FAST INTEGRAL EQUATION METHODS FOR THE MODIFIED HELMHOLTZ EQUATION

by

Bryan Quaife

B.Sc., University of Calgary, 2004

M.Sc., University of Calgary, 2006

A Thesis submitted in partial fulfillment
of the requirements for the degree of
Doctor of Philosophy
IN THE
DEPARTMENT OF MATHEMATICS
FACULTY OF SCIENCE

SIMON FRASER UNIVERSITY
Summer 2011

APPROVAL

Name: Bryan Quaife

Degree: Doctor of Philosophy

Title of Thesis: Fast Integral Equation Methods for the Modified Helmholtz Equation

Examining Committee: Dr. Ralf Wittenberg
Chair

Dr. Mary-Catherine Kropinski
Senior Supervisor

Dr. Nilima Nigam
Supervisor

Dr. Manfred Trummer
Supervisor

Dr. John Stockie
Internal Examiner

Dr. Leslie Greengard
External Examiner

Date Approved: _____

Abstract

Many problems in physics and engineering require the solution of the forced heat equation, $u_t - \Delta u = F(\mathbf{x}, u, t)$, with Dirichlet boundary conditions. In this thesis, we solve such PDEs in two-dimensional, multiply-connected domains, with a twice-continuously differentiable boundary. We discretize the partial differential equation (PDE) in time, known as Rothe's method, leading to the modified Helmholtz equation, $u(\mathbf{x}) - \alpha^2 \Delta u(\mathbf{x}) = g(\mathbf{x}, t)$. At each time step, solutions are written as the sum of a volume potential and a solution of $u(\mathbf{x}) - \alpha^2 \Delta u(\mathbf{x}) = 0$ with appropriate boundary conditions.

The solution of the homogeneous PDE is written as a double layer potential with unknown density function. The density function satisfies a Fredholm integral equation of the second kind. Some advantages of integral equation methods are: the unknown function is defined only on the boundary of the domain, complex physical boundaries are easy to incorporate, the ill-conditioning associated with discretizing the governing equations is avoided, high-order accuracy is easy to attain, and far-field boundary conditions are handled naturally. The integral equation is discretized at N points with a high-order, hybrid Gauss-trapezoidal rule resulting in a dense $N \times N$ linear system. The linear system is solved using the generalized minimal residual method (GMRES). If the required matrix-vector multiplication is done directly, $\mathcal{O}(N^2)$ operations are required. This is reduced to $\mathcal{O}(N)$ or $\mathcal{O}(N \log N)$ using the fast multipole method (FMM). To demonstrate the versatility of integral equation methods, the homogeneous problem is solved in bounded and unbounded, as well as simply- and multiply-connected domains.

The volume integral is computed using a previously developed fast multipole-accelerated fourth-order method. This work is extended to general bounded domains and is coupled with the double layer potential.

Applying Rothe's method coupled with integral equation methods is tested on a collection of forced heat equation problems. This includes the homogeneous heat equation, a forced linear heat equation, and the Allen-Cahn equation.

Keywords:

Forced heat equation; Rothe's method; layer potentials; high-order quadrature; fast multipole method; volume integrals

Acknowledgments

I thank my supervisor, Mary-Catherine Kropinski, for offering me support, encouragment, and criticism, and for introducing me to integral equations and the fast multipole method. Many others affiliated with the Math Department and PIMS at SFU have provided a positive experience throughout my Ph.D.

I thank my parents and extended family for their continued support and encouragment. Finally, I owe a special thank you to my wife, Lindsey, and son, Jeremy, for their love and support.

Contents

List of Tables

List of Figures

Chapter 1

Introduction

Many problems in science and engineering require the solution of partial differential equations (PDEs). Integral equation methods offer an attractive alternative to conventional finite difference, finite element, and spectral methods for finding numerical solutions. They offer several notable advantages: complex boundaries are handled naturally, high-order accuracy is easier to attain, the correct boundary conditions at infinity are guaranteed, and ill-conditioning associated with directly discretizing the PDE is avoided. Nevertheless, since discretizations of integral equations result in dense linear systems, these methods have been less popular than others. However, with the advancement of fast algorithms, integral equation methods have become popular for solving large-scale problems.

1.1 The Heat Equation

Many PDEs of interest involve the heat operator

$$\frac{\partial}{\partial t} - \beta^2 \Delta.$$

We consider the general forced heat equation

$$u_t(\mathbf{x}, t) - \beta^2 \Delta u(\mathbf{x}, t) = F(\mathbf{x}, u, t), \quad \mathbf{x} \in \Omega, t > 0, \tag{1.1a}$$

$$u(\mathbf{x}, t) = f(\mathbf{x}, t), \quad \mathbf{x} \in \Gamma, t > 0, \tag{1.1b}$$

$$u(\mathbf{x}, 0) = u_0(\mathbf{x}), \quad \mathbf{x} \in \Omega. \tag{1.1c}$$

The domain $\Omega \subset \mathbb{R}^2$ may be bounded or unbounded, simply- or multiply-connected, and has a twice-continuously differentiable boundary Γ. Applications arise in fluid dynamics,

pattern formation, and variational problems. Several choices for β^2 and F are:

- $F = 0$ and $\beta^2 = \kappa$ is the homogeneous heat equation, where κ is the thermal diffusivity.
- $F = F(\mathbf{x}, t)$ and $\beta^2 = \kappa$ is the heat equation with an external force.
- $F = u(1 - u^2)$ and $\beta^2 = \epsilon \ll 1$ is the Allen-Cahn equation.
- The system

  $$\mathbf{f}(\mathbf{u}) = \begin{pmatrix} a - (b+1)u + u^2 v \\ bu - u^2 v \end{pmatrix},$$

  where

  $$\mathbf{u} = \begin{pmatrix} u \\ v \end{pmatrix} \quad \text{and} \quad \beta^2 = \begin{pmatrix} D_u & 0 \\ 0 & D_v \end{pmatrix}$$

  is the Brusselator. By manipulating the parameters a, b, D_u, and D_v, the Brusselator can go through both Turing and Hopf bifurcations.
- The system

  $$\mathbf{f}(\mathbf{u}) = \begin{pmatrix} F(u, v) \\ G(u, v) \end{pmatrix},$$

  where $\mathbf{u}$ and β^2 are defined the same as the Brusselator is a general two-component reaction-diffusion system. Possible applications include population dynamics and pattern formation.
- $F(u) = \mathbf{v} \cdot \nabla u$, where $\mathbf{v}$ is a velocity field, and β^2 is a physical constant is the advection-diffusion problem

  $$\frac{Du}{Dt} = \beta^2 \Delta u.$$

  This PDE is important in many fluid dynamic applications.

1.2 Time Discretization

The goal of this thesis is to develop integral equation methods for numerically solving (1.1). One common approach is the method of lines which discretizes the spatial derivatives

of (1.1). The result is a system of coupled ordinary differential equations which are solved using a time-stepping scheme. Instead, we first discretize the time derivative of (1.1). This approach is known as Rothe's method and the result is an elliptic PDE that must be solved at each time step.

The time derivative can be discretized with linear multistep methods, Runge-Kutta methods, spectral deferred correction methods [19, 33, 34], or Implicit-Explict (IMEX) methods [4]. Often, large time steps can be taken if the diffusion term in (1.1a) is treated implicitly. Regardless of the time-stepping method, when the diffusion is treated implicitly, the resulting PDE is the modified Helmholtz equation

$$(1 - \alpha^2 \Delta) u^{N+1} = b, \tag{1.2}$$

where $\alpha^2 = \mathcal{O}(dt)$, $b = b(\mathbf{x}, t^N, \ldots, t^{N-p+1}, u^N, \ldots, u^{N-p+1})$, $t^N = Ndt$, and $u^N(\mathbf{x}) = u(\mathbf{x}, t^N)$. The number of previous time steps required, denoted here by p, depends on the time-stepping method and dt is the time step size.

In general, an integral equation formulation for the modified Helmholtz equation will require a layer potential and a volume integral. In this thesis, we couple two fast computational tools for the operator $(1 - \alpha^2 \Delta)$. In [17], Cheng et. al. present a fast direct solver for (1.2) in the two-dimensional unit square. The solution is expressed as a volume integral and is accelerated using the fast multipole method (FMM). In [37], Kropinski and Quaife present fast, well-conditioned integral equation methods for solving the homogeneous modified Helmholtz equation in bounded and unbounded multiply-connected domains. By coupling these methods, we solve (1.2) with Dirichlet boundary conditions in bounded multiply-connected domains.

1.3 Literature Review

The development of integral equations has focused largely on elliptic PDEs. Arguably, the most studied problems are Laplace's equation $\Delta u = 0$ [24], Poisson's equation $\Delta u = f$ [20], and the Helmholtz equation $\Delta u + k^2 u = 0$ [44]. There is literature on integral equation methods for the heat equation [9, 28, 29], but these equations require a full space-time history of the solution. Moreover, extendign these methods to more general PDEs is difficult or impossible.

There is previous work that uses integral equations to solve PDEs that arise from applying Rothe's method to time-dependent problems. For instance, the unsteady Stokes equations [11, 13], the unsteady incompressible Navier-Stokes equations [10, 38], and the homogeneous heat equation [14] have all been studied. More recently, Rothe's method has been applied to the forced heat equation (1.1) in [36].

Chapko and Kress [14] present an integral equation formulation for the heat equation ($F = 0$) that is free of volume integrals. Chapko applies a similar approach in [13] to the unsteady Stokes equations. However, these methods rely on homogeneous equations with homogeneous initial conditions. We are interested in a much broader class of problems.

Methods in this thesis closely resemble methods presented by Biros et. al. [11] for the Stokes equation which were extended to the Navier-Stokes equations in [10]. However, their work computes the volume integral using locally corrected finite difference stencils designed by Mayo [41]. These stencils account for jumps in the solution values across the interface of physical boundaries. The methods in [10, 11, 41] are two-dimensional and second-order, but this approach has been extended to fourth-order and three dimensions [43, 42]. While this method is much simpler than a volume integral, and is easily extended to three dimensions, it tends to impose severe time step restrictions. In the case of the Navier-Stokes equations, there is some indication that the differencing of the convection term leads to severe time step constraints as the Reynolds number increases [10]. In [38], the authors apply Rothe's method to the Navier-Stokes equations in the unit circle. They use a purely integral formulation, and the time step constraint is less problematic.

Fast algorithms have been developed for integral equations for a variety of elliptic boundary value problems. The FMM is one such method that was first developed by Greengard and Rokhlin [30]. An early example of its applications to integral equation is the work of Greenbaum et. al. [24] for Laplace's equation. Similar tools have been developed for Poisson's equation [20], Stokes equations [11, 26], and the modified Helmholtz equation [17, 37].

The development of corresponding fast algorithms for time-dependent problems is considerably more complex. There is literature for integral equations methods for the homogeneous heat equation. These rely on the heat kernel and thus require an integration in time and space [28, 29]. Methods that rely on a fast Gauss transform are discussed in [9, 47].

This thesis extends the methods outlined in [36] where the authors use Rothe's method to solve (1.1) with an added restriction: they require the forcing term b and the Dirichlet boundary condition be constant at each time step. Extending this work to more general

forcing terms and boundary conditions is discussed in Chapter 4.

1.4 Outline of Thesis

In Chapter 2, we demonstrate, by example, that the modified Helmholtz equation results from temporal discretizations of (1.1). We then focus on the homogeneous problem

$$(1 - \alpha^2\Delta)u = 0, \quad \mathbf{x} \in \Omega,$$

with either Dirichlet or Neumann boundary conditions, and either bounded or unbounded multiply-connected domains. This boundary value problem is recast as a boundary integral equation using standard potential theory. We establish uniqueness and existence of solutions of the boundary value problems and integral equations.

In Chapter 3, we present numerical methods for solving the integral equations from Chapter 2. The trapezoidal rule and high-order quadrature rules are both used to discretize the integral equations. The errors of these methods and properties of the resulting linear system are discussed. A near-singular integration is used to bound the error of u uniformly in Ω. Several examples that demonstrate the methods' robustness and high-order accuracy are presented.

In Chapter 4, we outline methods from [17] used to solve (1.2) in the absence of boundary conditions. We couple this method with methods developed in Chapters 2 and 3 to impose the desired boundary conditions. This requires extending functions from a bounded set Ω to a box containing Ω in a smooth fashion. Several examples demonstrate the expected accuracy.

In Chapter 5, the fast multipole method is presented. We alter the fast multipole method from [17] to develop a fast solver used to iteratively solve linear systems from Chapter 3. Comparisons of timings demonstrate the speedup.

Finally, Chapter 6 presents future directions and conclusions.

Chapter 2

The Modified Helmholtz Equation

In this chapter, we begin by showing in Section 2.1 how the modified Helmholtz equation (1.2) arises from two different IMEX temporal discretizations of (1.1). Such methods treat diffusion implicitly and nonlinearities explicitly to help avoid severe time step restrictions. At this point, it becomes apparent that regardless of which IMEX time-stepping method from [4] is used, the resulting PDE is always the modified Helmholtz equation. Then, in Section 2.2, we establish that solutions of the modified Helmholtz equation are unique in bounded and unbounded domains. For unbounded domains, we require an appropriate condition at infinity which is found using the Kelvin transform. We then find the fundamental solution.

We use the fundamental solution to introduce layer potentials in Section 2.3. In particular, we define the single layer potential and the double layer potential. Potential theory is used to recast the modified Helmholtz equation as a boundary integral equation. We show that Fredholm integral equations of the second kind result from the single layer potential if the boundary condition is Neumann, and, from the double layer potential if the boundary condition is Dirichlet. In Section 2.4, we prove existence and uniqueness of solutions of these second kind integral equations. These proofs rely on the compactness of the integral operators and the Fredholm Alternative. The existence of solutions of the integral equation establishes existence of solutions of the modified Helmholtz equation.

In Section 2.5, we discuss key differences between results in this chapter and parallel results for standard potential theory applied to Laplace's equation. We also compare and contrast the integral equations from Section 2.3 and discuss how similarities can be exploited in numerical solvers.

2.1 Implicit-Explicit Methods

Our general strategy for solving (1.1) is to discretize in time, known as Rothe's method, and then solve the resulting PDE at each time step. One class of temporal discretizations that can be applied to (1.1) is the IMEX method [4]. A general theme of these methods is implicit treatment of stiff terms, in this case the diffusion, and explicit treatment of nonlinear terms. IMEX methods ranging from first- to fourth-order are outlined in [4].

Here, we give two IMEX methods. We let dt be the size of the time step, $t^N = Ndt$, and $u^N(\mathbf{x}) = u(\mathbf{x}, t^N)$. The simplest IMEX scheme is the first-order IMEX Euler method

$$\frac{1}{dt}\left(u^{N+1} - u^N\right) = \beta^2 \Delta u^{N+1} + F(u^N). \tag{2.1}$$

A second-order method is the extrapolated Gear method

$$\frac{1}{2dt}\left(3u^{N+1} - 4u^N + u^{N-1}\right) = 2F(u^N) - F(u^{N-1}) + \beta^2\,\Delta u^{N+1}. \tag{2.2}$$

Upon rearranging (2.1),

$$(1 - \beta^2 dt\Delta)u^{N+1} = u^N + dtF(u^N), \tag{2.3}$$

and rearranging (2.2),

$$\left(1 - \beta^2 \frac{2dt}{3}\Delta\right) u^{N+1} = \frac{1}{3}(4u^N - u^{N-1}) + \frac{2dt}{3}(2F(u^N) - F(u^{N-1})). \tag{2.4}$$

In the case of IMEX Euler, if we define

$$\alpha^2 = \beta^2 dt, \quad b = u^N + dtF(u^N),$$

and in the case of extrapolated Gear, if we define

$$\alpha^2 = \beta^2 \frac{2dt}{3}, \quad b = \frac{1}{3}(4u^N - u^{N-1}) + \frac{2dt}{3}(2F(u^N) - F(u^{N-1})),$$

both (2.3) and (2.4) result in the PDE

$$(1 - \alpha^2\Delta)u^{N+1} = b. \tag{2.5}$$

In fact, using any IMEX method outlined in [4] results in the PDE (2.5), where $\alpha^2 > 0$ and $b = b(\mathbf{x}, t^N, \ldots, t^{N-p+1}, u^N, \ldots, u^{N-p+1})$. The number of previous time steps, denoted here by p, depends on the time integration scheme. For IMEX Euler, $p = 1$, while for extrapolated Gear, $p = 2$.

2.2 The Modified Helmholtz Equation

Assume that Ω is an open, bounded, multiply-connected subset of $\mathbb{R}^2$. Furthermore, assume $\Gamma := \partial\Omega$ has at least two continuous derivatives and write ν for the unit outward normal vector. An illustration of a bounded and unbounded multiply-connected domain is in Figure 2.1.

To use more standard notation, equation (2.5) is written as

$$(1 - \alpha^2\Delta)u = g, \quad \mathbf{x} \in \Omega, \tag{2.6a}$$

$$u = f, \quad \mathbf{x} \in \Gamma, \tag{2.6b}$$

and is called the modified Helmholtz equation. Solving (2.6) is the main goal of this thesis. Many applications have a boundary condition for the normal derivative, so we also consider the Neumann problem

$$(1 - \alpha^2\Delta)u = g, \quad \mathbf{x} \in \Omega, \tag{2.7a}$$

$$\frac{\partial u}{\partial \nu} = f, \quad \mathbf{x} \in \Gamma. \tag{2.7b}$$

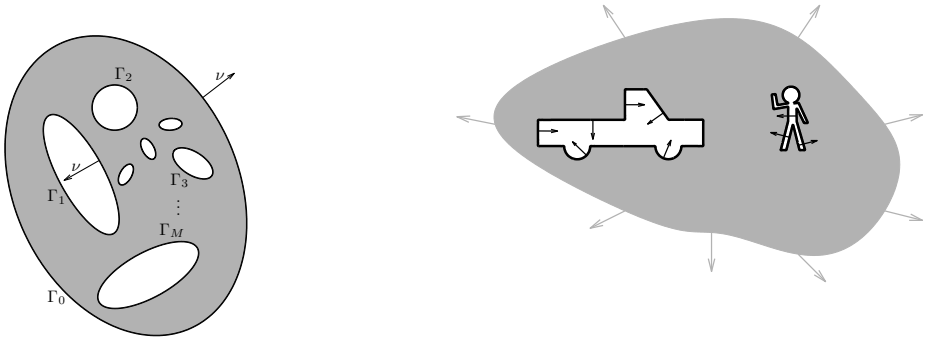

Figure 2.1: The left plot is a bounded multiply-connected domain Ω (shaded region). The outer boundary is denoted by Γ_0 and the interior component curves by $\Gamma_1, \ldots, \Gamma_M$. The unit normal ν points out of Ω on each component curve. The right plot is an unbounded 2-ply-connected domain Ω (everything outside the truck and the person). The unit normal points into each of the component curves.

2.2.1 Uniqueness of Solutions

We check that solutions of (2.6) are unique; existence will follow once we have recast (2.6) as a solvable integral equation. We start by assuming that Ω is bounded and assume that u_1 and u_2 both solve (2.6). Then, $w := u_1 - u_2$ satisfies

$$(1 - \alpha^2\Delta)w = 0, \quad \mathbf{x} \in \Omega, \tag{2.8a}$$

$$w = 0, \quad \mathbf{x} \in \Gamma. \tag{2.8b}$$

We multiply (2.8a) by w, integrate over Ω, and apply Green's first identity

$$\begin{aligned} 0 &= \int_\Omega w^2 d\mathbf{x} - \alpha^2 \int_\Omega w\Delta w d\mathbf{x} \\ &= \int_\Omega w^2 d\mathbf{x} - \alpha^2 \left(\int_\Gamma w \frac{\partial w}{\partial \nu} ds - \int_\Omega |\nabla w|^2 d\mathbf{x} \right) \\ &= \int_\Omega w^2 d\mathbf{x} + \alpha^2 \int_\Omega |\nabla w|^2 d\mathbf{x}, \end{aligned}$$

which implies that $w = 0$ and thus $u_1 = u_2$. The same argument can be used to establish uniqueness of solutions of (2.7), or a problem with a combination of Neumann and Dirichlet boundary conditions.

Let Ω be unbounded. Uniqueness of solutions requires a condition for the behavior of u at infinity. We use a standard technique to uncover this behavior. Without loss of generality, assume that $0 \notin \Omega$ and define the Kelvin transform

$$T : \mathbb{R}^2 \cup \{\infty\} \to \mathbb{R}^2 \cup \{\infty\},$$

$$T\mathbf{x} = \begin{cases} \frac{\mathbf{x}}{|\mathbf{x}|^2}, & \mathbf{x} \neq 0 \text{ or } \infty, \\ 0, & \mathbf{x} = \infty, \\ \infty, & \mathbf{x} = 0. \end{cases}$$

Since Ω is unbounded, $T(\Omega) = \{T\mathbf{x} \mid \mathbf{x} \in \Omega\}$ is bounded. A standard application of the chain rule shows that if $u^\star(\mathbf{x}) = u(T\mathbf{x})$, then

$$\Delta u^\star(\mathbf{x}) = \frac{1}{|\mathbf{x}|^4} \Delta u(T\mathbf{x}).$$

Applying the Kelvin transform to (2.6) gives

$$(1 - \alpha^2|\mathbf{x}|^4\Delta)u^\star = g^\star, \quad \mathbf{x} \in T(\Omega),$$

$$u^\star = f^\star, \quad \mathbf{x} \in T(\Gamma),$$

where $f^\star(\mathbf{x}) = f(T\mathbf{x})$ and $g^\star(\mathbf{x}) = g(T\mathbf{x})$. In order to show that solutions of this PDE are unique, we again assume u_1 and u_2 are solutions and let $w = u_1 - u_2$. Then, w satisfies

$$\begin{aligned}(1-\alpha^2|\mathbf{x}|^4\Delta)w = 0, \quad & \mathbf{x} \in T(\Omega),\\ w = 0, \quad & \mathbf{x} \in T(\Gamma).\end{aligned}$$

By substituting $\mathbf{x} = 0 \in T(\Omega)$, we have $w(0) = 0$. Now, we multiply by $w/|\mathbf{x}|^4$, integrate over $T(\Omega)_\epsilon := \{\mathbf{x} \in T(\Omega) \mid |\mathbf{x}| > \epsilon\}$, and apply Green's first identity

$$\begin{aligned}0 &= \int_{T(\Omega)_\epsilon} \frac{1}{|\mathbf{x}|^4} w^2 d\mathbf{x} - \alpha^2 \int_{T(\Omega)_\epsilon} w\Delta w d\mathbf{x}\\ &= \int_{T(\Omega)_\epsilon} \frac{1}{|\mathbf{x}|^4} w^2 d\mathbf{x} - \alpha^2 \left(\int_{|\mathbf{x}|=\epsilon} w\frac{\partial w}{\partial \nu} ds + \int_{T(\Gamma)} w\frac{\partial w}{\partial \nu} ds - \int_{T(\Omega)_\epsilon} |\nabla w|^2 d\mathbf{x} \right) \qquad (2.9)\\ &= \int_{T(\Omega)_\epsilon} \frac{1}{|\mathbf{x}|^4} w^2 d\mathbf{x} + \alpha^2 \int_{T(\Omega)_\epsilon} |\nabla w|^2 d\mathbf{x}.\end{aligned}$$

The first boundary integral in (2.9) vanishes as $\epsilon \to 0$ since $w(0) = 0$ and the second vanishes because of the boundary condition. The result is that $w = 0$ in Ω_ϵ for $\epsilon > 0$ guaranteeing that $w = 0$ in $T(\Omega)$. We have just proved the following theorem.

Theorem 2.1 *Let Ω be an unbounded simply- or multiply-connected domain. If a solution of*

$$\begin{aligned}(1-\alpha^2\Delta)u = g, \qquad & \mathbf{x} \in \Omega,\\ u = f, \qquad & \mathbf{x} \in \Gamma,\\ \lim_{R\to\infty} \sup_{|\mathbf{x}|>R} u(\mathbf{x}) = 0,\end{aligned}$$

exists, it is unique. If Ω is bounded, the condition at infinity is omitted. Moreover, if the boundary condition is Neumann, the result still holds.

A key difference between Laplace's equation and the modified Helmholtz equation concerns the uniqueness of solutions for the Neumann problem, and the compatibility constraint of the boundary data. Solutions of Laplace's equation with a Neumann boundary condition are not unique. If u is a solution, so is $u + c$ for any $c \in \mathbb{R}$. Also, if f is the Neumann boundary condition of Laplace's equation, it must satisfy the compatibility constraint $\int_\Gamma f = 0$. Solutions of the modified Helmholtz equation are unique and there are no restrictions on the boundary condition.

2.2.2 The Fundamental Solution

To develop integral equation methods for the modified Helmholtz equation, we require the fundamental solution, sometimes called the free-space Green's function, of the operator $(1-\alpha^2\Delta)$. This is the function G satisfying, in the weak sense,

$$(1-\alpha^2\Delta)G = \delta, \quad \mathbf{x} \in \mathbb{R}^2, \tag{2.10}$$

$$\lim_{R\to\infty} \sup_{|\mathbf{x}|>R} G(\mathbf{x}) = 0, \tag{2.11}$$

where δ is the delta distribution. In this thesis, the fundamental solution has two purposes. First, it will be used in Section 2.3 to formulate solution ansätze for the homogeneous modified Helmholtz equation. Then, in Chapter 4, it will be used to form a solution of the modified Helmholtz equation in the absence of boundary conditions. The condition at infinity (2.11) guarantees that solutions of the modified Helmholtz equation in unbounded domains will decay to 0 at infinity.

We imitate [21] where the fundamental solution of Laplace's equation is constructed. Since $(1-\alpha^2\Delta)$ is rotationally invariant, we assume that $G = G(r)$, where $r = \sqrt{x^2+y^2}$. In polar coordinates, (2.10) reduces to

$$G - \alpha^2\left(G_{rr} - \frac{1}{r}G_r\right) = \delta.$$

For $r \neq 0$,

$$G(r) = c_1 K_0\left(\frac{r}{\alpha}\right) + c_2 I_0\left(\frac{r}{\alpha}\right),$$

where K_0 and I_0 are the modified Bessel functions of order 0 of the first kind and second kind, respectively. Since I_0 is unbounded at infinity, we let $c_2 = 0$ so that (2.11) is satisfied. In the next theorem, we find the correct value for c_1.

Before we find this value, we define $B(0,r) = \{\mathbf{x} \in \mathbb{R}^2 \mid |\mathbf{x}| < r\}$, the open ball centered at 0 of radius r. We also write $a(\epsilon) \lesssim b(\epsilon)$ whenever $a(\epsilon) < cb(\epsilon)$ with c independent of ϵ. Finally, we require the following formulas found in [1]. For $z > 0$,

$$\begin{aligned}
zK_0\left(\frac{z}{\alpha}\right) &= \mathcal{O}(z\log z), && z \ll 1,\\
zK_1\left(\frac{z}{\alpha}\right) &= \alpha + \mathcal{O}(z^2\log z), && z \ll 1,\\
\frac{d}{dz}K_0\left(\frac{z}{\alpha}\right) &= -\frac{1}{\alpha}K_1\left(\frac{z}{\alpha}\right),\\
\int zK_0\left(\frac{z}{\alpha}\right)dz &= -\alpha z\, K_1\left(\frac{z}{\alpha}\right).
\end{aligned}$$

Theorem 2.2 *The fundamental solution of* $(1-\alpha^2\Delta)$ *is*

$$G(\mathbf{x}) = \frac{1}{2\pi\alpha^2} K_0\left(\frac{|\mathbf{x}|}{\alpha}\right).$$

Proof We closely follow the proof in [21]. Let $f \in C^2(\mathbb{R}^2)$ have compact support and define

$$v(\mathbf{x}) := \int_{\mathbb{R}^2} G(\mathbf{x}-\mathbf{y}) f(\mathbf{y}) d\mathbf{y} = \int_{\mathbb{R}^2} G(\mathbf{y}) f(\mathbf{x}-\mathbf{y}) d\mathbf{y}.$$

Our goal is to show that $(1-\alpha^2\Delta)v(\mathbf{x}) = f(\mathbf{x})$. We begin by computing the Laplacian of v. Letting $\epsilon > 0$,

$$\begin{aligned}
\Delta v(\mathbf{x}) &= \int_{\mathbb{R}^2} G(\mathbf{y}) \Delta_{\mathbf{x}} f(\mathbf{x}-\mathbf{y}) d\mathbf{y} \\
&= \int_{\mathbb{R}^2 \setminus B(0,\epsilon)} G(\mathbf{y}) \Delta_{\mathbf{x}} f(\mathbf{x}-\mathbf{y}) d\mathbf{y} + \int_{B(0,\epsilon)} G(\mathbf{y}) \Delta_{\mathbf{x}} f(\mathbf{x}-\mathbf{y}) d\mathbf{y} \\
&= A_\epsilon + B_\epsilon. \qquad (2.12)
\end{aligned}$$

Since $f \in C^2$, we can bound $|B_\epsilon|$ by

$$\begin{aligned}
|B_\epsilon| &\lesssim \int_{B(0,\epsilon)} K_0\left(\frac{|\mathbf{y}|}{\alpha}\right) d\mathbf{y} \\
&= \int_0^\epsilon K_0\left(\frac{r}{\alpha}\right) r dr \\
&= \alpha r K_1\left(\frac{r}{\alpha}\right)\Big|_\epsilon^0 \\
&= \alpha^2 - \alpha\epsilon K_1\left(\frac{\epsilon}{\alpha}\right) \\
&= \alpha^2 - \alpha(\alpha + \mathcal{O}(\epsilon^2 \log \epsilon)) \\
&= \mathcal{O}(\epsilon^2 \log \epsilon). \qquad (2.13)
\end{aligned}$$

We next apply Green's first identity to A_ϵ

$$\begin{aligned}
A_\epsilon &= \int_{\mathbb{R}^2 \setminus B(0,\epsilon)} G(\mathbf{y}) \Delta_{\mathbf{x}} f(\mathbf{x}-\mathbf{y}) d\mathbf{y} \\
&= \int_{\mathbb{R}^2 \setminus B(0,\epsilon)} G(\mathbf{y}) \Delta_{\mathbf{y}} f(\mathbf{x}-\mathbf{y}) d\mathbf{y} \\
&= -\int_{\mathbb{R}^2 \setminus B(0,\epsilon)} \nabla_{\mathbf{y}} G(\mathbf{y}) \cdot \nabla_{\mathbf{y}} f(\mathbf{x}-\mathbf{y}) d\mathbf{y} + \int_{\partial B(0,\epsilon)} G(\mathbf{y}) \frac{\partial f(\mathbf{x}-\mathbf{y})}{\partial \nu_{\mathbf{y}}} ds_{\mathbf{y}} \\
&= C_\epsilon + D_\epsilon. \qquad (2.14)
\end{aligned}$$

We bound $|D_\epsilon|$ by

$$\begin{aligned} |D_\epsilon| &\lesssim \int_{\partial B(0,\epsilon)} K_0\left(\frac{r}{\alpha}\right) ds_{\mathbf{y}} \\ &= K_0\left(\frac{\epsilon}{\alpha}\right) 2\pi\epsilon \\ &= \mathcal{O}(\epsilon \log \epsilon). \end{aligned} \tag{2.15}$$

Next,

$$\begin{aligned} v(x) &= \int_{\mathbb{R}^2 \setminus B(0,\epsilon)} G(\mathbf{y}) f(\mathbf{x}-\mathbf{y}) d\mathbf{y} + \int_{B(0,\epsilon)} G(\mathbf{y}) f(\mathbf{x}-\mathbf{y}) d\mathbf{y} \\ &= E_\epsilon + F_\epsilon. \end{aligned} \tag{2.16}$$

We bound $|F_\epsilon|$ exactly the same as $|B_\epsilon|$

$$|F_\epsilon| \lesssim \mathcal{O}(\epsilon^2 \log \epsilon). \tag{2.17}$$

Only C_ϵ and E_ϵ remain when $\epsilon \to 0$, so we compute

$$\begin{aligned} E_\epsilon - \alpha^2 C_\epsilon &= \int_{\mathbb{R}^2 \setminus B(0,\epsilon)} G(\mathbf{y}) f(\mathbf{x}-\mathbf{y}) d\mathbf{y} + \alpha^2 \int_{\mathbb{R}^2 \setminus B(0,\epsilon)} \nabla_{\mathbf{y}} G(\mathbf{y}) \cdot \nabla_{\mathbf{y}} f(\mathbf{x}-\mathbf{y}) d\mathbf{y} \\ &= \int_{\mathbb{R}^2 \setminus B(0,\epsilon)} G(\mathbf{y}) f(\mathbf{x}-\mathbf{y}) d\mathbf{y} \\ &+ \alpha^2 \int_{\partial B(0,\epsilon)} \frac{\partial G}{\partial \nu_{\mathbf{y}}} f(\mathbf{x}-\mathbf{y}) ds_{\mathbf{y}} - \alpha^2 \int_{\mathbb{R}^2 \setminus B(0,\epsilon)} \Delta_{\mathbf{y}} G(\mathbf{y}) f(\mathbf{x}-\mathbf{y}) d\mathbf{y} \\ &= \int_{\mathbb{R}^2 \setminus B(0,\epsilon)} (1-\alpha^2\Delta) G(\mathbf{y}) f(\mathbf{x}-\mathbf{y}) d\mathbf{y} + \alpha^2 \int_{\partial B(0,\epsilon)} \frac{\partial G}{\partial \nu_{\mathbf{y}}} f(\mathbf{x}-\mathbf{y}) ds_{\mathbf{y}} \\ &= \alpha^2 \int_{\partial B(0,\epsilon)} \frac{\partial G}{\partial \nu_{\mathbf{y}}} f(\mathbf{x}-\mathbf{y}) ds_{\mathbf{y}} \\ &= \frac{\alpha^2}{2\pi\alpha^2} \int_{\partial B(0,\epsilon)} \frac{\partial}{\partial \nu_{\mathbf{y}}} K_0\left(\frac{|\mathbf{y}|}{\alpha}\right) f(\mathbf{x}-\mathbf{y}) ds_{\mathbf{y}} \\ &= -\frac{1}{2\pi} \int_{\partial B(0,\epsilon)} \frac{1}{\alpha|\mathbf{y}|} K_1\left(\frac{|\mathbf{y}|}{\alpha}\right) \mathbf{y} \cdot \nu_{\mathbf{y}} f(\mathbf{x}-\mathbf{y}) ds_{\mathbf{y}}. \end{aligned}$$

The region of integration is exterior to $B(0,\epsilon)$, so $\nu_{\mathbf{y}} = -\mathbf{y}/|\mathbf{y}|$, and

$$\begin{aligned} E_\epsilon - \alpha^2 C_\epsilon &= \frac{1}{2\pi} \int_{\partial B(0,\epsilon)} \frac{1}{\alpha|\mathbf{y}|} K_1\left(\frac{|\mathbf{y}|}{\alpha}\right) \mathbf{y} \cdot \frac{\mathbf{y}}{|\mathbf{y}|} f(\mathbf{x}-\mathbf{y}) ds_{\mathbf{y}} \\ &= \frac{1}{2\pi\epsilon} K_1\left(\frac{\epsilon}{\alpha}\right) \frac{\epsilon}{\alpha} \int_{\partial B(0,\epsilon)} f(\mathbf{x}-\mathbf{y}) ds_{\mathbf{y}}. \end{aligned} \tag{2.18}$$

Since $zK_1(z) \to 1$ as $z \to 0$, combining (2.12)–(2.18),

$$\begin{aligned}(1-\alpha^2\Delta)v(\mathbf{x}) &= \lim_{\epsilon\to 0}\frac{1}{2\pi\epsilon}\int_{\partial B(0,\epsilon)} f(\mathbf{x}-\mathbf{y})ds_{\mathbf{y}} \\ &= \frac{1}{2\pi\epsilon}2\pi\epsilon f(\mathbf{x}) \\ &= f(\mathbf{x}).\end{aligned}$$

In other words,

$$(1-\alpha^2\Delta)G(\mathbf{x}) = \delta(\mathbf{x})$$

in the weak sense. □

In order to derive integral equations for the modified Helmholtz equation, we must understand the behavior of G at 0. We use well-known results for Laplace's fundamental solution in combination with the asymptotic expansion [1]

$$\begin{aligned}K_0(z) = -\log\left(\frac{z}{2}\right) - \log\left(\frac{z}{2}\right)\sum_{n=1}^{\infty}\frac{1}{(n!)^2}\left(\frac{z^2}{4}\right)^n + \gamma\left(1+\sum_{n=1}^{\infty}\frac{1}{(n!)^2}\left(\frac{z^2}{4}\right)^n\right) \\ + \sum_{n=1}^{\infty}\left(1+\frac{1}{2}+\cdots+\frac{1}{n}\right)\frac{1}{(n!)^2}\left(\frac{z^2}{4}\right)^n,\end{aligned}$$

or in a more compact form,

$$K_0(z) = -\log\left(\frac{z}{2}\right) + p(z)\log\left(\frac{z}{2}\right) + q(z). \tag{2.19}$$

The lowest order term of $p(z)$ is z^2 and γ is Euler's constant. The principal result is that $K_0(z)$ has a logarithmic-type singularity at $z = 0$. When forming integral equations, this will allow us to use results of integral equations for Laplace's equation.

2.3 Layer Potentials

Our strategy for solving (2.6) is to write its solution as the sum of a forced problem and a homogeneous problem. First, we find a solution for the forced problem

$$(1-\alpha^2\Delta)u^P = g, \quad \mathbf{x}\in\Omega. \tag{2.20}$$

Boundary conditions are not specified, therefore, solutions are not unique. However, we can take any solution of (2.20) that we wish; we discuss one possible solution of (2.20) in Chapter 4. We impose the boundary conditions by solving the homogeneous problem

$$\begin{aligned}(1-\alpha^2\Delta)u^H &= 0, && \mathbf{x}\in\Omega,\\ u^H &= f-u^P, && \mathbf{x}\in\Gamma.\end{aligned}$$

Then, $u = u^P + u^H$ solves (2.6). Upon redefining f, the homogeneous problem becomes

$$(1-\alpha^2\Delta)u^H = 0, \quad \mathbf{x}\in\Omega, \tag{2.21a}$$

$$u^H = f, \quad \mathbf{x}\in\Gamma. \tag{2.21b}$$

If we have a Neumann boundary condition, the homogeneous problem is

$$(1-\alpha^2\Delta)u^H = 0, \quad \mathbf{x}\in\Omega, \tag{2.22a}$$

$$\frac{\partial u^H}{\partial \nu} = f, \quad \mathbf{x}\in\Gamma. \tag{2.22b}$$

The remainder of this chapter is dedicated to solving (2.21) and (2.22). A layer potential is an ansatz for the solution of the homogeneous modified Helmholtz equation. It recasts the PDE as a boundary integral equation. The two most common layer potentials, both of which are discussed next, are the single layer potential and double layer potential.

2.3.1 Single Layer Potential

The single layer potential is the integral operator $\mathcal{S}[\sigma] : \Omega \to \mathbb{R}$, where

$$\mathcal{S}[\sigma](\mathbf{x}) = \frac{1}{2\pi\alpha^2}\int_\Gamma K_0\left(\frac{|\mathbf{y}-\mathbf{x}|}{\alpha}\right)\sigma(\mathbf{y})\,ds_{\mathbf{y}}. \tag{2.23}$$

The single layer potential takes a function $\sigma : \Gamma \to \mathbb{R}$, which we call a density function, and returns a real-valued function defined on Ω. We assume that $\sigma \in C(\Gamma)$, the space of continuous functions, so that (2.23) is well-defined. Defining the kernel of $S[\sigma]$ to be

$$K(\mathbf{y},\mathbf{x}) = \frac{1}{2\pi\alpha^2}K_0\left(\frac{|\mathbf{y}-\mathbf{x}|}{\alpha}\right),$$

the single layer potential can be written as

$$S[\sigma](\mathbf{x}) = \int_\Gamma K(\mathbf{y},\mathbf{x})\sigma(\mathbf{y})ds_{\mathbf{y}}.$$

We begin by showing that, regardless of σ, the single layer potential satisfies the modified Helmholtz equation. The function σ is later used to satisfy the boundary condition.

Theorem 2.3 *If $\sigma \in C(\Gamma)$, then*

$$u^H(\mathbf{x}) = \frac{1}{2\pi\alpha^2} \int_\Gamma K_0 \left(\frac{|\mathbf{y}-\mathbf{x}|}{\alpha} \right) \sigma(\mathbf{y}) ds_\mathbf{y} \tag{2.24}$$

solves (2.21a).

Proof For $\mathbf{x} \in \Omega$,

$$(1-\alpha^2\Delta)u^H(\mathbf{x}) = (1-\alpha^2\Delta)\frac{1}{2\pi\alpha^2} \int_\Gamma K_0 \left(\frac{|\mathbf{y}-\mathbf{x}|}{\alpha} \right) \sigma(\mathbf{y}) ds_\mathbf{y}.$$

When $\mathbf{x} \notin \Gamma$, the integrand is bounded, so, the integral and derivatives can be interchanged

$$\begin{aligned}(1-\alpha^2\Delta)u^H(\mathbf{x}) &= \frac{1}{2\pi\alpha^2} \int_\Gamma (1-\alpha^2\Delta) K_0 \left(\frac{|\mathbf{y}-\mathbf{x}|}{\alpha} \right) \sigma(\mathbf{y}) ds_\mathbf{y} \\ &= \int_\Gamma \delta(\mathbf{y}-\mathbf{x})\sigma(\mathbf{y}) ds_\mathbf{y} \\ &= 0.\end{aligned}$$

□

The single layer potential satisfies (2.21a), but we have not imposed the boundary condition (2.21b). The boundary condition is satisfied by taking the limit of (2.24) as $\mathbf{x} \to \mathbf{x}_0$ and equating it with $f(\mathbf{x}_0)$. That is, we find σ such that

$$\lim_{\substack{\mathbf{x}\to\mathbf{x}_0 \\ \mathbf{x}\in\Omega}} \frac{1}{2\pi\alpha^2} \int_\Gamma K_0 \left(\frac{|\mathbf{y}-\mathbf{x}|}{\alpha} \right) \sigma(\mathbf{y}) ds_\mathbf{y} = f(\mathbf{x}_0)$$

for all $\mathbf{x}_0 \in \Gamma$. To compute this limit, we use the jump condition for the logarithmic kernel [23, Prop 3.25]. For any $\mathbf{x}_0 \in \Gamma$,

$$\lim_{\substack{\mathbf{x}\to\mathbf{x}_0 \\ \mathbf{x}\in\Omega}} \frac{1}{2\pi} \int_\Gamma \log|\mathbf{y}-\mathbf{x}| \sigma(\mathbf{y}) ds_\mathbf{y} = \frac{1}{2\pi} \int_\Gamma \log|\mathbf{y}-\mathbf{x}_0| \sigma(\mathbf{y}) ds_\mathbf{y}. \tag{2.25}$$

Theorem 2.4 *Suppose that σ satisfies*

$$f(\mathbf{x}_0) = \frac{1}{2\pi\alpha^2} \int_\Gamma K_0 \left(\frac{|\mathbf{y}-\mathbf{x}_0|}{\alpha} \right) \sigma(\mathbf{y}) ds_\mathbf{y}.$$

Then, the single layer potential (2.24) *satisfies* (2.21a) *and* (2.21b).

Proof We have already shown that the single layer representation (2.24) satisfies (2.21a). We use (2.19) and (2.25) to show that it satisfies the boundary condition (2.21b)

$$\begin{aligned}
\lim_{\substack{\mathbf{x}\to\mathbf{x}_0\\ \mathbf{x}\in\Omega}} u^H(\mathbf{x}) &= \lim_{\substack{\mathbf{x}\to\mathbf{x}_0\\ \mathbf{x}\in\Omega}} \frac{1}{2\pi\alpha^2}\int_\Gamma K_0\left(\frac{|\mathbf{y}-\mathbf{x}|}{\alpha}\right)\sigma(\mathbf{y})ds_\mathbf{y} \\
&= -\lim_{\substack{\mathbf{x}\to\mathbf{x}_0\\ \mathbf{x}\in\Omega}} \frac{1}{2\pi\alpha^2}\int_\Gamma \log\left(\frac{|\mathbf{y}-\mathbf{x}|}{2\alpha}\right)\sigma(\mathbf{y})ds_\mathbf{y} \\
&\qquad -\lim_{\substack{\mathbf{x}\to\mathbf{x}_0\\ \mathbf{x}\in\Omega}} \frac{1}{2\pi\alpha^2}\int_\Gamma p\left(\frac{|\mathbf{y}-\mathbf{x}|}{\alpha}\right)\log\left(\frac{|\mathbf{y}-\mathbf{x}|}{2\alpha}\right)\sigma(\mathbf{y})ds_\mathbf{y} \\
&\qquad +\lim_{\substack{\mathbf{x}\to\mathbf{x}_0\\ \mathbf{x}\in\Omega}} \frac{1}{2\pi\alpha^2}\int_\Gamma q\left(\frac{|\mathbf{y}-\mathbf{x}|}{\alpha}\right)\sigma(\mathbf{y})ds_\mathbf{y} \\
&= -\frac{1}{2\pi\alpha^2}\int_\Gamma \log\left(\frac{|\mathbf{y}-\mathbf{x}_0|}{2\alpha}\right)\sigma(\mathbf{y})ds_\mathbf{y} \\
&\qquad -\frac{1}{2\pi\alpha^2}\int_\Gamma p\left(\frac{|\mathbf{y}-\mathbf{x}_0|}{\alpha}\right)\log\left(\frac{|\mathbf{y}-\mathbf{x}_0|}{2\alpha}\right)\sigma(\mathbf{y})ds_\mathbf{y} \\
&\qquad +\frac{1}{2\pi\alpha^2}\int_\Gamma q\left(\frac{|\mathbf{y}-\mathbf{x}_0|}{\alpha}\right)\sigma(\mathbf{y})ds_\mathbf{y} \\
&= \frac{1}{2\pi\alpha^2}\int_\Gamma K_0\left(\frac{|\mathbf{y}-\mathbf{x}_0|}{\alpha}\right)\sigma(\mathbf{y})ds_\mathbf{y}.
\end{aligned}$$

The first limit is evaluated using (2.25). Since $p(z)\log(z)$ and $q(z)$ are bounded at $z=0$, the second and third limits follow since the integrand is bounded. □

To solve the Neumann problem (2.22), we require the normal derivative of the single layer potential,

$$\lim_{\substack{\mathbf{x}\to\mathbf{x}_0\\ \mathbf{x}\in\Omega}} \frac{\partial}{\partial\nu_\mathbf{x}} S[\sigma](\mathbf{x}) = \lim_{\substack{\mathbf{x}\to\mathbf{x}_0\\ \mathbf{x}\in\Omega}} \frac{\partial}{\partial\nu_\mathbf{x}} \frac{1}{2\pi\alpha^2}\int_\Gamma K_0\left(\frac{|\mathbf{y}-\mathbf{x}|}{\alpha}\right)\sigma(\mathbf{y})ds_\mathbf{y}.$$

We have written $\frac{\partial}{\partial\nu_\mathbf{x}}$ for a point $\mathbf{x}\in\Omega$, but the normal vector is only defined on Γ. To alleviate this problem, we follow the procedure outlined in [23]. We define the tubular neighborhood, a set $T\subset\Omega$ of points near Γ. It is constructed so that for all $\mathbf{x}\in T$, there is exactly one point $\mathbf{x}_0\in\Gamma$ with the property that the normal vector $-\nu_{\mathbf{x}_0}$ passes through $\mathbf{x}$ (see Figure 2.2). With this unique point, we define $\nu_\mathbf{x}=\nu_{\mathbf{x}_0}$.

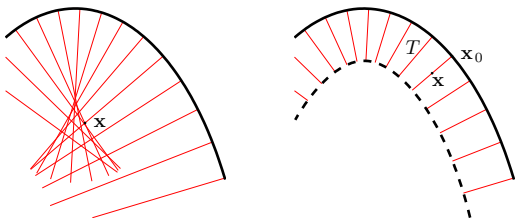

Figure 2.2: The bold line is a subset of Γ and the normal vectors are drawn at several points. The normal vectors intersect each other sufficiently far from Γ (left plot). However, if we define T as illustrated in the right plot, the normal vectors do not intersect. Thus, with each point $\mathbf{x} \in T$, we can associate a unique point $\mathbf{x}_0 \in \Gamma$ and then define $\nu_{\mathbf{x}} = \nu_{\mathbf{x}_0}$.

Now, we require the jump condition for the normal derivative of the single layer potential with logarithmic kernel [23, Lemma 3.30]

$$\lim_{\substack{\mathbf{x}\to\mathbf{x}_0 \\ \mathbf{x}\in\Omega}} \frac{\partial}{\partial \nu_{\mathbf{x}}} \frac{1}{2\pi} \int_\Gamma \log(|\mathbf{y}-\mathbf{x}|)\sigma(\mathbf{y}) ds_{\mathbf{y}} = -\frac{1}{2}\sigma(\mathbf{x}_0) + \frac{1}{2\pi}\int_\Gamma \frac{\partial}{\partial \nu_{\mathbf{x}_0}} \log(|\mathbf{y}-\mathbf{x}_0|)\sigma(\mathbf{y}) ds_{\mathbf{y}}. \tag{2.26}$$

Theorem 2.5 *Suppose that σ satisfies*

$$f(\mathbf{x}_0) = \frac{1}{2\alpha^2}\sigma(\mathbf{x}_0) + \frac{1}{2\pi}\int_\Gamma \frac{\partial}{\partial \nu_{\mathbf{x}_0}} K_0\left(\frac{|\mathbf{y}-\mathbf{x}_0|}{\alpha}\right)\sigma(\mathbf{y}) ds_{\mathbf{y}}. \tag{2.27}$$

Then, the single layer potential (2.24) *satisfies* (2.22a) *and* (2.22b).

Proof This is almost identical to the proof of Theorem 2.4. It requires (2.26) instead of (2.25). □

2.3.2 Double Layer Potential

The double layer potential $\mathcal{D}[\sigma] : \Omega \to \mathbb{R}$ is

$$\mathcal{D}[\sigma](\mathbf{x}) = \frac{1}{2\pi\alpha^2}\int_\Gamma \frac{\partial}{\partial \nu_{\mathbf{y}}} K_0\left(\frac{|\mathbf{y}-\mathbf{x}|}{\alpha}\right)\sigma(\mathbf{y})\, ds_{\mathbf{y}}. \tag{2.28}$$

We again assume that $\sigma \in C(\Gamma)$ to guarantee that (2.28) is well-defined. Computing the normal derivative,

$$\mathcal{D}[\sigma](\mathbf{x}) = -\frac{1}{2\pi\alpha^2}\int_\Gamma K_1\left(\frac{|\mathbf{y}-\mathbf{x}|}{\alpha}\right)\frac{(\mathbf{y}-\mathbf{x})\cdot\nu_{\mathbf{y}}}{\alpha|\mathbf{y}-\mathbf{x}|}\sigma(\mathbf{y}) ds_{\mathbf{y}}.$$

The kernel of the double layer potential is

$$K(\mathbf{y},\mathbf{x}) = -\frac{1}{2\pi\alpha^2}\frac{\partial}{\partial \nu_{\mathbf{y}}} K_0\left(\frac{|\mathbf{y}-\mathbf{x}|}{\alpha}\right).$$

Again, the double layer potential automatically satisfies the modified Helmholtz equation. The function σ is determined by the boundary condition.

Theorem 2.6 *Let $\sigma \in C(\Gamma)$. Then,*

$$u^D(\mathbf{x}) = \frac{1}{2\pi\alpha^2}\int_\Gamma \frac{\partial}{\partial \nu_{\mathbf{y}}} K_0\left(\frac{|\mathbf{y}-\mathbf{x}|}{\alpha}\right)\sigma(\mathbf{y})ds_{\mathbf{y}} \tag{2.29}$$

solves (2.21a).

Proof For $\mathbf{x} \in \Omega$,

$$(1-\alpha^2\Delta)u^D(\mathbf{x}) = (1-\alpha^2\Delta)\frac{1}{2\pi\alpha^2}\int_\Gamma \frac{\partial}{\partial \nu_{\mathbf{y}}} K_0\left(\frac{|\mathbf{y}-\mathbf{x}|}{\alpha}\right)\sigma(\mathbf{y})ds_{\mathbf{y}}.$$

When $\mathbf{x} \notin \Gamma$, the integrand is bounded, so, the integral and derivatives can be interchanged. Also, the Laplacian and the normal derivative can be interchanged since $K_0(|\mathbf{y}-\mathbf{x}|)$ is smooth away from its singularity. Thus,

$$\begin{aligned}(1-\alpha^2\Delta)u^D(\mathbf{x}) &= \frac{1}{2\pi\alpha^2}\int_\Gamma \frac{\partial}{\partial \nu_{\mathbf{y}}}(1-\alpha^2\Delta)K_0\left(\frac{|\mathbf{y}-\mathbf{x}|}{\alpha}\right)\sigma(\mathbf{y})ds_{\mathbf{y}}\\ &= \int_\Gamma \frac{\partial}{\partial \nu_{\mathbf{y}}}\delta(\mathbf{y}-\mathbf{x})\sigma(\mathbf{y})ds_{\mathbf{y}}\\ &= 0.\end{aligned}$$

□

The double layer potential satisfies (2.21a), but we have not imposed the boundary condition (2.21b). The boundary condition is satisfied by taking the limit of (2.29) as $\mathbf{x} \to \mathbf{x}_0$ and equating it with $f(\mathbf{x}_0)$. That is, we find σ such that

$$\lim_{\substack{\mathbf{x}\to\mathbf{x}_0\\ \mathbf{x}\in\Omega}} \frac{1}{2\pi\alpha^2}\int_\Gamma \frac{\partial}{\partial \nu_{\mathbf{y}}} K_0\left(\frac{|\mathbf{y}-\mathbf{x}|}{\alpha}\right)\sigma(\mathbf{y})ds_{\mathbf{y}} = f(\mathbf{x}_0)$$

for all $\mathbf{x}_0 \in \Gamma$. To compute this limit, we use the jump condition for the logarithmic kernel [23, Thm 3.22] or [35, pg 173–4]. For any $\mathbf{x}_0 \in \Gamma$,

$$\lim_{\substack{\mathbf{x}\to\mathbf{x}_0\\ \mathbf{x}\in\Omega}} \frac{1}{2\pi}\int_\Gamma \frac{\partial}{\partial \nu_{\mathbf{y}}}\log|\mathbf{y}-\mathbf{x}|\sigma(\mathbf{y})ds_{\mathbf{y}} = \frac{1}{2}\sigma(\mathbf{x}_0) + \frac{1}{2\pi}\int_\Gamma \frac{\partial}{\partial \nu_{\mathbf{y}}}\log|\mathbf{y}-\mathbf{x}_0|\sigma(\mathbf{y})ds_{\mathbf{y}}. \tag{2.30}$$

Theorem 2.7 *Suppose that σ satisfies*

$$f(\mathbf{x}_0) = -\frac{1}{2\alpha^2}\sigma(\mathbf{x}_0) + \frac{1}{2\pi\alpha^2}\int_\Gamma \frac{\partial}{\partial \nu_\mathbf{y}} K_0\left(\frac{|\mathbf{y}-\mathbf{x}_0|}{\alpha}\right)\sigma(\mathbf{y})ds_\mathbf{y}. \tag{2.31}$$

Then, the double layer potential (2.29) *satisfies* (2.21a) *and* (2.21b)*.*

Proof We have already shown that (2.29) satisfies (2.21a). We use (2.19) and (2.30) to show that it satisfies the boundary condition (2.21b)

$$\begin{aligned}
\lim_{\substack{\mathbf{x}\to\mathbf{x}_0\\ \mathbf{x}\in\Omega}} u^H(\mathbf{x}) &= \lim_{\substack{\mathbf{x}\to\mathbf{x}_0\\ \mathbf{x}\in\Omega}} \frac{1}{2\pi\alpha^2}\int_\Gamma \frac{\partial}{\partial \nu_\mathbf{y}} K_0\left(\frac{|\mathbf{y}-\mathbf{x}|}{\alpha}\right)\sigma(\mathbf{y})ds_\mathbf{y} \\
&= -\lim_{\substack{\mathbf{x}\to\mathbf{x}_0\\ \mathbf{x}\in\Omega}} \frac{1}{2\pi\alpha^2}\int_\Gamma \frac{\partial}{\partial \nu_\mathbf{y}} \log\left(\frac{|\mathbf{y}-\mathbf{x}|}{2\alpha}\right)\sigma(\mathbf{y})ds_\mathbf{y} \\
&\qquad -\lim_{\substack{\mathbf{x}\to\mathbf{x}_0\\ \mathbf{x}\in\Omega}} \frac{1}{2\pi\alpha^2}\int_\Gamma \frac{\partial}{\partial \nu_\mathbf{y}} p\left(\frac{|\mathbf{y}-\mathbf{x}|}{\alpha}\right)\log\left(\frac{|\mathbf{y}-\mathbf{x}|}{2\alpha}\right)\sigma(\mathbf{y})ds_\mathbf{y} \\
&\qquad +\lim_{\substack{\mathbf{x}\to\mathbf{x}_0\\ \mathbf{x}\in\Omega}} \frac{1}{2\pi\alpha^2}\int_\Gamma \frac{\partial}{\partial \nu_\mathbf{y}} q\left(\frac{|\mathbf{y}-\mathbf{x}|}{\alpha}\right)\sigma(\mathbf{y})ds_\mathbf{y} \qquad (2.32)\\
&= -\frac{1}{2\pi\alpha^2}\int_\Gamma \frac{\partial}{\partial \nu_\mathbf{y}} \log\left(\frac{|\mathbf{y}-\mathbf{x}_0|}{2\alpha}\right)\sigma(\mathbf{y})ds_\mathbf{y} - \frac{1}{2\alpha^2}\sigma(\mathbf{x}_0) \\
&\qquad -\frac{1}{2\pi\alpha^2}\int_\Gamma \frac{\partial}{\partial \nu_\mathbf{y}} p\left(\frac{|\mathbf{y}-\mathbf{x}_0|}{\alpha}\right)\log\left(\frac{|\mathbf{y}-\mathbf{x}_0|}{2\alpha}\right)\sigma(\mathbf{y})ds_\mathbf{y} \\
&\qquad +\frac{1}{2\pi\alpha^2}\int_\Gamma \frac{\partial}{\partial \nu_\mathbf{y}} q\left(\frac{|\mathbf{y}-\mathbf{x}_0|}{\alpha}\right)\sigma(\mathbf{y})ds_\mathbf{y} \\
&= -\frac{1}{2\alpha^2}\sigma(\mathbf{x}_0) + \frac{1}{2\pi\alpha^2}\int_\Gamma \frac{\partial}{\partial \nu_\mathbf{y}} K_0\left(\frac{|\mathbf{y}-\mathbf{x}_0|}{\alpha}\right)\sigma(\mathbf{y})ds_\mathbf{y}.
\end{aligned}$$

The last two limits in (2.32) do not exhibit any jumps since the integrand is bounded, while the first, which results in the jump term

$$-\frac{1}{2\alpha^2}\sigma(\mathbf{x}_0),$$

follows from (2.30). □

To summarize, both the single layer potential (2.24) and double layer potential (2.29) solve the modified Helmholtz equation. We have shown that the single layer potential is a continuous function as $\mathbf{x}$ passes through Γ, while its normal derivative has a jump. We also have shown that the double layer potential has a jump in its function value. We now work towards establishing existence and uniqueness of these integral equations.

2.4 Existence and Uniqueness of Solutions of the Integral Equations

For numerical reasons that become apparent in Chapter 3, in this thesis, we always use the single layer representation (2.24) when solving the Neumann problem (2.22), and we always use the double layer representation (2.29) when solving the Dirichlet problem (2.21). This means that we need to solve the integral equations (2.27) and (2.31). Here, we establish existence and uniqueness of solutions to these integral equations. We first show that the integral operators are both compact, and then establish that the homogeneous integral equations have a trivial null space. By the Fredholm Alternative, this guarantees that solutions exist and are unique. We discuss numerical methods to solve the integral equations in Chapter 3.

2.4.1 Compactness of Integral Operators

To establish compactness of the integral operators, we need to understand the nature of the singularities of the layer potentials when $\mathbf{x} \in \Gamma$. Earlier we assumed that Γ had at least two continuous derivatives. This guarantees continuity of the curvature of Γ since the curvature depends on first and second derivatives. By the following theorem, this implies that both the kernel of the double layer potential and the normal derivative of the single layer potential are continuous.

Theorem 2.8 *The kernel of the integral operators* (2.27) *and* (2.31) *are continuous and bounded on* $\Gamma \times \Gamma$. *Moreover, for all* $\mathbf{x}_0 \in \Gamma$,

$$\lim_{\substack{\mathbf{y}\to\mathbf{x}_0 \\ \mathbf{y}\in\Gamma}} \frac{\partial}{\partial \nu_{\mathbf{y}}} K_0\left(\frac{|\mathbf{y}-\mathbf{x}_0|}{\alpha}\right) = -\frac{1}{2}\kappa(\mathbf{x}_0),$$
$$\lim_{\substack{\mathbf{y}\to\mathbf{x}_0 \\ \mathbf{y}\in\Gamma}} \frac{\partial}{\partial \nu_{\mathbf{x}_0}} K_0\left(\frac{|\mathbf{y}-\mathbf{x}_0|}{\alpha}\right) = \frac{1}{2}\kappa(\mathbf{x}_0),$$

where $\kappa(\mathbf{x}_0)$ *is the curvature of* Γ *at* $\mathbf{x}_0$.

Proof For any $\mathbf{x}_0 \in \Gamma$, the kernels are continuous and bounded for all $\mathbf{y} \neq \mathbf{x}_0$. The only problematic point is $\mathbf{y} = \mathbf{x}_0$. Considering the limit of the kernel of the double layer potential

at its singularity

$$\begin{aligned}
&\lim_{\substack{\mathbf{y}\to\mathbf{x}_0\\ \mathbf{y}\in\Gamma}} \frac{\partial}{\partial\nu_{\mathbf{y}}} K_0\left(\frac{|\mathbf{y}-\mathbf{x}_0|}{\alpha}\right) \\
&\quad = \frac{\partial}{\partial\nu_{\mathbf{y}}}\left\{-\log\left(\frac{|\mathbf{y}-\mathbf{x}_0|}{2\alpha}\right) + p(|\mathbf{y}-\mathbf{x}_0|)\log\left(\frac{|\mathbf{y}-\mathbf{x}_0|}{2\alpha}\right) + q(|\mathbf{y}-\mathbf{x}_0|)\right\} \\
&\quad = -\frac{\partial}{\partial\nu_{\mathbf{y}}}\log(|\mathbf{y}-\mathbf{x}|) \\
&\quad = -\frac{1}{2}\kappa(\mathbf{x}_0),
\end{aligned}$$

we see that the kernel is in fact bounded there. The second and third terms vanished since their derivatives are 0 at the origin. The final limit is a standard potential theory result that can be found, for instance, in [18, page 199]. The limit of the normal derivative of the single layer potential follows immediately since

$$\lim_{\substack{\mathbf{y}\to\mathbf{x}_0\\ \mathbf{y}\in\Gamma}} \frac{\partial}{\partial\nu_{\mathbf{y}}} K_0\left(\frac{|\mathbf{y}-\mathbf{x}_0|}{\alpha}\right) = -\lim_{\substack{\mathbf{y}\to\mathbf{x}_0\\ \mathbf{y}\in\Gamma}} \frac{\partial}{\partial\nu_{\mathbf{x}_0}} K_0\left(\frac{|\mathbf{y}-\mathbf{x}_0|}{\alpha}\right)$$

□

From Theorem 2.8, both integral operators (2.27) and (2.31) have a bounded and continuous kernel. This guarantees that the integral operators are compact on $C(\Omega)$ [5, 18]. Thus, the Fredholm Alternative can be applied to discuss the existence and uniqueness of solutions.

2.4.2 Existence and Uniqueness of the Dirichlet Problem

Recall that we are using the double layer potential representation (2.29) to solve the boundary integral equation (2.31). To establish existence and uniqueness of solutions, we require the normal derivative of the double layer potential.

As before, we first compute the normal derivative for the double layer potential with logarithmic kernel [18, Eqn 5.7],

$$\lim_{\substack{\mathbf{x}\to\mathbf{x}_0\\ \mathbf{x}\in\Omega}} \frac{\partial}{\partial\nu_{\mathbf{x}}}\frac{1}{2\pi}\int_\Gamma \frac{\partial}{\partial\nu_{\mathbf{y}}}\log(|\mathbf{y}-\mathbf{x}|)\sigma(\mathbf{y})ds_{\mathbf{y}} = \frac{1}{2\pi}\int_\Gamma \frac{\partial^2}{\partial\nu_{\mathbf{x}_0}\partial\nu_{\mathbf{y}}}\log(|\mathbf{y}-\mathbf{x}_0|)\sigma(\mathbf{y})ds_{\mathbf{y}}. \quad (2.33)$$

That is, there is no jump in the normal derivative of the double layer potential.

Theorem 2.9 *The normal derivative the double layer potential is continuous. That is,*

$$\lim_{\substack{\mathbf{x}\to\mathbf{x}_0\\ \mathbf{x}\in\Omega}} \frac{\partial}{\partial\nu_{\mathbf{x}}}\frac{1}{2\pi\alpha^2}\int_\Gamma \frac{\partial}{\partial\nu_{\mathbf{y}}}K_0\left(\frac{|\mathbf{y}-\mathbf{x}_0|}{\alpha}\right)\sigma(\mathbf{y})ds_{\mathbf{y}} = \frac{1}{2\pi\alpha^2}\int_\Gamma \frac{\partial^2}{\partial\nu_{\mathbf{x}_0}\partial\nu_{\mathbf{y}}}K_0\left(\frac{|\mathbf{y}-\mathbf{x}_0|}{\alpha}\right)\sigma(\mathbf{y})ds_{\mathbf{y}}$$

Proof This is almost identical to the proof of Theorem 2.7. It requires (2.33) instead (2.30). □

We are now able to establish existence and uniqueness of solutions of (2.31)

Theorem 2.10 *Suppose that $f \in C(\Gamma)$. Then, there exists a unique $\sigma \in C(\Gamma)$ such that*

$$f(\mathbf{x}_0) = -\frac{1}{2\alpha^2}\sigma(\mathbf{x}_0) + \frac{1}{2\pi\alpha^2}\int_\Gamma \frac{\partial}{\partial\nu_{\mathbf{y}}}K_0\left(\frac{|\mathbf{y}-\mathbf{x}_0|}{\alpha}\right)\sigma(\mathbf{y})ds_{\mathbf{y}}.$$

That is, solutions of (2.31) *exist and are unique.*

Proof Assume that Ω is bounded. Solutions are guaranteed to be unique if the only solution of

$$-\frac{1}{2\alpha^2}\sigma(\mathbf{x}_0) + \frac{1}{2\pi\alpha^2}\int_\Gamma \frac{\partial}{\partial\nu_{\mathbf{y}}}K_0\left(\frac{|\mathbf{y}-\mathbf{x}_0|}{\alpha}\right)\sigma(\mathbf{y})ds_{\mathbf{y}} = 0 \tag{2.34}$$

is $\sigma(\mathbf{x}_0) = 0$. By the Fredholm Alternative, this also guarantees the existence of a solution. Suppose that $\sigma \in C(\Gamma)$ solves (2.34) and let $u(\mathbf{x})$ be the double layer potential associated with σ

$$u(\mathbf{x}) = \frac{1}{2\pi\alpha^2}\int_\Gamma \frac{\partial}{\partial\nu_{\mathbf{y}}}K_0\left(\frac{|\mathbf{y}-\mathbf{x}|}{\alpha}\right)\sigma(\mathbf{y})ds_{\mathbf{y}}, \quad \mathbf{x}\in\Omega. \tag{2.35}$$

Then, $(1-\alpha^2\Delta)u = 0$ in Ω and $u = 0$ on Γ. We already established uniqueness of solutions of this PDE, so we are guaranteed that $u = 0$. Now consider $u(\mathbf{x})$ given by (2.35) for $\mathbf{x} \in \mathbb{R}^2\backslash\overline{\Omega}$. Then, $(1-\alpha^2\Delta)u = 0$ in $\mathbb{R}^2\backslash\overline{\Omega}$ and $|u(\mathbf{x})| \to 0$ as $|\mathbf{x}| \to \infty$. By continuity of the normal derivative of u, u has a homogeneous Neumann boundary condition on Γ. We established uniqueness of solutions of this PDE as well, so we are guaranteed that $u = 0$ in $\mathbb{R}^2\backslash\Gamma$. Fixing a point $\mathbf{x}_0 \in \Gamma$, we consider the limit of u from both sides of Γ.

$$0 = \lim_{\substack{\mathbf{x}\to\mathbf{x}_0\\ \mathbf{x}\in\Omega}} u(\mathbf{x}) = -\frac{1}{2\alpha^2}\sigma(\mathbf{x}_0) + \frac{1}{2\pi\alpha^2}\int_\Gamma \frac{\partial}{\partial\nu_{\mathbf{y}}}K_0\left(\frac{|\mathbf{y}-\mathbf{x}_0|}{\alpha}\right)\sigma(\mathbf{y})ds_{\mathbf{y}}$$

$$0 = \lim_{\substack{\mathbf{x}\to\mathbf{x}_0\\ \mathbf{x}\in\mathbb{R}^2\backslash\overline{\Omega}}} u(\mathbf{x}) = \frac{1}{2\alpha^2}\sigma(\mathbf{x}_0) + \frac{1}{2\pi\alpha^2}\int_\Gamma \frac{\partial}{\partial\nu_{\mathbf{y}}}K_0\left(\frac{|\mathbf{y}-\mathbf{x}_0|}{\alpha}\right)\sigma(\mathbf{y})ds_{\mathbf{y}}.$$

The opposing signs of the jump terms occur since the exterior problem has an inward pointing normal. Subtracting the two equations gives $\sigma(\mathbf{x}_0) = 0$. If Ω is unbounded, the only change to the proof is that the condition at infinity holds in Ω rather than in $\mathbb{R}^2\backslash\overline{\Omega}$. □

2.4.3 Existence and Uniqueness of the Neumann Problem

Using the single layer potential (2.24) for the Neumann problem results in the boundary integral equation (2.27). We use the Fredholm Alternative and the continuity of the single layer potential to establish existence and uniqueness of solutions of (2.27)

Theorem 2.11 *Suppose that $f \in C(\Gamma)$. Then, there exists a unique $\sigma \in C(\Gamma)$ such that*

$$f(\mathbf{x}_0) = \frac{1}{2\alpha^2}\sigma(\mathbf{x}_0) + \frac{1}{2\pi}\int_\Gamma \frac{\partial}{\partial \nu_{\mathbf{x}_0}} K_0\left(\frac{|\mathbf{y}-\mathbf{x}_0|}{\alpha}\right)\sigma(\mathbf{y})ds_{\mathbf{y}}.$$

That is, solutions of (2.27) *exist and are unique.*

Proof The proof is almost identical to that of Theorem 2.10. By the same argument made earlier, we can assume that Ω is bounded. Suppose that σ solves

$$\frac{1}{2\alpha^2}\sigma(\mathbf{x}_0) + \frac{1}{2\pi\alpha^2}\int_\Gamma \frac{\partial}{\partial \nu_{\mathbf{x}_0}} K_0\left(\frac{|\mathbf{y}-\mathbf{x}_0|}{\alpha}\right)\sigma(\mathbf{y})ds_{\mathbf{y}} = 0.$$

Define $u(\mathbf{x})$ for $\mathbf{x} \in \Omega$ by the single layer potential

$$u(\mathbf{x}) = \frac{1}{2\pi\alpha^2}\int_\Gamma K_0\left(\frac{|\mathbf{y}-\mathbf{x}|}{\alpha}\right)\sigma(\mathbf{y})ds_{\mathbf{y}}, \quad \mathbf{x} \in \Omega. \tag{2.36}$$

Then, u satisfies $(1-\alpha^2\Delta)u = 0$ in Ω with homogeneous Neumann boundary conditions, hence, $u = 0$ in Ω. As we did in the Dirichlet case, we define $u(\mathbf{x})$ in $\mathbb{R}^2\backslash\overline{\Omega}$ by (2.36). As the single layer potential is a continuous function in $\mathbb{R}^2$, $(1-\alpha^2\Delta)u = 0$ in $\mathbb{R}^2\backslash\overline{\Omega}$, $u = 0$ on Γ, and $u(\mathbf{x}) \to 0$ as $|\mathbf{x}| \to \infty$. Thus, $u = 0$ in $\mathbb{R}^2\backslash\overline{\Omega}$. Fixing a point $\mathbf{x}_0 \in \Gamma$, we consider the limit of the normal derivative of u from both sides of Γ

$$0 = \lim_{\substack{\mathbf{x}\to\mathbf{x}_0 \\ \mathbf{x}\in\Omega}} \frac{\partial}{\partial \nu_{\mathbf{x}_0}} u(\mathbf{x}) = \frac{1}{2\alpha^2}\sigma(\mathbf{x}_0) + \frac{1}{2\pi\alpha^2}\int_\Gamma \frac{\partial}{\partial \nu_{\mathbf{x}_0}} K_0\left(\frac{|\mathbf{y}-\mathbf{x}_0|}{\alpha}\right)\sigma(\mathbf{y})ds_{\mathbf{y}}$$

$$0 = \lim_{\substack{\mathbf{x}\to\mathbf{x}_0 \\ \mathbf{x}\in\mathbb{R}^2\backslash\overline{\Omega}}} \frac{\partial}{\partial \nu_{\mathbf{x}_0}} u(\mathbf{x}) = -\frac{1}{2\alpha^2}\sigma(\mathbf{x}_0) + \frac{1}{2\pi\alpha^2}\int_\Gamma \frac{\partial}{\partial \nu_{\mathbf{x}_0}} K_0\left(\frac{|\mathbf{y}-\mathbf{x}_0|}{\alpha}\right)\sigma(\mathbf{y})ds_{\mathbf{y}}.$$

Subtracting the two equations gives $\sigma(\mathbf{x}_0) = 0$. □

We have established both existence and uniqueness of solutions of the integral equations corresponding to (2.21) and (2.22). Thus, we have also established existence of solutions of the homogeneous modified Helmholtz equation.

2.5 Summary

It is worth noting that when solving Laplace's equation, the proofs of Theorems 2.10 and 2.11 break down when the domain is either multiply-connected or unbounded. In fact, in [18], it is assumed that Ω is a simply-connected bounded domain. If the domain is multiply-connected and the boundary condition is Dirichlet, then $\mathbb{R}^2\backslash\overline{\Omega}$ contains bounded disjoint regions. Inside each of these regions, u solves $\Delta u = 0$ with a homogeneous Neumann boundary condition. Since $u = 0$ is not the only solution to this problem, the proof breaks down. However, for the modified Helmholtz equation, inside each of these components, u must satisfy $(1-\alpha^2\Delta)u = 0$ with a homogeneous Neumann boundary condition. This PDE does have a unique solution, namely $u = 0$. The assumption that Ω is bounded can also be dropped when solving the modified Helmholtz equation. It is possible to formulate integral equations to solve Laplace's equation in multiply-connected or unbounded domains. One such formulation, which requires the addition of Lagrange-type multipliers, is found in [24].

We have established existence and uniqueness of solutions of (2.27) and (2.31). However, closed-form solutions hardly ever exist, thus, we resort to numerical solutions in Chapter 3. We note here that the two integral equations we have formulated are very similar. The first difference is the change in the sign in the jump condition. The second difference is the variable where the normal derivative is taken. These similarities are exploited when developing numerical solvers. In particular, a few small changes to a numerical solver for (2.31) establishes a numerical solver for (2.27).

Chapter 3

Numerical Solutions of the Integral Equations

We are interested in solving the integral equations that correspond to the PDEs (2.21) and (2.22). In this chapter, we drop the superscript and write u instead of u^H. With the ansätze we have chosen, the integral equations of interest are (2.31) and (2.27). Both equations can be written in the general form:

$$f(\mathbf{x}) = \lambda\sigma(\mathbf{x}) + \int_\Gamma K(\mathbf{y}, \mathbf{x})\sigma(\mathbf{y})ds_\mathbf{y} \tag{3.1}$$

with $\lambda \neq 0$. Equation (3.1) is a Fredholm integral equation of the second kind with a bounded kernel. From Chapter 2, we know a unique solution of (3.1) exists. However, closed-form solutions are difficult or impossible to obtain. Thus, numerical solutions must be sought.

The most straightforward discretization of (3.1) is the trapezoidal rule. We will see in Section 3.1 that it is surprisingly accurate if the kernel K is sufficiently smooth. Unfortunately, the kernels considered in this thesis are not smooth. Thus, we resort to high-order quadrature rules designed for functions with logarithmic singularities in Section 3.2. Using either discretization technique, if N is the total number of discretization points, the result is a dense $N \times N$ linear system. A solution strategy and properties of these linear systems are discussed. Upon solving the linear system, we evaluate $u(\mathbf{x})$ for $\mathbf{x} \in \Omega$ since these values are required by the volume integral at subsequent time steps. As points $\mathbf{x} \in \Omega$ approach Γ, an unbounded number of discretization points are required to maintain a uniform bound on the error. Therefore, a near-singular integration strategy which numerically integrates the

layer potentials with uniform error is introduced in Section 3.3. Several numerical examples in Section 3.4 demonstrate the desired properties of the numerical solution.

3.1 The Trapezoidal Rule

The most naive approach to solve (3.1) is to use the trapezoidal rule. We now show that with assumptions on the smoothness of the kernel of the integral operator, the trapezoidal rule gives high accuracy. For an interval $[a, b]$, the trapezoidal rule is

$$T_N(f) = \frac{\Delta x}{2} f(a) + \Delta x \sum_{i=1}^{N-1} f(x_j) + \frac{\Delta x}{2} f(b)$$

where $x_j = a + j\Delta x$ and $\Delta x = (b - a)/N$. When $f \in C^2[a, b]$, the trapezoidal rule is second-order since there exists a number $\xi \in [a, b]$ with

$$\left| \int_a^b f(x)dx - T_N(f) \right| = \frac{b-a}{12N^2} f''(\xi).$$

However, the error is significantly reduced if f is periodic. If $[a, b] = [0, 2\pi]$ and f is periodic,

$$T_N(f) = \Delta x \sum_{j=0}^{N-1} f(x_j)$$

where $x_j = j\Delta x$ and $\Delta x = 2\pi/N$. The error is

$$\int_0^{2\pi} f(x)dx - T_N(f) = 2\pi \sum_{\substack{k\in\mathbb{Z} \\ k\neq 0}} \hat{f}(kN), \tag{3.2}$$

where

$$\hat{f}(n) = \frac{1}{2\pi} \int_0^{2\pi} f(x)e^{-inx}dx.$$

Thus, the error of the trapezoidal rule decays at the same rate as the Fourier coefficients (spectrum) of f. Equation (3.2) follows from the following well-known theorem [46].

Theorem 3.1 *If n is not an integer multiple of N,*

$$T_N(e^{inx}) = 0.$$

If n is an integer multiple of N,

$$T_N(e^{inx}) = 2\pi.$$

Since Γ_k is a closed curve, continuous functions defined on Γ_k are periodic. Therefore, solving (3.1) with the trapezoidal rule gives the same accuracy as a Fourier method. We parameterize each component curve by

$$\Gamma_k = \{\mathbf{r}^k(\theta) \mid 0 \leq \theta < 2\pi\}, \quad k = 0, \ldots, M,$$

and use N equispaced points with respect to θ,

$$\theta_i = (i-1)\Delta\theta, \quad i = 1, \ldots, N,$$

where $\Delta\theta = 2\pi/N$. The total number of discretization points is $N(M+1)$ and the trapezoidal rule applied to (3.1) is

$$f(\mathbf{r}^k(\theta_j)) = \lambda\sigma(\mathbf{r}^k(\theta_j)) + \frac{1}{2\pi\alpha^2}\sum_{m=0}^{M}\sum_{n=1}^{N} K(\mathbf{r}^m(\theta_n), \mathbf{r}^k(\theta_j))\sigma(\mathbf{r}^m(\theta_n))|\mathbf{r}'^m(\theta_n)|\Delta\theta,$$

where $k = 0, \ldots, M$ and $j = 1, \ldots, N$. If the domain is unbounded, the index for m starts at 1 rather than 0, and there is a total of NM points. We simplify notation by writing

$$\begin{aligned} f_j^k &= f(\mathbf{r}^k(\theta_j)), \\ \sigma_j^k &= \sigma(\mathbf{r}^k(\theta_j)), \\ K_{j,n}^{k,m} &= \frac{1}{2\pi\alpha^2} K(\mathbf{r}^m(\theta_n), \mathbf{r}^k(\theta_j))|\mathbf{r}'^m(\theta_n)|\Delta\theta, \end{aligned}$$

resulting in the linear system

$$f_j^k = \lambda\sigma_j^k + \sum_{m=0}^{M}\sum_{n=1}^{N} K_{j,n}^{k,m}\sigma_n^m, \quad k = 0, \ldots, M,\ j = 1, \ldots, N. \tag{3.3}$$

We note that the linear system corresponding to (3.3) is dense. This is a result of the kernel K being nonzero for two arbitrary points on Γ.

The trapezoidal rule applied to (3.1) is straightforward to implement, but, it can only converge as fast as the spectrum of the integral operator. Unfortunately, the spectrum of integral operators involving K_0 decay slowly with respect to N which we illustrate with the following example.

Let Ω be the ellipse with radii 1 and $a > 1$ and let $\mathbf{x}_0 = (1, 0) \in \Gamma$. Then,

$$\begin{aligned} |\mathbf{y} - \mathbf{x}_0|^2 &= (1 - a^2)\cos^2(\theta) - 2\cos(\theta) + (1 + a^2), \\ |\mathbf{y}'|(\mathbf{y} - \mathbf{x}_0) \cdot \nu_{\mathbf{y}} &= a - a\cos(\theta). \end{aligned}$$

We apply the trapezoidal rule to

$$\begin{aligned} f_1(\theta) &= \frac{\partial}{\partial \nu_{\mathbf{y}}} \log|\mathbf{y}-\mathbf{x}_0||\mathbf{y}'| \\ &= \frac{(\mathbf{y}-\mathbf{x}_0)\cdot\nu_{\mathbf{y}}}{|\mathbf{y}-\mathbf{x}_0|^2}|\mathbf{y}'| \\ &= \frac{a-a\cos(\theta)}{(1-a^2)\cos^2(\theta)-2\cos(\theta)+(1+a^2)} \\ &= \frac{a}{(1+a^2)-(1-a^2)\cos(\theta)}, \end{aligned}$$

and

$$\begin{aligned} f_2(\theta) &= -\frac{\partial}{\partial \nu_{\mathbf{y}}} K_0(|\mathbf{y}-\mathbf{x}_0|)|\mathbf{y}'| \\ &= \frac{K_1(|\mathbf{y}-\mathbf{x}_0|)}{|\mathbf{y}-\mathbf{x}_0|}(\mathbf{y}-\mathbf{x}_0)\cdot\nu_{\mathbf{y}}|\mathbf{y}'| \\ &= \frac{K_1\left(\sqrt{(1-a^2)\cos^2(\theta)-2\cos(\theta)+(1+a^2)}\right)}{\sqrt{(1-a^2)\cos^2(\theta)-2\cos(\theta)+(1+a^2)}}(a-a\cos(\theta)) \\ f_2(0) &= \frac{1}{2a}. \end{aligned}$$

f_1 and f_2 are kernels of the double layer potential for Laplace's equation and the modified Helmholtz equation evaluated at $\mathbf{x}_0$. We choose $f_2(0)$ so that f_2 is continuous for all $\theta \in [0, 2\pi)$. The functions are illustrated in the top plots of Figure 3.1 and 3.2.

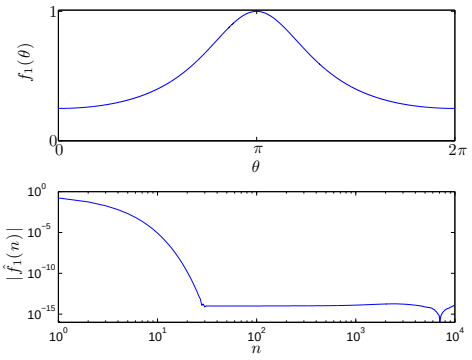

Figure 3.1: The function $f_1(\theta)$ (top) and the absolute value of its Fourier coefficients (bottom) when $a = 2$.

When $a = 2$, the Fourier coefficients of f_1 drop below machine precision well before the 100^{th} Fourier mode, thus, we expect the error of the trapezoidal rule to decay quickly

with respect to N. The Fourier coefficients of f_1 can be computed exactly using the residue theorem. Letting C be the unit circle in the complex plane,

$$\begin{aligned}\hat{f}_1(n) &= \frac{1}{2\pi}\int_0^{2\pi} f_1(\theta)e^{-in\theta}d\theta \\ &= \frac{1}{2\pi}\oint_C \frac{z^{-n}dz}{iz}\frac{a}{(1+a^2)-\frac{1-a^2}{2}(z+z^{-1})} \\ &= \frac{ai}{\pi}\oint_C \frac{z^{-n}dz}{(1-a^2)z^2-2z(1+a^2)+(1-a^2)}.\end{aligned}$$

When $n \leq 0$, there are two simple poles at

$$z_1 = \frac{1-a}{1+a}, \qquad z_2 = \frac{1+a}{1-a}.$$

Since z_1 is inside C and z_2 is not, the residue theorem yields

$$\begin{aligned}\hat{f}_1(n) &= \frac{\frac{ai}{\pi(1-a^2)}2\pi i\left(\frac{1-a}{1+a}\right)^{-n}}{\frac{1-a}{1+a}-\frac{1+a}{1-a}} \\ &= \frac{1}{2}\left(\frac{1-a}{1+a}\right)^{-n}.\end{aligned}$$

Since f_1 is real-valued, $\hat{f}_1(n) = \overline{\hat{f}_1(-n)}$. Thus,

$$\hat{f}_1(n) = \frac{1}{2}\left(\frac{1-a}{1+a}\right)^{|n|} \quad n \in \mathbb{Z}.$$

For N even, the error of the trapezoidal rule is

$$\begin{aligned}\int_0^{2\pi} f_1(\theta)d\theta - T_N(f_1) &= 2\pi\sum_{\substack{k\in\mathbb{Z}\\k\neq 0}}\frac{1}{2}\left(\frac{1-a}{1+a}\right)^{|kN|} \\ &= 2\pi\sum_{k=1}^{\infty}\left(\left(\frac{a-1}{a+1}\right)^N\right)^k \\ &= 2\pi\frac{\left(\frac{a-1}{a+1}\right)^N}{1-\left(\frac{a-1}{a+1}\right)^N} \\ &= 2\pi\frac{(a-1)^N}{(a+1)^N-(a-1)^N}.\end{aligned}$$

To guarantee the trapezoidal rule will have error ϵ, we take

$$N = \frac{\log\left(\frac{\epsilon}{2\pi+\epsilon}\right)}{\log(a-1)-\log(a+1)}.$$

N	Computed Error	Predicted Error
2	7.85×10^{-1}	7.85×10^{-1}
4	7.85×10^{-2}	7.85×10^{-2}
8	9.58×10^{-4}	9.58×10^{-4}
16	1.46×10^{-7}	1.46×10^{-7}
32	3.55×10^{-15}	3.39×10^{-15}
64	8.88×10^{-16}	1.83×10^{-30}
128	2.22×10^{-15}	5.33×10^{-61}

Table 3.1: The computed error and the infinite sum (3.2) applied to $f_1(\theta)$ when $a = 2$. From equation (3.2), the errors agree until machine precision when the error of the trapezoidal rule plateaus.

The error of the trapezoidal rule applied to f_1 is summarized in Table 3.1. For comparison, we compute the infinite sum (3.2). The two values agree until machine precision when the computed error plateaus. We expect this to happen when

$$\begin{aligned} N &= \frac{\log\left(\frac{10^{-16}}{2\pi+10^{-16}}\right)}{-\log(3)} \\ &\approx 35.2. \end{aligned}$$

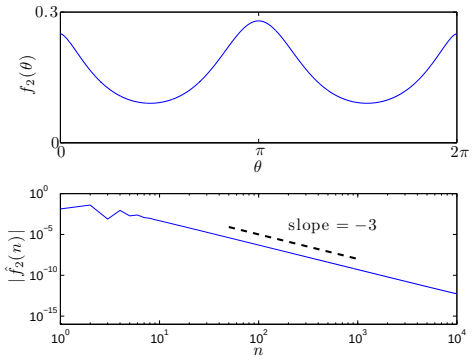

Figure 3.2: The function $f_2(\theta)$ (top) and the absolute value of its Fourier coefficients (bottom) when $a = 2$. The plot suggests $|\hat{f}_2(n)| \sim n^{-3}$.

We now analyze the error of the trapezoidal rule applied to f_2. From the bottom plot of Figure 3.2, we see that $|\hat{f}_2(n)| = \mathcal{O}(n^{-3})$. This rate of decay suggests that $f_2 \in$

N	Computed Error	Predicted Error
2	6.71×10^{-1}	1.49×10^{-2}
4	1.28×10^{-1}	8.64×10^{-2}
8	1.44×10^{-2}	1.81×10^{-2}
16	1.81×10^{-3}	2.00×10^{-3}
32	2.30×10^{-4}	2.52×10^{-4}
64	2.88×10^{-5}	3.19×10^{-5}
128	3.60×10^{-6}	4.01×10^{-6}

Table 3.2: The computed error and a predicted error of the trapezoidal rule applied to $f_2(\theta)$ when $a = 2$. The error reduces by a factor of 8 when N is doubled. We list the N^{th} Fourier coefficient which scales with the computed error.

$C^1[0, 2\pi) \backslash C^2[0, 2\pi)$. This is the case since

$$\lim_{\theta \to 0} f_2(\theta) = \frac{1}{4},$$
$$\lim_{\theta \to 0} f_2'(\theta) = 0,$$
$$\lim_{\theta \to 0} f_2''(\theta) = -\infty.$$

To apply the trapezoidal rule to f_2, we would like an exact value for its integral. However, we do not have this value, so, we use an approximate with 30 digits accuracy. The results are summarized in Table 3.2. We do not have an expression for the spectrum of f_2, so we can not compute the error exactly. However, we can use the N^{th} Fourier coefficient of f_2 as a gauge for the error of the trapezoidal rule.

Summarizing, the trapezoidal rule applied to (3.1) converges at the same rate as a Fourier method. Since $f_1 \in C^\infty[0, 2\pi)$, the trapezoidal rule converges spectrally, that is, faster than any power of N^{-1}. However, the function $f_2 \in C^1[0, 2\pi)$ and so the trapezoidal rule is only a third-order method. This motivates using high-order, specialized quadrature rules adapted for the nature of the singularity.

3.2 High-Order Quadrature Rules

The trapezoidal rule applied to f_2 demonstrates the need for high-order quadrature rules to compute integrals involving K_0. Because of (2.19), we implement quadrature rules designed for functions with a logarithmic singularity introduced by Bradley Alpert [2]. Suppose we

N	Trapezoidal	$p = 4$	$p = 8$	$p = 12$	$p = 16$
2	6.71×10^{-1}	1.44×10^{-2}	2.71×10^{-5}	3.65×10^{-7}	5.27×10^{-10}
4	1.28×10^{-1}	1.75×10^{-3}	3.18×10^{-6}	4.15×10^{-8}	6.00×10^{-11}
8	1.44×10^{-2}	3.51×10^{-5}	3.77×10^{-8}	5.28×10^{-10}	1.24×10^{-12}
16	1.81×10^{-3}	5.49×10^{-6}	7.53×10^{-10}	8.07×10^{-13}	1.24×10^{-12}
32	2.30×10^{-4}	5.78×10^{-7}	5.45×10^{-12}	9.45×10^{-13}	4.18×10^{-13}
64	2.88×10^{-5}	3.59×10^{-8}	3.82×10^{-13}	8.41×10^{-13}	1.62×10^{-13}
128	3.60×10^{-6}	1.74×10^{-9}	2.90×10^{-13}	2.30×10^{-13}	2.16×10^{-13}

Table 3.3: The quadrature error for integrating f_2. The order of convergence is $\mathcal{O}(h^p \log h)$. For comparison, we rewrite the error of the trapezoidal rule. As desired, Alpert's quadrature rules reduce the error.

wish to compute

$$\int_0^{2\pi} f(\theta) d\theta,$$

where $f(\theta)$ is periodic with a logarithmic singularity at $\theta = 0$. Alpert's quadrature rules are

$$\int_0^{2\pi} f(\theta) \approx h \sum_{i=1}^{\ell} u_i f(v_i h) + \sum_{i=0}^{n-1} f(ah + ih) + h \sum_{i=1}^{\ell} u_i f(2\pi - v_i h). \tag{3.4}$$

The error is $\mathcal{O}(h^p \log h)$, a is a positive integer, the grid spacing is $h = (n + 2a - 1)^{-1}$, and the quadrature weights u_i and nodes v_i, $i = 1, \ldots, \ell$ all depend on the choice of p.

The nodes and weights developed in [2] are found by numerically solving a nonlinear system of equations. Alpert establishes both uniqueness and existence of such solutions. He uses an iterative method outlined in [39] to solve the system of equations in quadratic time. Rules have been published for p ranging from 2 to 16.

We test the quadrature rules on f_2, varying both n and p. From Table 3.3, we see that high accuracy is easy to achieve if p is sufficiently large. For comparison, we also rewrite the computed error from the trapezoidal rule (Table 3.2). As desired, we see a significant increase in the accuracy and are able to establish 13 digits accuracy.

We now discretize (3.1) using Alpert's quadrature rules. For $k = 0, \ldots, M$ and $j =$

$1, \ldots, N$,

$$
\begin{aligned}
f(\mathbf{r}^k(\theta_j)) &= \lambda\sigma(\mathbf{r}^k(\theta_j)) \\
&+ \frac{1}{2\pi\alpha^2}\sum_{\substack{m=0\\ m\neq k}}^{M}\sum_{n=1}^{N} K(\mathbf{r}^m(\theta_n),\mathbf{r}^k(\theta_j))\sigma(\mathbf{r}^m(\theta_n))|\mathbf{r}'^m(\theta_n)|\Delta\theta \\
&+ \frac{1}{2\pi\alpha^2}\sum_{n=j+a}^{N+j-a} K(\mathbf{r}^k(\theta_n),\mathbf{r}^k(\theta_j))\sigma(\mathbf{r}^k(\theta_n))|\mathbf{r}'^k(\theta_n)|\Delta\theta \\
&+ \frac{1}{2\pi\alpha^2}\sum_{n=1}^{\ell} u_n K(\mathbf{r}^k(\theta_j+v_n\Delta\theta),\mathbf{r}^k(\theta_j))\sigma(\mathbf{r}^k(\theta_j+v_n\Delta\theta))|\mathbf{r}'^k(\theta_j+v_n\Delta\theta)|\Delta\theta \\
&+ \frac{1}{2\pi\alpha^2}\sum_{n=1}^{\ell} u_n K(\mathbf{r}^k(\theta_j-v_n\Delta\theta),\mathbf{r}^k(\theta_j))\sigma(\mathbf{r}^k(\theta_j-v_n\Delta\theta))|\mathbf{r}'^k(\theta_j-v_n\Delta\theta)|\Delta\theta. \qquad (3.5)
\end{aligned}
$$

The first summation is the trapezoidal rule applied to points not on Γ_k. The second summation is the second term of (3.4) applied to Γ_k; it is the trapezoidal rule outside of a window surrounding $\mathbf{r}^k(\theta_j)$. The final two summations are the first and third terms of (3.4). In the second summation of (3.5), we invoke periodicity of all functions defined on Γ_k, or equivalently, $j+N=j$. In the final two summations of (3.5), we are required to know values of σ intermediate to the nodal values. In these cases, we use Fourier interpolation.

Fix k and n and suppose we require $\sigma(\mathbf{r}^k(\theta_j+v_n\Delta\theta))$ in the third summation of (3.5). Suppose we know $\sigma(\mathbf{r}^k(\theta_j))$ for all $j=1,\ldots,N$. Since σ restricted to Γ_k is a periodic function, we can compute its Fourier series

$$\sigma(\mathbf{r}^k(\theta)) \approx \sum_{m=-N/2}^{N/2-1}\hat{\sigma}_k(m)e^{im\theta},$$

where

$$\hat{\sigma}_k(m) = \frac{1}{2\pi}\sum_{j=1}^{N}\sigma(\mathbf{r}^k(\theta_j))e^{-im\theta}, \quad m=-N/2,\ldots,N/2-1.$$

Then,

$$
\begin{aligned}
\sigma(\mathbf{r}^k(\theta_j+v_n\Delta\theta)) &\approx \sum_{m=-N/2}^{N/2-1}\hat{\sigma}_k(m)e^{im(\theta_j+v_n\Delta\theta)} \\
&= \sum_{m=-N/2}^{N/2-1}\hat{\sigma}_k(m)e^{imv_n\Delta\theta}e^{im\theta_j},
\end{aligned}
$$

which is also a Fourier series with Fourier coefficients $\hat{\sigma}_k(m)e^{imv_n\Delta\theta}$. Using an inverse Fourier transform, $\sigma(\mathbf{r}^k(\theta_j + v_n\Delta\theta))$ is computed for all $j = 1, \ldots, N$. To compute $\sigma(\mathbf{r}^k(\theta_j \pm v_n\Delta\theta))$ for all $n = 1, \ldots, N$, $m = 0, \ldots, M$, and $k = 1, \ldots, \ell$ requires $M + 1$ forward Fourier transforms and $2\ell(M + 1)$ inverse Fourier transforms. All the Fourier transforms are of size N.

Using Fourier interpolation, we have not formulated the problem as a linear system, but rather have made it suitable for an iterative solver. If constructing the linear system is desired, as an alternative to Fourier interpolation, we could use Lagrange interpolation as is suggested in [2]. This is straightforward to implement and results in a linear system resembling (3.3). However, it is very unstable when a high-order interpolant is used or the geometry becomes complex.

We have discretized the integral equation (3.1) with either (3.3) or (3.5). Now we must solve the linear system, which in both cases is dense. Gaussian elimination would require $\mathcal{O}(N^3(M+1)^3)$ operations which is far too slow for problems we are considering. We resort to the iterative solver generalized minimal residual method (GMRES) [45]. The bulk of the work at each GMRES iteration is applying the matrix to a vector. As this matrix is dense, a direct matrix-vector multiplication would require $\mathcal{O}(N^2(M+1)^2)$ operations. While this is an improvement over Gaussian elimination, the matrix-vector multiplication can be reduced to $\mathcal{O}(N(M+1))$ or $\mathcal{O}(N(M+1)\log(N(M+1)))$ using the fast multipole method (FMM) discussed in Chapter 5. As a note, the matrix is never actually formed. Rather, we construct a function that takes $N(M+1)$ values of σ and returns the right-hand-side of either (3.3) or (3.5).

The condition number of the linear system is important to determining the performance of GMRES, so, we consider the condition number of the linear systems (3.3) and (3.5). Since the integral operators are compact, the eigenvalues cluster at the origin. Thus, discretizations of (3.1) cluster at $\lambda \neq 0$. As N increases, the largest and smallest eigenvalues in absolute value converge; hence, the spectrum is bounded. This guarantees a bound independent of N on the condition number of (3.3) and (3.5) (see Figure 3.3). With this property, we expect that the number of required GMRES steps is bounded independent of N. The numerical examples in Section 3.4 demonstrate this property.

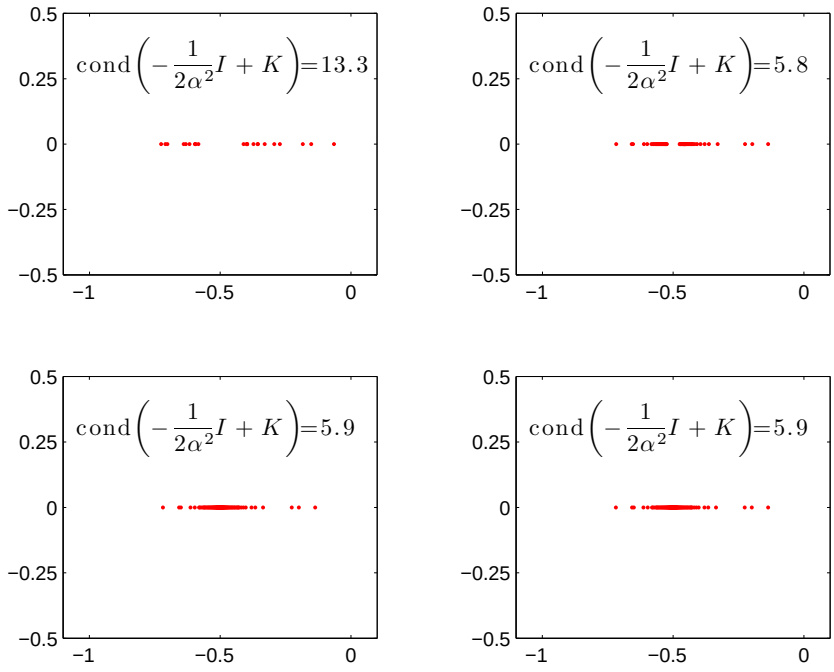

Figure 3.3: The eigenvalues and condition number of a 2-ply-connected exterior domain. The values of N reading left to right then top to bottom are 16, 32, 64, and 128. The eigenvalues cluster at $\lambda = 1/2\alpha^2$ ($\alpha = 1$ in this example) and the condition number remains bounded.

3.3 Near-Singular Integration

Once $\sigma(\mathbf{r}^k(\theta_j))$ is computed, we need to accurately evaluate the single-layer or double-layer potential at points $\mathbf{x} \in \Omega$. These values are required in Rothe's method since the volume integral that is computed at each time step requires values of the solution from previous time steps (2.5). In this section, we work with the double layer potential (2.29) in a bounded domain; the single layer potential (2.24) works similarly. Since $\mathbf{x} \notin \Gamma$, the kernel of the double layer potential is smooth; thus, the trapezoidal rule has spectral accuracy. However, for fixed N, as $\mathbf{x}$ approaches Γ, the error in the trapezoidal rule increases. In fact, the trapezoidal rule does not converge uniformly in Ω.

Figure 3.4 shows plots of

$$u_i(\theta) = \frac{1}{2\pi} \frac{K_1\left(|(\cos(\theta), \sin(\theta)) - \mathbf{x}_i|\right)}{|(\cos(\theta), \sin(\theta)) - \mathbf{x}_i|} (1 - (\cos(\theta), \sin(\theta)) \cdot \mathbf{x}_i) \quad i = 1, \ldots, 4.$$

These functions are integrated when evaluating the double layer potential of the unit circle. The points $\mathbf{x}_1$, $\mathbf{x}_2$, $\mathbf{x}_3$, and $\mathbf{x}_4$ are distance 0.2, 0.15, 0.1, and 0.05 from $(-1, 0)$. As $\mathbf{x}$ approaches Γ, we see a boundary layer forming at $\theta = \pi$. Moreover, the Fourier coefficients take longer to decay below a fixed threshold. To achieve machine precision, $N = 200$ is sufficient for $\mathbf{x}_1$, while $N \approx 1000$ is required for $\mathbf{x}_4$.

Near-singular integration is a difficult problem and has been considered in the past by Helsing and Ojala [32] and references therein, Cheng and Greengard [15], Biros et. al. [50], and Beale and Lai [7]. The work in [15, 32] is applied to integral equations arising from Laplace's equation. It is not immediately clear how to extend this work to other kernels. The work in [7] performs a smoothing of the singularity and then adds corrections. These corrections are found by doing a careful asymptotic analysis. While this could be done for the modified Helmholtz equation, numerical results in [7] indicate that no more than six digits of accuracy are ever achieved.

To bound the error in Ω uniformly, we adopt the strategy from [50]. Let $\sigma_k : \Gamma_k \to \mathbb{R}$

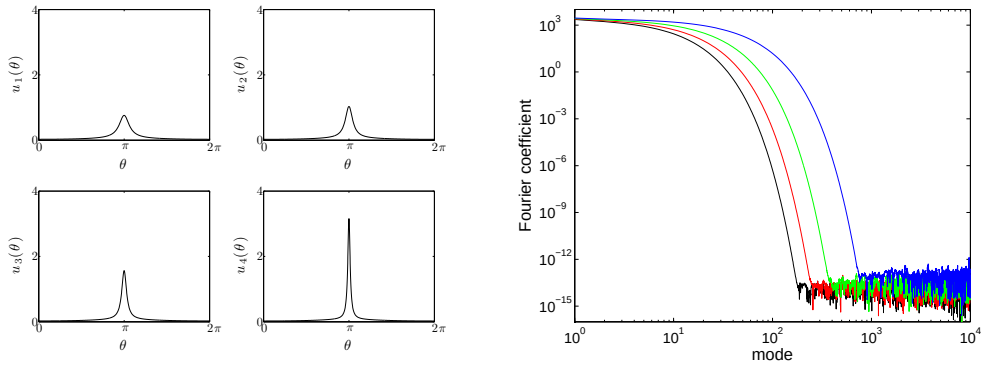

Figure 3.4: The left plots are the double layer potentials for four values of $\mathbf{x}$ approaching Γ. The distances in decreasing order are 0.2, 0.15, 0.1, 0.05. The right plot is the absolute value of the spectrums of u_1, u_2, u_3, and u_4. The black plot corresponds to distance 0.2, the red to distance 0.15, the green to distance 0.1, and the blue to distance 0.05.

be the restriction of σ to Γ_k, $k = 0, \ldots, M$. The double layer potential is decomposed as

$$\begin{aligned} u(\mathbf{x}) &= \frac{1}{2\pi\alpha^2} \int_\Gamma \frac{\partial}{\partial \nu_y} K_0 \left(\frac{|\mathbf{y} - \mathbf{x}|}{\alpha} \right) \sigma(\mathbf{y}) ds_{\mathbf{y}} \\ &= \frac{1}{2\pi\alpha^2} \sum_{k=0}^{M} \int_{\Gamma_k} \frac{\partial}{\partial \nu_{\mathbf{y}}} K_0 \left(\frac{|\mathbf{y} - \mathbf{x}|}{\alpha} \right) \sigma_k(\mathbf{y}) ds_{\mathbf{y}} \\ &= \sum_{k=0}^{M} u_k(\mathbf{x}), \end{aligned}$$

where

$$u_k(\mathbf{x}) = \frac{1}{2\pi\alpha^2} \int_{\Gamma_k} \frac{\partial}{\partial \nu_{\mathbf{y}}} K_0 \left(\frac{|\mathbf{y} - \mathbf{x}|}{\alpha} \right) \sigma_k(\mathbf{y}) ds_{\mathbf{y}}.$$

Let h_k be the maximum distance in arclength between two successive points on Γ_k and assume $h_k < 1$. Define the three regions

$$\begin{aligned} \Omega_k^2 &:= \{\mathbf{x} \in \Omega \mid \operatorname{dist}(\mathbf{x}, \Gamma_k) \in (\sqrt{h_k}, \infty)\}, \\ \Omega_k^1 &:= \{\mathbf{x} \in \Omega \mid \operatorname{dist}(\mathbf{x}, \Gamma_k) \in (h_k, \sqrt{h_k}]\}, \\ \Omega_k^0 &:= \{\mathbf{x} \in \Omega \mid \operatorname{dist}(\mathbf{x}, \Gamma_k) \in (0, h_k]\}, \end{aligned}$$

where the distance function is

$$\operatorname{dist}(\mathbf{x}, \Gamma_k) = \inf_{\mathbf{y} \in \Gamma_k} |\mathbf{y} - \mathbf{x}|.$$

In this thesis, we do not find the distance from $\mathbf{x}$ to Γ_k, but rather from $\mathbf{x}$ to the discretization of Γ_k. The three regions are called the far, intermediate, and near regions respectively (Figure 3.5).

If $\mathbf{x} \in \Omega_k^2$ and N is sufficiently large, the trapezoidal rule with N points achieves high accuracy [50]. Thus, we use the approximation

$$u_k(\mathbf{x}) \approx \frac{1}{2\pi\alpha^2} \sum_{j=1}^{N} \frac{\partial}{\partial \nu_{\mathbf{y}_j}} K_0 \left(\frac{|\mathbf{y}_j - \mathbf{x}|}{\alpha} \right) \sigma_k(\mathbf{y}_j) |\Delta s_{\mathbf{y}_j}|.$$

If $\mathbf{x} \in \Omega_k^1$, we apply the trapezoidal rule with $N^{3/2}$ points

$$u_k(\mathbf{x}) \approx \frac{1}{2\pi\alpha^2} \sum_{j=1}^{N^{3/2}} \frac{\partial}{\partial \nu_{\tilde{\mathbf{y}}_j}} K_0 \left(\frac{|\tilde{\mathbf{y}}_j - \mathbf{x}|}{\alpha} \right) \sigma_k(\tilde{\mathbf{y}}_j) |\Delta s_{\tilde{\mathbf{y}}_j}|.$$

The denser sampling ensures that the approximation order is maintained [50]. To compute σ_k at $N^{3/2}$ points, we compute the Fourier series of σ_k, pad it with $N^{3/2} - N$ zeros, and compute the inverse Fourier transform.

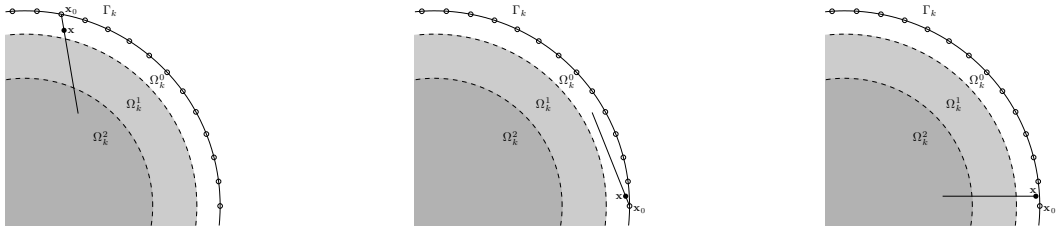

Figure 3.5: The near (white), intermediate (light grey), and far (dark grey) regions. $\mathbf{x}$ is a typical point in Ω_k^0 and $\mathbf{x}_0$ is its closest point on Γ_k. The interpolation points (3.6) are on the straight line. In the left plot, the interpolation points can be chosen in $\Omega_k^1 \cup \Omega_k^2$ since $(\mathbf{x} - \mathbf{x}_0) \cdot \nu_{\mathbf{x}_0}$ is far from 0. In the middle plot, $(\mathbf{x} - \mathbf{x}_0) \cdot \nu_{\mathbf{x}_0}$ is close to 0 resulting in interpolation points in Ω_k^0. In the right plot the interpolation points are taken in the direction $\nu_{\mathbf{x}_0}$. Then, the interpolation points are in $\Omega_k^1 \cup \Omega_k^2$. However, the interpolation becomes an extrapolation.

The problematic region is the near region Ω_k^0. As mentioned earlier, regardless of how large N is chosen, the error in the trapezoidal rule can be made arbitrarily large by choosing $\mathbf{x} \in \Omega_k^0$ sufficiently close to Γ. To avoid evaluating layer-potentials at points $\mathbf{x} \in \Omega_k^0$, an interpolant is used. We find the discretization point $\mathbf{x}_0 \in \Gamma_k$ nearest to $\mathbf{x}$, and define the

interpolation points in the direction $\mathbf{x} - \mathbf{x}_0$

$$\mathbf{z}_j = \mathbf{x}_0 + j\frac{\mathbf{x} - \mathbf{x}_0}{|\mathbf{x} - \mathbf{x}_0|}\beta h_k, \quad j = 0, \ldots, p. \tag{3.6}$$

β is chosen so that

$$\beta\frac{\mathbf{x}_0 - \mathbf{x}}{|\mathbf{x}_0 - \mathbf{x}|} \cdot \nu_{\mathbf{x}_0} > 1.$$

Then, $\mathbf{z}_0 = \mathbf{x}_0$ so that

$$\begin{aligned} u_k(\mathbf{z}_0) &= \lim_{\substack{\mathbf{x}\to\mathbf{z}_0 \\ \mathbf{x}\in\Omega}} u_k(\mathbf{x}) \\ &= \frac{1}{2\alpha^2}\sigma_k(\mathbf{x}_0) + \frac{1}{2\pi\alpha^2}\int_{\Gamma_k}\frac{\partial}{\partial\nu_{\mathbf{y}}}K_0\left(\frac{|\mathbf{y} - \mathbf{x}_0|}{\alpha}\right)\sigma_k(\mathbf{y})ds_{\mathbf{y}}. \end{aligned}$$

The jump comes from (2.31), and the integral is computed using Alpert's quadrature rules. Also, with the choice for β, the interpolation nodes $\mathbf{z}_j$ with $j \neq 0$ satisfy

$$\text{dist}(\mathbf{z}_j, \Gamma_k) > h_k.$$

Depending on the location of $\mathbf{z}_j$, we use the trapezoidal rule with either N or $N^{3/2}$ points to approximate $u_k(\mathbf{z}_j)$. Thus, if N is sufficiently large, we can approximate $u_k(\mathbf{z}_j)$ to any accuracy desired.

In the center plot of Figure 3.5, $\mathbf{x} - \mathbf{x}_0$ and $\nu_{\mathbf{x}_0}$ are close to orthogonal. The result is the interpolation points (3.6) lie in Ω_k^0. This problem is alleviated by setting a threshold on the angle between $\mathbf{x} - \mathbf{x}_0$ and $\nu_{\mathbf{x}_0}$. If the angle is too close to 0, we interpolate at the points

$$\mathbf{z}_j = \mathbf{x} - (j+1)\nu_{\mathbf{x}_0}h_k, \quad j = 0, \ldots, p,$$

which are illustrated in the right plot of Figure 3.5. Notice that in this case, $\mathbf{x}$ lies beyond all the interpolation points. Thus, we are in fact extrapolating which is an ill-conditioned problem. This can lead to larger than desired errors as is seen in the numerical examples. Possible solutions to this problem are discussed in the Interior Dirichlet example. Once we have chosen the interpolation (or extrapolation) points $\mathbf{z}_j$ and have evaluated $u_k(\mathbf{z}_j)$, a Lagrange interpolant is used to approximate $u_k(\mathbf{x})$.

In the outlined method, for each $\mathbf{x} \in \Omega$, we have to decide if it is in the far, intermediate, or near region. Done directly, the cost would be $N(M+1)$ operations for each evaluation

point in Ω. As an alternative, in [50], the authors use a Newton-type nonlinear iteration to maximize

$$\frac{\mathbf{x}_0 - \mathbf{x}}{|\mathbf{x}_0 - \mathbf{x}|} \cdot \nu_{\mathbf{x}_0}.$$

They report that in most cases, it converges to a satisfactory result in 3 or 4 iterations. However, this requires a closed-form representation of Γ_k. Also, if the initial guess is poor, the method may converge to the farthest point from $\mathbf{x}$.

To resolve these issues, we find the closest point using a discrete method. Suppose $\Gamma_k \subset [-1/2, 1/2]^2$. We recursively divide $[-1/2, 1/2]^2$ into 4 equal parts $\lfloor -\log_2 \sqrt{h_k} \rfloor$ times where $\lfloor \cdot \rfloor$ is the floor function. This guarantees each undivided box will be the smallest box whose diameter is greater than $\sqrt{h_k}$. To determine if a point $\mathbf{x}$ is in Ω_k^2, we first find the undivided box containing it. Then, if its neighboring boxes contain no points of Γ_k, then $\mathbf{x} \in \Omega_k^2$. Otherwise, the distance is computed by looking at all points in neighboring boxes. Then, it is classified as either being far, intermediate, or near. This method is illustrated in Figure 3.6.

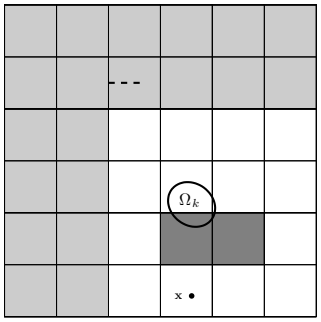

Figure 3.6: If a point lies in the light grey region it is in Ω_k^2. If it is in the white region, such as the point labeled $\mathbf{x}$, then a search is done in its neighboring boxes (dark grey region) for the closest point. Once found, the distance is computed exactly. A line of length $\sqrt{h_k}$ is drawn for comparison with the size of undivided boxes. Notice that $\sqrt{h_k}$ is smaller than the diameter of an undivided box, but if each box was refined once more, this would no longer be the case.

As a final option to sort points in each of the three regions, if Ω_k is an ellipse, the closest point can be found by solving a polynomial equation. Finding the closest point on an ellipse to a fixed point in space can be recast as the solution of a fourth-order polynomial. Since

the roots of a quartic can be determined exactly, we can bin each point immediately with no iterations.

3.4 Numerical Examples

The algorithms described in this section have been implemented in Fortran. The tolerance of GMRES is set to 10^{-11}. We demonstrate the method with four examples.

3.4.1 Interior Dirichlet

We first consider solving (2.21) with $\alpha = 0.1$ in a bounded, circular domain with 10 interior elliptic contours as depicted in Figure 3.7. We generate the Dirichlet boundary conditions from

$$u(\mathbf{x}) = \sum_{k=1}^{10} K_0 \left(\frac{|\mathbf{x} - \mathbf{x}_k|}{\alpha} \right), \tag{3.7}$$

where $\mathbf{x}_k$ is a point inside Γ_k. We compute the maximum error in the three regions

$$\Omega^0 = \bigcup_{k=0}^{10} \Omega_k^0, \quad \Omega^1 = \bigcup_{k=0}^{10} \Omega_k^1 \backslash \Omega^0, \quad \Omega^2 = \bigcup_{k=0}^{10} \Omega_k^2 \backslash (\Omega^0 \cup \Omega^1).$$

For the near region Ω^0, 15 interpolation points are used. The results are summarized in Tables 3.4–3.8.

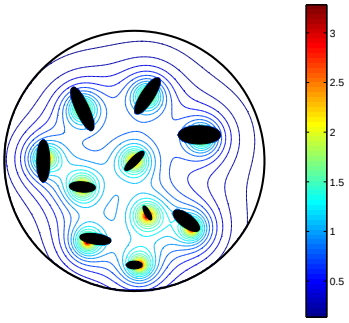

Figure 3.7: The solution of the interior Dirichlet 10-ply domain problem.

We draw the following conclusions.

- The required number of GMRES steps is independent of N, as predicted, but is also independent of the quadrature rule.

- For smaller values of N, the accuracy in Ω^1 and Ω^0 is poor. This is most likely the result of a significant error in the density function. Since the density function is multiplied by a kernel which takes on its smallest values in Ω^2, this error is not as prevalent in Ω^2.

- The error in Ω^0 is at times larger than the error in $\Omega^1 \cup \Omega^2$. This indicates an interpolation error. A first attempt to reduce the error would be to use Chebyshev interpolation points. However, these points cluster near the end points and it would be difficult to guarantee that they remain outside of Ω_k^0. Another attempt would be to use different interpolating functions. Due to the nature of the problems being solved, perhaps the interpolating functions

$$K_n\left(\frac{|\mathbf{x}-\mathbf{x}_k|}{\alpha}\right), \quad n \geq 0,$$

  where $\mathbf{x}_k$ are points chosen inside Ω_k would reduce the interpolation error.

To demonstrate the need for the three different regions, Table 3.7 is recalculated with N points, rather than $N^{3/2}$, used in Ω^1. Table 3.9 indicates a significant loss of accuracy.

Total Points	GMRES Iterations	Ω^2 Error	Ω^1 Error	Ω^0 Error
704	45	8.00×10^{-6}	5.56×10^{-3}	2.84×10^{-3}
1408	45	4.19×10^{-7}	1.31×10^{-4}	1.31×10^{-4}
2816	45	5.43×10^{-8}	8.00×10^{-8}	1.06×10^{-6}
5632	45	7.22×10^{-9}	1.10×10^{-8}	9.31×10^{-8}

Table 3.4: The maximum error in the three different regions of Ω. The trapezoidal rule is used to find the density function.

3.4.2 Exterior Dirichlet

We demonstrate the versatility of the method by considering a complex unbounded domain. The domain is illustrated in Figure 3.8. The geometry is constructed by placing points in the desired locations, computing the Fourier series of this representation, and then truncating

Total Points	GMRES Iterations	Ω^2 Error	Ω^1 Error	Ω^0 Error
704	45	5.61×10^{-6}	5.53×10^{-3}	2.84×10^{-3}
1408	45	1.06×10^{-6}	1.31×10^{-4}	1.31×10^{-4}
2816	45	1.65×10^{-7}	1.13×10^{-6}	1.88×10^{-6}
5632	45	2.83×10^{-8}	2.69×10^{-7}	1.86×10^{-8}

Table 3.5: The maximum error in the three different regions of Ω. The accuracy of the quadrature rule is $\mathcal{O}(h^2 \log h)$.

Total Points	GMRES Iterations	Ω^2 Error	Ω^1 Error	Ω^0 Error
704	45	5.21×10^{-6}	5.55×10^{-3}	2.85×10^{-3}
1408	45	2.85×10^{-8}	1.31×10^{-4}	1.31×10^{-4}
2816	45	1.50×10^{-10}	3.52×10^{-7}	1.01×10^{-6}
5632	45	5.16×10^{-12}	4.34×10^{-11}	7.84×10^{-11}

Table 3.6: The maximum error in the three different regions of Ω. The accuracy of the quadrature rule is $\mathcal{O}(h^4 \log h)$.

Total Points	GMRES Iterations	Ω^2 Error	Ω^1 Error	Ω^0 Error
704	45	5.21×10^{-6}	5.55×10^{-3}	2.85×10^{-3}
1408	45	2.85×10^{-8}	1.32×10^{-4}	1.32×10^{-4}
2816	45	1.44×10^{-10}	3.76×10^{-9}	1.01×10^{-6}
5632	45	1.98×10^{-11}	1.29×10^{-10}	1.38×10^{-10}

Table 3.7: The maximum error in the three different regions of Ω. The accuracy of the quadrature rule is $\mathcal{O}(h^8 \log h)$.

Total Points	GMRES Iterations	Ω^2 Error	Ω^1 Error	Ω^0 Error
704	45	5.21×10^{-6}	5.55×10^{-3}	2.85×10^{-3}
1408	45	2.85×10^{-8}	1.31×10^{-4}	1.31×10^{-4}
2816	45	1.26×10^{-10}	3.86×10^{-9}	1.01×10^{-6}
5632	45	1.39×10^{-10}	9.96×10^{-10}	9.30×10^{-10}

Table 3.8: The maximum error in the three different regions of Ω. The accuracy of the quadrature rule is $\mathcal{O}(h^{16} \log h)$.

Total Points	GMRES Iterations	Ω^2 Error	Ω^1 Error	Ω^0 Error
704	45	5.21×10^{-6}	2.75×10^{-1}	4.56×10^{-1}
1408	45	2.85×10^{-8}	4.32×10^{-2}	2.94×10^{-1}
2816	45	1.44×10^{-10}	5.14×10^{-3}	1.21×10^{-1}
5632	45	1.98×10^{-11}	9.38×10^{-4}	1.16×10^{-1}

Table 3.9: The maximum error in the three different regions of Ω. Only N points were used in Ω^1. The accuracy of the quadrature rule is $\mathcal{O}(h^8 \log h)$.

the Fourier series. In this example, modes above 100 are set to zero. There are 1812 points on the truck and 2928 points on the man for a total of 4740 points.

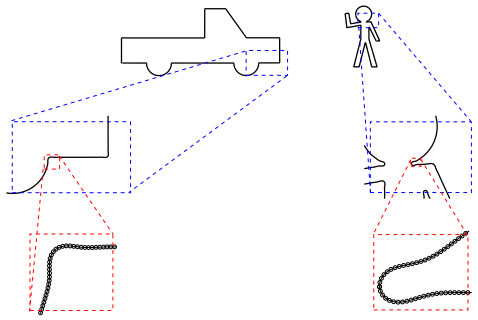

Figure 3.8: The exterior domain consisting of a truck and a man. The blue boxes are magnified in the middle plots, and the red boxes are magnified in the bottom plots.

The modified Helmholtz equation is solved with $\alpha = 1$. The boundary conditions are $u = 1$ on the truck and $u = -1$ on the man. A total of 44 GMRES steps were required to achieve the desired accuracy. The near-singular integration strategy is not used because of fine details that are difficult to resolve such as in the neck of the man. This results in some sporadic errors near the boundaries. Thus, we threshold the solution by imposing $u(\mathbf{x}) = 1$ if $\mathbf{x}$ is in the near region of the truck and $u(\mathbf{x}) = -1$ if $\mathbf{x}$ is in the near region of the man. Surface and contour plots are in Figure 3.9.

3.4.3 Exterior Neumann

We consider an exterior Neumann problem whose boundary conditions are derived from (3.7). The geometry is the same as Figure 3.7 minus the outer boundary. Based on results from

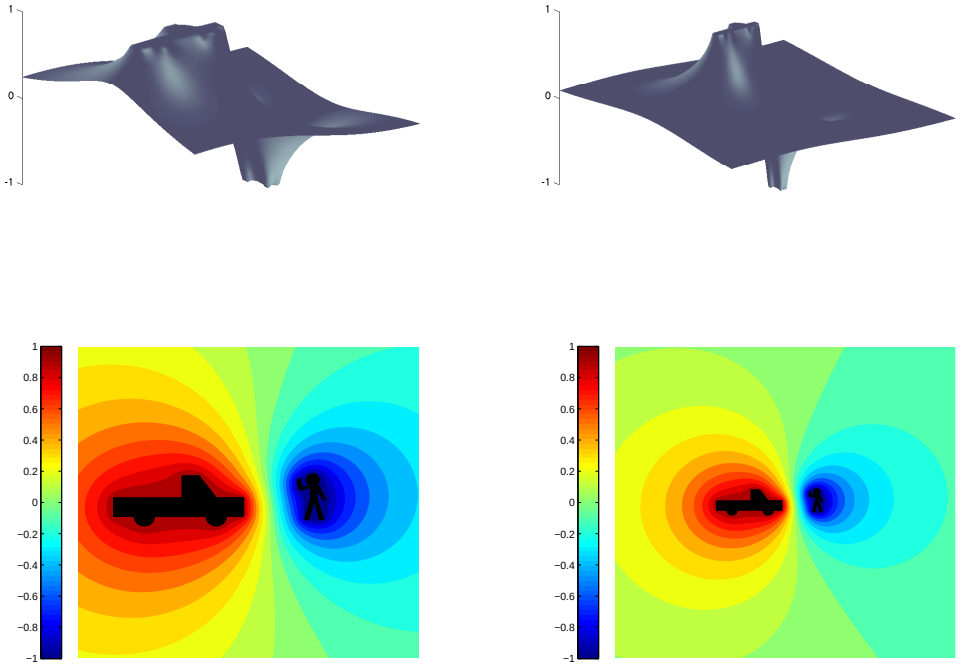

Figure 3.9: The solution of the modified Helmholtz equation in an exterior domain. The left plots have domain $[-1/2, 1/2]^2$ and the right plots have domain $[-1, 1]^2$. The right plots show that the solution is decaying to zero.

Tables 3.4–3.8, we select the $\mathcal{O}(h^8 \log h)$ quadrature rule, and we examine the performance of the method for different values of the parameter α.

Total Points	GMRES Iterations	Ω^2 Error	Ω^1 Error	Ω^0 Error
640	23	1.10×10^{-4}	1.73×10^{-4}	1.85×10^{-2}
1280	23	1.47×10^{-9}	2.31×10^{-8}	1.32×10^{-3}
2560	23	1.56×10^{-11}	2.04×10^{-11}	3.15×10^{-6}
5120	23	2.08×10^{-11}	2.55×10^{-11}	3.91×10^{-10}

Table 3.10: The maximum error in the three different regions of Ω with $\alpha = 10$.

Total Points	GMRES Iterations	Ω^2 Error	Ω^1 Error	Ω^0 Error
640	23	6.18×10^{-5}	1.24×10^{-4}	1.85×10^{-2}
1280	23	9.37×10^{-10}	2.37×10^{-8}	1.32×10^{-3}
2560	23	1.46×10^{-11}	2.07×10^{-11}	3.15×10^{-6}
5120	23	1.69×10^{-11}	2.12×10^{-11}	3.97×10^{-10}

Table 3.11: The maximum error in the three different regions of Ω with $\alpha = 1$.

Total Points	GMRES Iterations	Ω^2 Error	Ω^1 Error	Ω^0 Error
640	25	1.62×10^{-5}	7.55×10^{-5}	1.85×10^{-2}
1280	25	3.43×10^{-10}	2.43×10^{-8}	1.32×10^{-3}
2560	25	1.90×10^{-11}	2.20×10^{-11}	3.15×10^{-6}
5120	25	1.48×10^{-11}	2.32×10^{-11}	4.07×10^{-10}

Table 3.12: The maximum error in the three different regions of Ω with $\alpha = 0.1$.

For the near region Ω^0, 10 interpolation points are used. The results are summarized in Tables 3.10–3.13. We see similar behavior as observed in the interior Dirichlet example. In addition, the number of required GMRES steps appears relatively independent of α for $\alpha \geq 0.1$. This behavior is partially explained by the following argument. As α increases, the equation we are solving approaches Laplace's equation. We know that the boundary integral equation for the exterior Neumann Laplace's equation has a unique solution [18, 24]. Thus, we should expect the integral equation for the exterior Neumann modified Helmholtz equation to remain well-conditioned as α increases. This in turn bounds the number of

Total Points	GMRES Iterations	Ω^2 Error	Ω^1 Error	Ω^0 Error
640	15	7.23×10^{-9}	1.51×10^{-5}	2.18×10^{-2}
1280	15	1.25×10^{-12}	2.40×10^{-8}	1.46×10^{-3}
2560	15	3.66×10^{-14}	2.17×10^{-12}	3.41×10^{-6}
5120	15	1.38×10^{-13}	2.18×10^{-12}	4.23×10^{-10}

Table 3.13: The maximum error in the three different regions of Ω with $\alpha = 0.01$.

required GMRES steps. However, the boundary integral equation for Laplace's equation with Dirichlet boundary conditions has non-trivial solutions. Therefore, we expect the number of GMRES steps to increase for larger values of α. We expect the same behavior for the bounded Neumann problem.

3.4.4 A Larger-Scale Problem

We now consider a more complex bounded domain with 100 elliptic contours of varying size and alignment, and $\alpha = 0.1$. On each contour, we prescribe a constant Dirichlet boundary condition selected randomly from $(-1, 1)$. Each contour is discretized with 512 points, resulting in a linear system with 51,712 unknowns. A contour plot and surface plot are in Figure 3.10. If an integral equation method were not used, the modified Helmholtz equation would be difficult or impossible to solve in this geometry with such high accuracy.

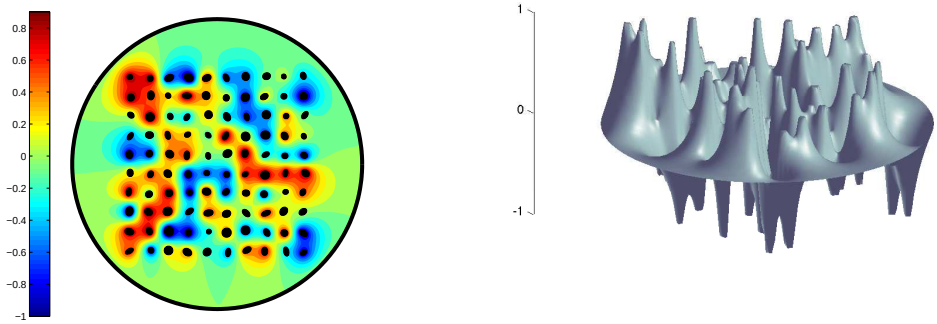

Figure 3.10: The solution to the modified Helmholtz equation with $\alpha = 0.1$. The quadrature rule has accuracy $\mathcal{O}(h^8 \log h)$. On each Γ_k, a constant boundary condition is chosen at random in $(-1, 1)$. GMRES required 89 iterations to achieve 11 digits accuracy.

Chapter 4

The Forced Problem

Our strategy for solving (2.6) and (2.7) requires a solution of the forced problem (2.20), which we rewrite here,

$$(1 - \alpha^2 \Delta) u^P = g, \quad \mathbf{x} \in \Omega. \tag{4.1}$$

Boundary conditions are not specified, so solutions are not unique. In this chapter, we use volume potentials to form a solution of (4.1).

Anita Mayo [41] has developed methods for efficiently evaluating volume potentials for the Laplace and biharmonic equations. These approaches are based on a finite difference method with locally corrected stencils to account for jumps across interfaces. The methods in [41] are second-order, but have been extended to fourth-order in [43, 42]. However, we avoid using stencil-based methods as they often have stability issues [10]. Alternatively, an unstructured mesh could be used to calculate the volume potential. However, we wish to avoid the difficulties with mesh generation. Instead, we compute the volume potential with an adaptive quadtree structure.

Section 4.1 discusses methods developed in [17] for computing a volume integral that solves (4.1). We also discuss strategies for evaluating this volume integral on Γ so that the correct boundary conditions in (2.21) are formed. The volume integral requires values for the forcing term in the unit box, thus, the forcing term must be extended from Ω to a box containing Ω. Three possible methods are compared in Section 4.2. In Section 4.3, several numerical examples show the advantages and limitations of each extension.

4.1 Volume Integral

From Theorem 2.2, a solution of (4.1) is

$$u^P(\mathbf{x}) = \frac{1}{2\pi\alpha^2}\int_\Omega K_0\left(\frac{|\mathbf{y}-\mathbf{x}|}{\alpha}\right) g(\mathbf{y})d\mathbf{y}, \quad \mathbf{x}\in\Omega. \tag{4.2}$$

In [17], Cheng et. al. present a fourth-order method to compute (4.2) when Ω is the unit square $D = [-1/2, 1/2]^2$. We extend this work to more general domains Ω by coupling the volume integral solver in [17] with the homogeneous solver in [37]. This work can also be extended to higher order methods. In [20], the authors develop an eighth-order method for Poisson's equation.

Suppose Ω is a bounded domain. We assume that $\Omega \subset D$ which can always be achieved by manipulating α. Given a forcing term $g : \Omega \to \mathbb{R}$, we construct an extension $\tilde{g} : D \to \mathbb{R}$. That is, $\tilde{g}$ satisfies $\tilde{g}(\mathbf{x}) = g(\mathbf{x})$ for all $\mathbf{x} \in \Omega$. Define $\widetilde{u^P} : D \to \mathbb{R}$,

$$\widetilde{u^P}(\mathbf{x}) = \frac{1}{2\pi\alpha^2}\int_D K_0\left(\frac{|\mathbf{y}-\mathbf{x}|}{\alpha}\right) \tilde{g}(\mathbf{y})d\mathbf{y}, \quad \mathbf{x}\in D. \tag{4.3}$$

Then, $(1-\alpha^2\Delta)\widetilde{u^P}(\mathbf{x}) = \tilde{g}(\mathbf{x})$ for all $\mathbf{x} \in D$; in particular, $(1-\alpha^2\Delta)\widetilde{u^P}(\mathbf{x}) = g(\mathbf{x})$ for all $\mathbf{x} \in \Omega$. Hence, a solution of (4.1) is

$$u^P(\mathbf{x}) = \widetilde{u^P}(\mathbf{x}), \quad \mathbf{x}\in\Omega,$$

the restriction of $\widetilde{u^P}$ to Ω. In the next section, we discuss possible methods to construct $\tilde{g}$. First, we outline the method described in [17].

An adaptive quadtree structure is used to superimpose a hierarchy of refinement on the computational domain D. The unit square D is considered to be grid level 0. Grid level $l+1$ is obtained recursively by subdividing each square (or node) s at level l into four equal parts; these are called the children of s. Adaptivity is achieved by allowing different levels of refinement throughout the tree. Precomputation is possible if a standard restriction is placed on the quadtree: two nodes that share a boundary point must be no more than one refinement level apart. We denote the childless nodes in the quadtree as D_i, $i = 1, \ldots, P$, where P is the total number of such nodes.

In each box s, an interpolant for $\tilde{g}$ is constructed. The interpolant belongs to

$$span\{1, x, y, x^2, xy, y^2, x^3, x^2y, xy^2, y^3\},$$

and is the best approximation in the least-squares sense on a cell-centered 4×4 grid in s. Then, $\tilde{g}$ and the interpolant are evaluated on a cell-centered 8×8 grid in s. If the l^2 error is larger than some preset tolerance τ, then s is subdivided.

For each childless box D_i, we write the polynomial interpolant as

$$\tilde{g}(\mathbf{x}) \approx \sum_{j=1}^{10} c_j^i p_j(\mathbf{x} - \mathbf{x}^i), \quad \mathbf{x} \in D_i,$$

where $\mathbf{x}^i$ is the center of D_i. An approximation of (4.3) is

$$\begin{aligned}
\widetilde{u^P}(\mathbf{x}) &= \sum_{i=1}^{P} \frac{1}{2\pi\alpha^2} \int_{D_i} K_0\left(\frac{|\mathbf{y}-\mathbf{x}|}{\alpha}\right) \tilde{g}(\mathbf{y}) d\mathbf{y} \\
&\approx \sum_{i=1}^{P} \frac{1}{2\pi\alpha^2} \int_{D_i} K_0\left(\frac{|\mathbf{y}-\mathbf{x}|}{\alpha}\right) \sum_{j=1}^{10} c_j^i p_j(\mathbf{y} - \mathbf{x}^i) d\mathbf{y} \\
&= \sum_{i=1}^{P} \frac{1}{2\pi\alpha^2} \sum_{j=1}^{10} c_j^i \int_{D_i} K_0\left(\frac{|\mathbf{y}-\mathbf{x}|}{\alpha}\right) p_j(\mathbf{y} - \mathbf{x}^i) d\mathbf{y}, \quad \mathbf{x} \in D. \qquad (4.4)
\end{aligned}$$

To evaluate (4.4) at all $N_D = 16 \times P$ points directly requires $\mathcal{O}(N_D^2)$ operations. This is reduced to $\mathcal{O}(N_D)$ operations using the fast multiople method (FMM) [17].

Once (4.4) has been computed at all N_D points, we interpolate onto Γ to formulate the correct boundary condition f in (2.21b) or (2.22b). To avoid computing derivatives of u^P, we focus on the Dirichlet problem (2.6). Since we have computed $\widetilde{u^P}$ on the cell-centered 4×4 grid of each D_i, we use the third-order polynomials that we have already introduced to construct an interpolant. Let $\mathbf{x}_0 \in \Gamma$ and let D_i be the childless box with $\mathbf{x}_0 \in D_i$. Given the 16 values of u^P in box D_i, we construct the polynomial approximation

$$u^P(\mathbf{x}) \approx \sum_{j=1}^{10} d_j^i p_j(\mathbf{x} - \mathbf{x}^i), \quad \mathbf{x} \in D_i,$$

and then evaluate

$$u^P(\mathbf{x}_0) \approx \sum_{j=1}^{10} d_j^i p_j(\mathbf{x}_0 - \mathbf{x}^i).$$

Alternatively, we could use (4.4) and evaluate

$$u^P(\mathbf{x}_0) \approx \sum_{i=1}^{P} \frac{1}{2\pi\alpha^2} \sum_{j=1}^{10} c_j^i \int_{D_i} K_0\left(\frac{|\mathbf{y}-\mathbf{x}_0|}{\alpha}\right) p_j(\mathbf{y} - \mathbf{x}^i) d\mathbf{y}.$$

This would require manipulating the FMM used to evaluate (4.4) at the N_D cell-centered points. However, if solving a Neumann problem, the normal derivative should be approximated with

$$\frac{\partial}{\partial \nu_{\mathbf{x}_0}} u^P(\mathbf{x}_0) \approx \sum_{i=1}^{P} \frac{1}{2\pi\alpha^2} \sum_{j=1}^{10} c_j^i \int_{D_i} \frac{\partial}{\partial \nu_{\mathbf{x}_0}} K_0\left(\frac{|\mathbf{y}-\mathbf{x}_0|}{\alpha}\right) p_j(\mathbf{y}-\mathbf{x}^i) d\mathbf{y}.$$

This approach is not adopted in [17]; rather, they used finite differences.

4.2 Constructing Extensions

There are several options for extending g to D. We outline three of them. The first extension is the most naive

$$\tilde{g}(\mathbf{x}) = \begin{cases} g(\mathbf{x}), & \mathbf{x} \in \Omega, \\ 0, & \mathbf{x} \in D \backslash \Omega. \end{cases}$$

Since $\tilde{g}$ is only piecewise continuous, we expect $\widetilde{u^P}$ to be continuously differentiable. Thus, when we interpolate $\widetilde{u^P}$, the order of the method is reduced to two. Also, since a box is refined if it can not be approximated well by a third-order polynomial, the quadtree will excessively refine near Γ and consequently will slow down the evaluation. For example, in [20], $\Delta u = \tilde{g}$ was solved with $\tilde{g} = 1$ inside the unit disk and $\tilde{g} = 0$ outside. The total number of childless boxes was $\mathcal{O}(10^5)$ which is far too large for this simple function $\tilde{g}$.

In [36], the authors consider the class of problems where the forcing term g on each Γ_k is constant. Let Ω_k, $k = 1, \ldots, M$ be the region bounded by Γ_k, and $\Omega_0 = D \backslash \Omega_1 \cup \cdots \cup \Omega_M$. The second extension is

$$\tilde{g}(\mathbf{x}) = \begin{cases} g(\mathbf{x}), & \mathbf{x} \in \Omega, \\ C_k, & \mathbf{x} \in \Omega_k, \\ C_0, & \mathbf{x} \in \Omega_0, \end{cases}$$

where $g(\mathbf{x}) = C_k$ for $\mathbf{x} \in \Gamma_k$. The disadvantage of this method is the restriction on g. However, with this restriction, the authors demonstrate that using integral equations and Rothe's method to solve (1.1) is promising. Since $\tilde{g}$ is continuous, this extension results in a third-order accurate solution. There will also be refinement near Γ because of the discontinuity in the derivative of $\tilde{g}$. However, the refinement will not be as excessive as in the first extension.

As a final option to extend g, we focus on reducing excessive refinement of the quadtree near Γ and make no attempt to construct a smooth function $\tilde{g}$. When constructing the quadtree, a box s is either entirely inside Ω, entirely outside Ω, or intersects Ω and Ω^c. We start by defining

$$\tilde{g}(\mathbf{x}) = \begin{cases} g(\mathbf{x}), & \mathbf{x} \in \Omega, \\ 0, & \mathbf{x} \in D_i \text{ with } D_i \cap \Omega = \emptyset. \end{cases}$$

Now consider a box s whose 16 points $\{\mathbf{x}_j\}_{j=1}^{16}$ lie on both sides of Γ. For each of these points, we define its neighbors to be the set of points inside s to the north, south, east, and west, as well as northeast, northwest, southeast, and southwest. A point has at most eight neighbors. Let $\Lambda \subset \{1, \ldots, 16\}$ be the indices of points where $\tilde{g}$ is undefined. For each $j \in \Lambda$, we count the total number of neighbors of $\mathbf{x}_j$ where $\tilde{g}$ is defined. Beginning with the point which has the most known neighbor values, we take an average of the values and assign it to $\tilde{g}(\mathbf{x}_j)$. We repeat this process until $\tilde{g}$ is known at all 16 points inside s. To assign more weight to closer points, we use the inverse distance weighted average

$$\tilde{g}(\mathbf{x}_j) = \sum_{k \in \Lambda} w_k \tilde{g}(\mathbf{x}_k),$$

where

$$w_k = \frac{h_k^{-2}}{\sum_{i \in \Lambda} h_i^{-2}},$$

and $h_k = 1$ if $\mathbf{x}_k$ is to the north, south, east or west of $\mathbf{x}_j$, and $h_j = \sqrt{2}$ if $\mathbf{x}_k$ is to the northeast, northwest, southeast, or southwest of $\mathbf{x}_j$. This procedure is illustrated in Figure 4.1.

Once $\tilde{g}$ has values assigned at all 16 points, a fourth-order polynomial is fit in the least-squares sense to these function values. Then, the error is checked at the intersection of the cell-centered 8×8 grid and Ω. If the error is above the threshold τ, s is subdivided.

We compare these three options for $\tilde{g}$ by computing the size of the quadtree required to achieve a desired accuracy. The domain Ω is the ball centered at the origin of radius 0.5 and the forcing term is

$$g(\mathbf{x}) = e^{-|\mathbf{x}|^2}, \quad |\mathbf{x}| \leq 0.5.$$

The three options are:

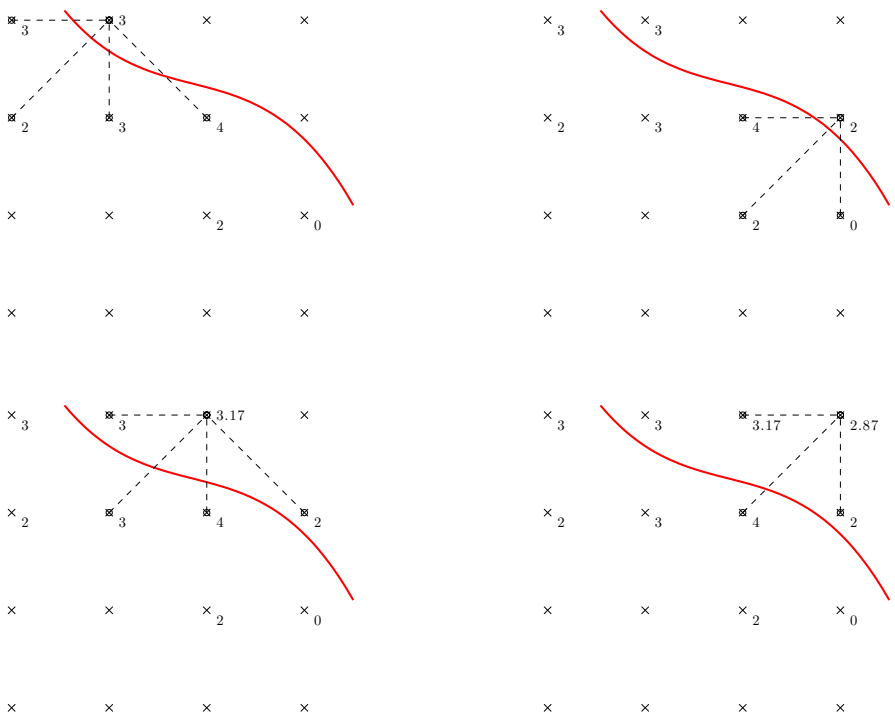

Figure 4.1: The cell-centered 4×4 grid points and the value of $\tilde{g}$ at some of the grid points. The points to the right of the red line are unknown at the initial state. Reading left to right then top to bottom, values are assigned to $\tilde{g}$ at the unknown values.

- Option 1:

$$\tilde{g}(\mathbf{x}) = \begin{cases} g(\mathbf{x}), & \mathbf{x} \in \Omega, \\ 0, & \mathbf{x} \notin \Omega. \end{cases}$$

- Option 2:

$$\tilde{g}(\mathbf{x}) = \begin{cases} g(\mathbf{x}), & \mathbf{x} \in \Omega, \\ e^{-0.5^2}, & \mathbf{x} \notin \Omega. \end{cases}$$

- Option 3

$$\tilde{g}(\mathbf{x}) = \begin{cases} g(\mathbf{x}), & \mathbf{x} \in \Omega, \\ 0, & \mathbf{x} \in D_i \text{ with } D_i \cap \Omega = \emptyset, \end{cases}$$

  otherwise, $\tilde{g}(\mathbf{x})$ is defined using the averaging strategy.

Table 4.1 lists the size of the quadtree required to achieve the desired accuracy τ (prerefine), and the size of the quadtree after the restriction on neighboring boxes (postrefine).

	Option 1		Option 2		Option 3	
τ	Prerefine	Postrefine	Prerefine	Postrefine	Prerefine	Postrefine
10^{-1}	21	21	1	1	5	5
10^{-2}	149	165	5	5	21	21
10^{-3}	405	645	37	37	69	69
10^{-4}	1,189	2,085	117	133	149	165
10^{-5}	4,053	8,101	277	357	309	389
10^{-6}	11,253	24,485	581	901	741	1,157
10^{-7}	36,021	76,517	1,461	2,197	2,149	3,973
10^{-8}	—	—	2,885	4,709	4,389	8,773

Table 4.1: The total number of boxes in the quadtrees for each option of $\tilde{g}$. Option 1 is piecewise continuous with the discontinuity on Γ; option 2 is continuous, but not differentiable, with the loss of differentiability on Γ; option 3 is piecewise continuous, but has some regularity on each childless box D_i.

Figure 4.2 illustrates the quadtree both before and after the tree has the additional restriction concerning neighboring boxes. Also illustrated is the extension $\tilde{g}$. As expected, option 1 refines near Γ and $\tilde{g}$ is only piecewise continuous. Using option 2, $\tilde{g}$ is continuous and the tree is refined less along Γ. For the third option, $\tilde{g}$ is piecewise continuous in D, but

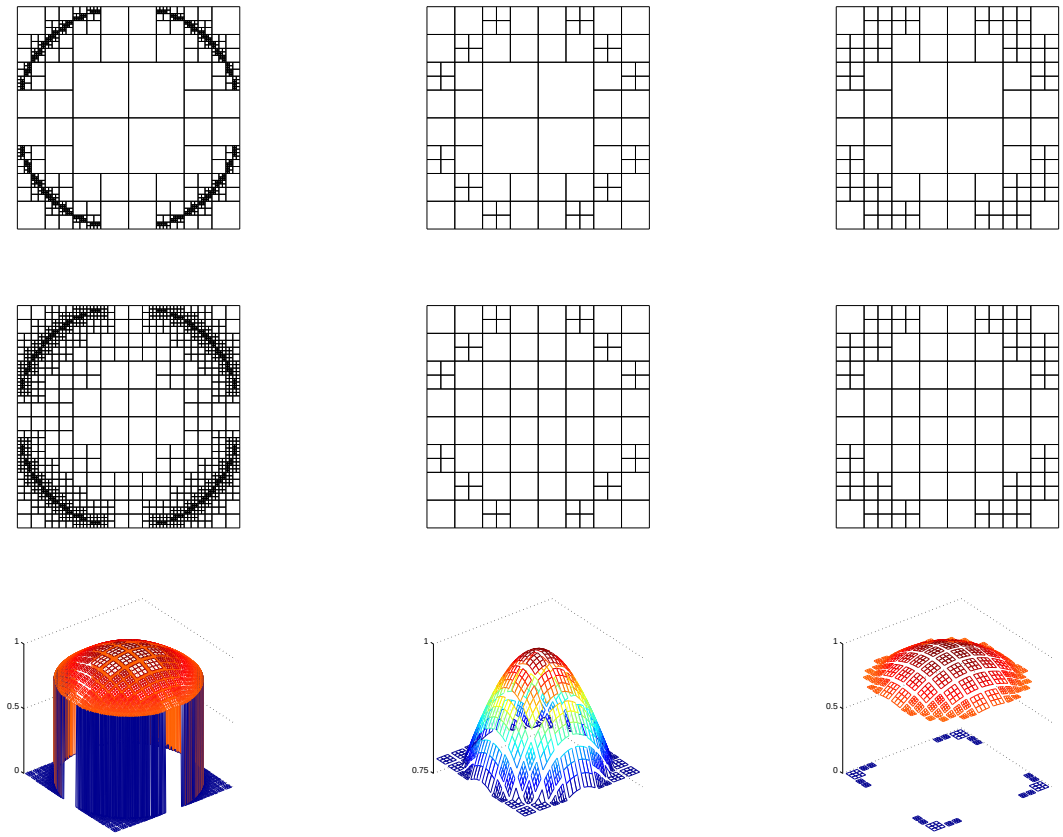

Figure 4.2: From left to right are option 1, option 2, and option 3. From top to bottom are the quadtrees before refinement, after refinement, and a plot of the $\tilde{g}$. Boxes are subdivided if the error is greater than $\tau = 10^{-4}$.

has some regularity in each childless box D_i. The result is a quadtree that is comparable to option 2.

We redo the previous example with the forcing term $g(x, y) = x$. Since g is not constant on Γ, option 2 is omitted. The results are summarized in Table 4.2 and illustrated in Figure 4.3. Again, option 3 results in a significant reduction of the size of the quadtree.

	Option 1		Option 3	
τ	Prerefine	Postrefine	Prerefine	Postrefine
10^{-1}	21	21	5	5
10^{-2}	85	85	21	21
10^{-3}	245	325	69	69
10^{-4}	885	1,525	149	165
10^{-5}	2,373	4,565	293	389
10^{-6}	7,349	15,221	801	1,405
10^{-7}	22,613	48,993	1,737	3,625
10^{-8}	—	—	3,279	7,965

Table 4.2: The total number of boxes in the quadtrees for two options of $\tilde{g}$. Option 1 is piecewise continuous with the discontinuity on Γ; option 3 is piecewise continuous, but has some regularity on each childless box D_i.

To develop methods that are higher-order, we require additional conditions on $\tilde{g}$. Ideally, we want $\tilde{g}$ to satisfy three properties:

1. $\tilde{g}(\mathbf{x}) = g(\mathbf{x})$ for all $\mathbf{x} \in \Omega$.
2. $\tilde{g} \in C^{\infty}(D)$.
3. The support of $\tilde{g}$ is contained in D.

The second property can be relaxed since we are using a fourth-order method, but smoother $\tilde{g}$ allows for higher-order methods to compute (4.2). The third property guarantees that $\tilde{g}$ is smooth in $\mathbb{R}^2$. This would eliminate a loss of accuracy near the boundary of D. The future goal is to use mollifiers or partitions of unity to guarantee properties 2 and 3.

4.3 Numerical Examples

We test the methods described in this chapter on a variety of problems. We start by solving a forced modified Helmholtz equation, then the heat equation both with and without a

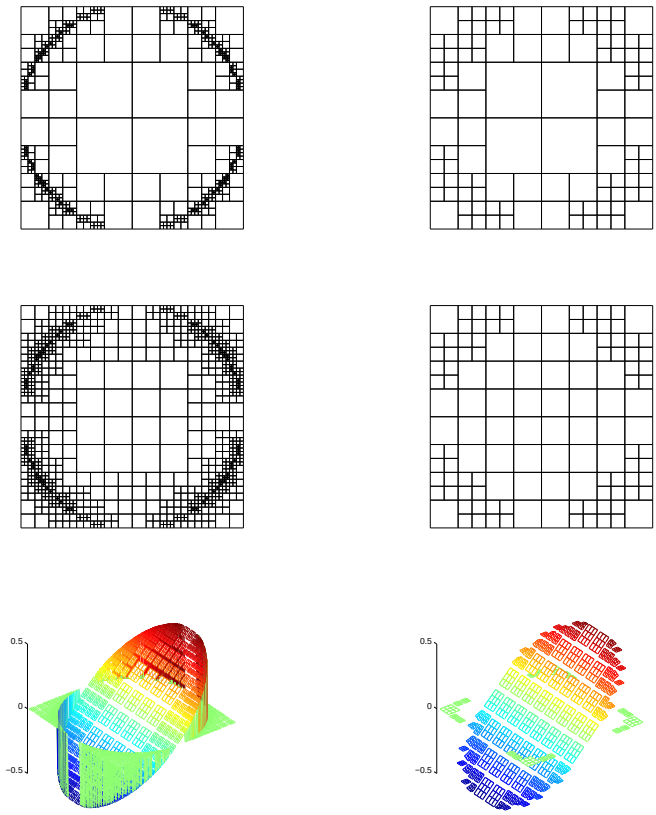

Figure 4.3: From left to right are option 1 and option 3. From top to bottom are the quadtree before refinement, after refinement, and a plot of the $\tilde{g}$. Boxes are subdivided if the error is greater than $\tau = 10^{-4}$.

forcing term, and conclude with the nonlinear Allen-Cahn equation. The GMRES tolerance for the forced problem is set to 10^{-11}.

4.3.1 A Forced Problem

We solve the forced modified Helmholtz equation

$$u(\mathbf{x}) - \alpha^2 \Delta u(\mathbf{x}) = g(\mathbf{x}), \quad \mathbf{x} \in \Omega,$$
$$u(\mathbf{x}) = f(\mathbf{x}), \quad \mathbf{x} \in \Gamma,$$

where $g(\mathbf{x}) = |\mathbf{x}|^4 - 16\alpha^2|\mathbf{x}|^2$, and $f(\mathbf{x}) = |\mathbf{x}|^4$. The exact solution is $u(\mathbf{x}) = |\mathbf{x}|^4$. The domain Ω is the annulus $B(0, 0.4)\backslash B(0, 0.1)$, and we choose $\alpha = 1$. We use $N = 2^8$ points on both Γ_0 and Γ_1 and $N = 2^{12}$ points are used in the intermediate region Ω^1. The tolerance for constructing the quadtree is set to $\tau = 10^{-12}$. With this small value of τ, we expect the quadtree to refine to the maximum allowable level except in regions where $\tilde{g}$ is constant.

Since g is constant on Γ_0 and Γ_1, we take the continuous extension defined by option 2. The results are summarized in Table 4.3 As expected, we see fourth-order accuracy in

Max Level	Quadtree Size	Ω^2 Error	Ω^1 Error	Ω^0 Error
2	21	7.76×10^{-4}	4.00×10^{-4}	1.23×10^{-4}
3	85	3.73×10^{-5}	1.36×10^{-4}	1.39×10^{-5}
4	341	1.84×10^{-6}	2.01×10^{-5}	2.00×10^{-6}
5	917	1.74×10^{-7}	5.86×10^{-7}	4.12×10^{-7}
6	3,125	8.40×10^{-9}	3.28×10^{-8}	9.09×10^{-8}
7	11,781	1.31×10^{-9}	2.99×10^{-9}	1.17×10^{-8}

Table 4.3: The maximum level of the quadtree and the size of the quadtree for a forced modified Helmholtz equation. The maximum errors in the far, intermediate, and near regions are listed. Option 2 is used to construct $\tilde{g}$.

Ω^2. However, the order of convergence in Ω^1 is 3.6 and in Ω^0 is order 2.6. This is a result of the discontinuity in the derivative of the forcing term along Γ. A smoother extension $\tilde{g}$ with compact support in D would result in fourth-order accuracy throughout Ω.

We redo this example, but rather than using option 2 to construct the extension $\tilde{g}$, we use option 3. The results are summarized in Table 4.4. We do see a drop in the accuracy when comparing to Table 4.3. The order of convergence in Ω^2 is 2.0, in Ω^1 is 2.2, and in Ω^0 is 1.5. The second-order accuracy results from the loss of continuity of $\tilde{g}$ near Γ. However,

Max Level	Quadtree Size	Ω^2 Error	Ω^1 Error	Ω^0 Error
2	21	1.09×10^{-3}	4.17×10^{-4}	7.19×10^{-5}
3	85	1.11×10^{-4}	1.97×10^{-4}	1.38×10^{-4}
4	341	2.96×10^{-6}	5.76×10^{-5}	4.05×10^{-5}
5	917	1.21×10^{-4}	1.15×10^{-5}	1.45×10^{-5}
6	3,125	3.55×10^{-7}	1.66×10^{-6}	4.84×10^{-6}
7	11,781	1.38×10^{-7}	6.82×10^{-7}	2.30×10^{-6}

Table 4.4: The maximum level of the quadtree and the size of the quadtree for a forced modified Helmholtz equation. The maximum errors in the far, intermediate, and near regions are listed. Option 3 is used to construct $\tilde{g}$.

the benefit of using option 3 is clear if we set the desired tolerance to $\tau = 10^{-4}$. If we let $\tilde{g} = 0$ outside of Ω, that is, use option 1, then the required quadtree has 2517 boxes. If we use option 2, only 1077 boxes are required.

4.3.2 Forced Heat Equation

In this example, we test the temporal accuracy by solving the forced heat equation

$$u_t - \Delta u = g, \qquad \mathbf{x} \in \Omega, t > 0, \tag{4.5a}$$

$$u = f, \qquad \mathbf{x} \in \Gamma, t > 0, \tag{4.5b}$$

$$u = u_0, \qquad \mathbf{x} \in \Omega, t = 0, \tag{4.5c}$$

where $\Omega = B(0, 0.4) \backslash B(0, 0.1)$. The forcing term is

$$g(\mathbf{x}) = -400 \cos(20|\mathbf{x}|) - 20 \frac{\sin(20|\mathbf{x}|)}{|\mathbf{x}|}.$$

The exact solution is

$$u(\mathbf{x}, t) = e^{-\lambda^2 t}[Y_0(0.1\lambda)J_0(\lambda|\mathbf{x}|) - J_0(0.1\lambda)Y_0(\lambda|\mathbf{x}|)] + \cos(20|\mathbf{x}|),$$

where J_0 is the zeroth-order Bessel function of the first kind, and Y_0 is the zeroth-order Bessel function of the second kind. We choose $\lambda \approx 10.244$ which makes the time-dependent term vanish on Γ. Then, the boundary conditions are

$$f(\mathbf{x}) = \begin{cases} \cos(8), & \mathbf{x} \in \Gamma_0, \\ \cos(2), & \mathbf{x} \in \Gamma_1. \end{cases}$$

Since the boundary conditions are constant on Γ_0 and Γ_1, we use the continuous extension of g defined earlier as option 2. This helps reduce the spatial error so that the temporal discretization is the dominating source of error.

We calculate solutions to (4.5) using the first-order IMEX Euler and extrapolated Gear methods up to $t = 0.01$. The tolerance for the volume integral is $\tau = 10^{-10}$ and $N = 1024$ points are used on both Γ_0 and Γ_1. This spatial resolution is high enough that the spatial error is negligible in comparison to the temporal error. The maximum error is evaluated at points that are sufficiently far away from Γ. The results are summarized in Table 4.5. We

Δt	Error_1	Error_2
2.0×10^{-3}	1.37×10^{-2}	1.66×10^{-3}
1.0×10^{-3}	7.14×10^{-3}	4.77×10^{-4}
5.0×10^{-4}	3.66×10^{-3}	1.25×10^{-4}
2.5×10^{-4}	1.89×10^{-3}	3.22×10^{-5}

Table 4.5: Temporal Error using IMEX Euler (Error_1) and Extrapolated Gear (Error_2); we achieve first and second order convergence, respectively. The solution at time step dt for extrapolated Gear was taken to be the exact solution. This eliminates introducing error caused by initially using a low-order method.

see that we achieve first-order convergence for IMEX Euler and nearly achieve second-order for extrapolated Gear. The slight reduction in order is due to error near Γ that is propagated into Ω with each time step. This problem would be amplified if a third- or fourth-order time integrator were used. This could be resolved by implementing the near-singular integration strategy for time-dependent problems.

4.3.3 Homogeneous Heat Equation

We consider the homogeneous heat equation

$$\begin{aligned} u_t - \Delta u &= 0, \quad \mathbf{x} \in \Omega, t > 0, \\ u(\mathbf{x}, t) &= 0, \quad \mathbf{x} \in \Gamma_0, t > 0, \\ u(\mathbf{x}, t) &= 1, \quad \mathbf{x} \in \Gamma_1, t > 0, \\ u(\mathbf{x}, 0) &= 0, \quad \mathbf{x} \in \Omega. \end{aligned}$$

The geometry is an annular region (left plot of Figure 4.4). The right plot of Figure 4.4 is the solution at time $dt = 10^{-3}$. Since u is constant for all time on each of the component

curves, option 2 is used as the extension. The quadtree for the volume integral and contour plots of the solution are in Figure 4.5.

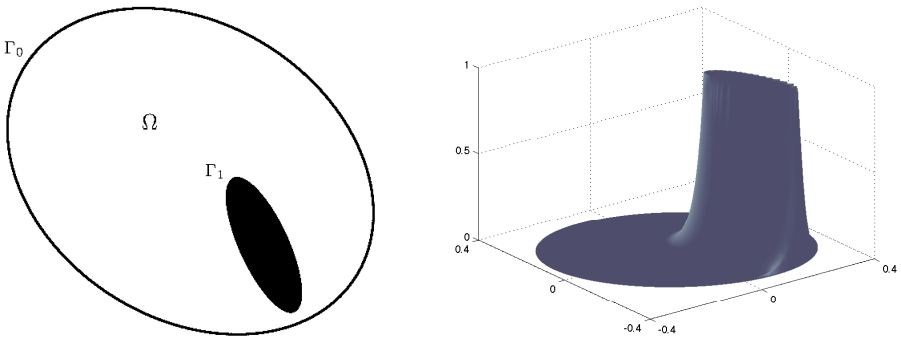

Figure 4.4: The left plot is the geometry. The right plot shows the solution at the first time step which is $t = 10^{-3}$.

4.3.4 Allen-Cahn Equation

Let $\Omega \subset \mathbb{R}^2$ be a bounded domain with a C^2 boundary. A common problem requires minimizing the energy functional

$$F(u) = \int_\Omega f(u) d\mathbf{x}.$$

Using the Euler-Lagrange equation, u must satisfy $f'(u) = 0$ for all $\mathbf{x} \in \Omega$. To solve this PDE, we can use the gradient flow

$$\frac{\partial u}{\partial t} - \epsilon \Delta u = -f'(u), \quad \mathbf{x} \in \Omega,$$

where $\epsilon > 0$. If

$$f(u) = \frac{1}{4}(1 - u^2)^2,$$

the result is the Allen-Cahn equation $u_t - \epsilon \Delta u = u(1 - u^2)$. We impose homogeneous Dirichlet boundary conditions and initialize the solution with random values uniformly distributed in $(-1, 1)$

$$\begin{aligned} &\frac{\partial u}{\partial t} - \epsilon \Delta u = u(1 - u^2), && \mathbf{x} \in \Omega, t > 0, \\ &u(\mathbf{x}, t) = 0, && \mathbf{x} \in \Gamma, t > 0, \\ &u(\mathbf{x}, 0) = u_0(\mathbf{x}), && \mathbf{x} \in \Omega. \end{aligned}$$

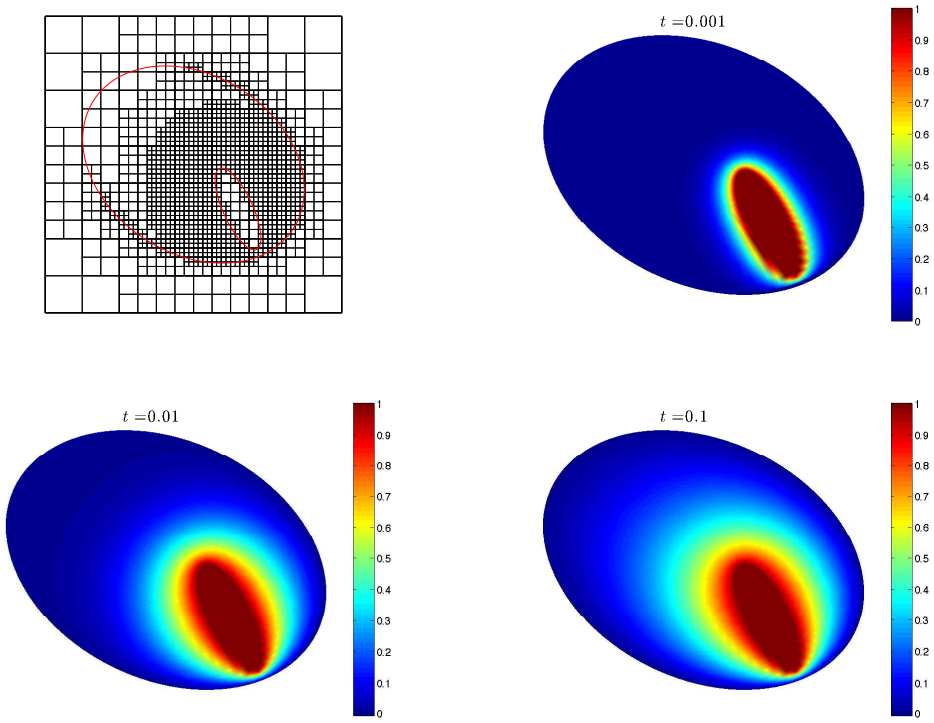

Figure 4.5: In the top left plot is the quadtree used for the volume integral. The function used to construct the quadtree is in the right plot of Figure 4.4. The other plots are solutions of the heat equation at times 10^{-3}, 10^{-2}, and 10^{-1}. The solution is near steady state at the final time.

The general behavior of solutions to the Allen-Cahn equation is well known: the stable stationary solutions are $u = 1$ and $u = -1$ and the solution exhibits coarsening towards these values. The parameter ϵ controls the width of the transition regions between the two stationary solutions. Smaller ϵ results in sharper interfaces.

We discretize in time with IMEX Euler

$$\frac{u^{N+1} - u^N}{\Delta t} - \epsilon \Delta u^{N+1} = -f'(u^N), \quad \mathbf{x} \in \Omega.$$

Rearranging,

$$(1 - \alpha^2 \Delta) u^{N+1} = u^N - \Delta t f'(u^N), \quad \mathbf{x} \in \Omega, \tag{4.6}$$

where $\alpha^2 = \epsilon \Delta t$. We march (4.6) in time with $\epsilon = 2 \times 10^{-5}$ (Figure 4.6), $\epsilon = 1 \times 10^{-5}$ (Figure 4.7), and $\epsilon = 5 \times 10^{-6}$ (Figure 4.8). Because the initial condition is random, we automatically refine the quadtree to level 6; the interpolation error is not used to determine if a box is subdivided.

We observe the expected coarsening toward the two stationary solutions. For smaller values of ϵ, the system is less diffusive and we expect more interfaces between the two stationary solutions. This qualitative behavior is captured in Figures 4.6–4.8.

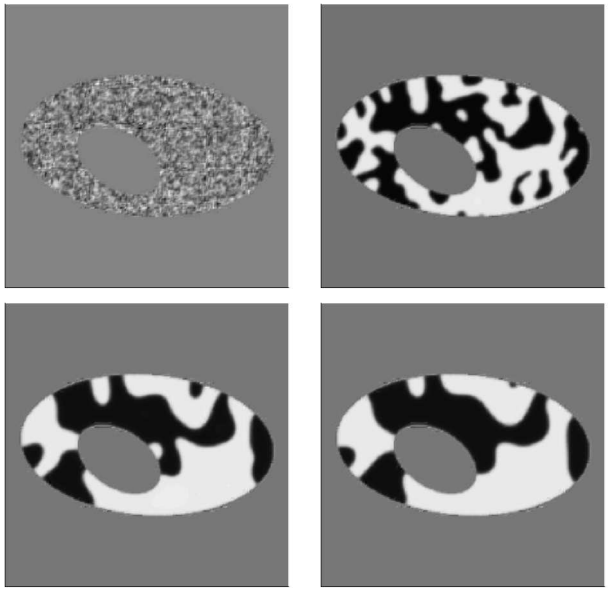

Figure 4.6: A solution of the Allen-Cahn equation with $\epsilon = 2 \times 10^{-5}$. Here, $\Delta t = 1$ and IMEX Euler's method is used. The upper left plot is the initial condition, and proceeding to the right and then down, the remaining plots are $t = 20$, $t = 60$, and $t = 100$.

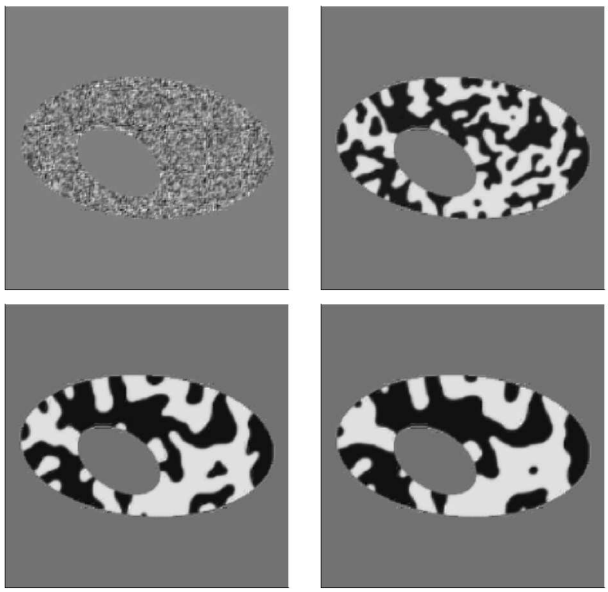

Figure 4.7: A solution of the Allen-Cahn equation with $\epsilon = 1 \times 10^{-5}$. Here, $\Delta t = 1$ and IMEX Euler's method is used. The upper left plot is the initial condition, and proceeding to the right and then down, the remaining plots are $t = 20$, $t = 60$, and $t = 100$.

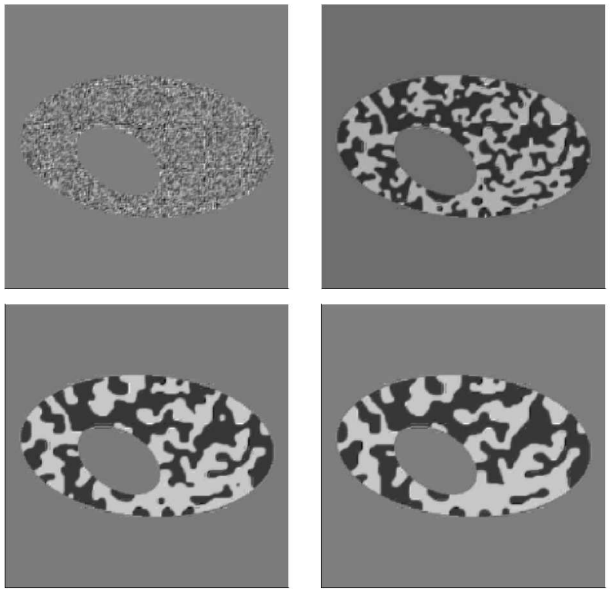

Figure 4.8: A solution of the Allen-Cahn equation with $\epsilon = 5 \times 10^{-6}$. Here, $\Delta t = 1$ and IMEX Euler's method is used. The upper left plot is the initial condition, and proceeding to the right and then down, the remaining plots are $t = 20$, $t = 60$, and $t = 100$.

Chapter 5

Fast Multipole Methods

Many problems in scientific computing require evaluating

$$\phi(\mathbf{x}_i) = \sum_{j=1}^{N} q_j K(\mathbf{y}_j, \mathbf{x}_i), \quad i = 1, \ldots, M,$$

where ϕ is called the potential, $\{\mathbf{y}_j\}_{j=1}^N \subset \mathbb{R}^n$ the source points, $\{q_j\}_{j=1}^N \subset \mathbb{R}$ the source strengths, $\{\mathbf{x}_i\}_{i=1}^M \subset \mathbb{R}^n$ the target points, and $K : \mathbb{R}^n \times \mathbb{R}^n \to \mathbb{R}$ the kernel. Evaluating discretizations of integral equations with the trapezoidal rule (3.3) or with Alpert's quadrature rules (3.5) are two examples of problems that require evaluating such sums. In the case of solving integral equations, the source and target points are the same

$$\phi(\mathbf{x}_i) = \sum_{\substack{j=1 \\ j \neq i}}^{N} q_j K(\mathbf{x}_j, \mathbf{x}_i), \quad i = 1, \ldots, N. \tag{5.1}$$

The target points correspond to the discretization locations, the kernel K corresponds to the kernel of the integral operator, and the potential corresponds to the evaluation of a layer potential at a discretization point. The source strengths correspond to the density function, the arclength term, the quadrature weights, and the Fourier interpolant. The diagonal terms of K usually require special treatment. For instance, for the trapezoidal rule (3.3), the diagonal term is replaced with an appropriate term involving the curvature at $\mathbf{x}_i$ (see Theorem 2.8).

Computing (5.1) directly for all $i = 1, \ldots, N$ requires $\mathcal{O}(N^2)$ operations. This is too expensive for the applications in mind and will not be considered further. Instead, we use a fast method to compute (5.1). The fast multipole method (FMM) was first introduced

by Greengard and Rokhlin [30]. It computes (5.1) in $\mathcal{O}(N)$ operations. Originally, it was designed for the kernel

$$K(\mathbf{x}_j, \mathbf{x}_i) = -\log(|\mathbf{x}_j - \mathbf{x}_i|).$$

Extensions of the original FMM include higher dimensions [8, 16, 31, 25], adaptive structures [8, 16, 17, 27], other kernels [17, 28, 29, 37], and kernel-free FMMs [49]. In the remainder of this chapter, we construct a FMM for the two-dimensional Yukawa potential.

We begin by defining the Yukawa potential in Section 5.1. We also state, and prove, the three classical translation operators of a FMM. In Section 5.2, we outline the key differences between the original adaptive FMM [12] and the FMM for the Yukawa potential. Section 5.3, we give timings for three problems that require evaluating the Yukawa potential. Finally, in Section 5.4, we discuss other fast methods that can be used to solve integral equations.

5.1 Yukawa Potential

The Yukawa potential is

$$\phi(\mathbf{x}) = \sum_{j=1}^{N} q_j K_0 \left(\frac{|\mathbf{x}_j - \mathbf{x}|}{\alpha} \right). \tag{5.2}$$

We evaluate ϕ and its normal derivatives with respect to its source location

$$\phi^{SL}(\mathbf{x}) = \sum_{j=1}^{N} q_j \frac{\partial}{\partial \nu_{\mathbf{x}}} K_0 \left(\frac{|\mathbf{x}_j - \mathbf{x}|}{\alpha} \right), \tag{5.3}$$

and its target location

$$\phi^{DL}(\mathbf{x}) = \sum_{j=1}^{N} q_j \frac{\partial}{\partial \nu_{\mathbf{x}_j}} K_0 \left(\frac{|\mathbf{x}_j - \mathbf{x}|}{\alpha} \right). \tag{5.4}$$

Equation (5.2) results from discretizations of the single layer potential (2.24), equation (5.3) results from discretizations of (2.27), and equation (5.4) results from discretizations of (2.29) and (2.31). In [17], a FMM for evaluating (4.4) is presented. In [12], a fully adaptive two-dimensional FMM for evaluating several potentials of the form (5.1) is presented. The combination of methods from these two papers results in a FMM for (5.2)–(5.4). We begin by defining the potential due to a set $S \subset \mathbb{R}^2$ with center $\mathbf{s}$.

Definition 5.1 *Given a set $S \subset \mathbb{R}^2$, the potential due to S is*

$$\phi_S(\mathbf{x}) = \sum_{\mathbf{x}_j \in S} q_j K_0 \left(\frac{|\mathbf{x}_j - \mathbf{x}|}{\alpha} \right).$$

The single layer and double layer potentials due to S are

$$\phi_S^{SL}(\mathbf{x}) = \sum_{\mathbf{x}_j \in S} q_j \frac{\partial}{\partial \nu_{\mathbf{x}}} K_0 \left(\frac{|\mathbf{x}_j - \mathbf{x}|}{\alpha} \right),$$
$$\phi_S^{DL}(\mathbf{x}) = \sum_{\mathbf{x}_j \in S} q_j \frac{\partial}{\partial \nu_{\mathbf{x}_j}} K_0 \left(\frac{|\mathbf{x}_j - \mathbf{x}|}{\alpha} \right).$$

The FMM requires a method to separate the kernel's dependence on two variables. This allows a set S of nearby source points to be grouped in an expansion for ϕ_S. Then, to evaluate $\phi_S(\mathbf{x})$, this expansion can be evaluated rather than computing $\phi_S(\mathbf{x})$ directly. In the original FMM [30], Taylor series are used. For (5.2), we use Graf's Addition Theorem [48, §11.3 Eqn 8].

Theorem 5.2 (Graf's Addition Theorem) *Let $\mathbf{x}, \mathbf{y} \in \mathbb{R}^2$ have polar coordinates $(|\mathbf{x}|, \theta_{\mathbf{x}})$ and $(|\mathbf{y}|, \theta_{\mathbf{y}})$ respectively and let $\theta_{\mathbf{y}}^{\mathbf{x}} = \theta_{\mathbf{y}-\mathbf{x}}$. If $|\mathbf{x}| > |\mathbf{y}|$,*

$$K_n \left(\frac{|\mathbf{y} - \mathbf{x}|}{\alpha} \right) e^{in(\theta_{\mathbf{y}}^{\mathbf{x}} - \theta_{\mathbf{x}} + \pi)} = \sum_{p=-\infty}^{\infty} K_{n+p} \left(\frac{|\mathbf{x}|}{\alpha} \right) I_p \left(\frac{|\mathbf{y}|}{\alpha} \right) e^{ip(\theta_{\mathbf{x}} - \theta_{\mathbf{y}})},$$

where I_p and K_p are the p^{th} order modified Bessel functions of the first and second kind respectively.

We use Graf's Addition Theorem to construct multipole and local expansions of ϕ_S, ϕ_S^{SL}, and ϕ_S^{DL}.

5.1.1 Multipole Expansions

A multipole expansion of a set S converges to $\phi_S(\mathbf{x})$ when $\mathbf{x}$ is sufficiently far from $\mathbf{s}$ (left plot of Figure 5.1). It is particularly useful if S contains a large number of points. Rather than evaluating the potential due to points in S directly, the multipole expansion can be evaluated. The multipole expansion is constructed with the following theorem.

Theorem 5.3 *Let $S \subset \mathbb{R}^2$ have center $\mathbf{s}$ and suppose*

$$|\mathbf{x} - \mathbf{s}| > |\mathbf{x}_j - \mathbf{s}|$$

for all $\mathbf{x}_j \in S$. Then, there exists coefficients $\{M_p\}_{p\in\mathbb{Z}} \subset \mathbb{C}$, independent of $\mathbf{x}$, such that

$$\phi_S(\mathbf{x}) = \sum_{p=-\infty}^{\infty} M_p K_p\left(\frac{|\mathbf{x}-\mathbf{s}|}{\alpha}\right) e^{ip\,\theta_{\mathbf{x}}^{\mathbf{s}}}. \tag{5.5}$$

The coefficients $\{M_p\}$ are called the multipole coefficients of ϕ_S. The series is called the multipole expansion of ϕ_S.

Proof By Graf's Addition Theorem,

$$\begin{aligned}
\phi_S(\mathbf{x}) &= \sum_{\mathbf{x}_j\in S} q_j K_0\left(\frac{|\mathbf{x}_j-\mathbf{x}|}{\alpha}\right) \\
&= \sum_{\mathbf{x}_j\in S} q_j K_0\left(\frac{|(\mathbf{x}_j-\mathbf{s})-(\mathbf{x}-\mathbf{s})|}{\alpha}\right) \\
&= \sum_{\mathbf{x}_j\in S} q_j \sum_{p=-\infty}^{\infty} K_p\left(\frac{|\mathbf{x}-\mathbf{s}|}{\alpha}\right) I_p\left(\frac{|\mathbf{x}_j-\mathbf{s}|}{\alpha}\right) e^{ip\,(\theta_{\mathbf{x}}^{\mathbf{s}}-\theta_{\mathbf{x}_j}^{\mathbf{s}})} \\
&= \sum_{p=-\infty}^{\infty} K_p\left(\frac{|\mathbf{x}-\mathbf{s}|}{\alpha}\right) e^{ip\,\theta_{\mathbf{x}}^{\mathbf{s}}} \sum_{\mathbf{x}_j\in S} q_j I_p\left(\frac{|\mathbf{x}_j-\mathbf{s}|}{\alpha}\right) e^{-ip\,\theta_{\mathbf{x}_j}^{\mathbf{s}}} \\
&= \sum_{p=-\infty}^{\infty} M_p K_p\left(\frac{|\mathbf{x}-\mathbf{s}|}{\alpha}\right) e^{ip\,\theta_{\mathbf{x}}^{\mathbf{s}}},
\end{aligned}$$

where

$$M_p = \sum_{\mathbf{x}_j\in S} q_j I_p\left(\frac{|\mathbf{x}_j-\mathbf{s}|}{\alpha}\right) e^{-ip\,\theta_{\mathbf{x}_j}^{\mathbf{s}}}. \tag{5.6}$$

□

A multipole expansion of ϕ_S^{SL} is

$$\begin{aligned}
\phi_S^{SL}(\mathbf{x}) &= \sum_{\mathbf{x}_j\in S} q_j \frac{\partial}{\partial \nu_{\mathbf{x}}} K_0\left(\frac{|\mathbf{x}_j-\mathbf{x}|}{\alpha}\right) \\
&= \frac{\partial}{\partial \nu_{\mathbf{x}}} \sum_{\mathbf{x}_j\in S} q_j K_0\left(\frac{|\mathbf{x}_j-\mathbf{x}|}{\alpha}\right) \\
&= \frac{\partial}{\partial \nu_{\mathbf{x}}} \sum_{p=-\infty}^{\infty} M_p K_p\left(\frac{|\mathbf{x}-\mathbf{s}|}{\alpha}\right) e^{ip\,\theta_{\mathbf{x}}^{\mathbf{s}}},
\end{aligned}$$

where $\{M_p\}$ are given by (5.6). Constructing a multipole expansion of ϕ_S^{DL} requires the calculation

$$\begin{aligned}
\phi_S^{DL}(\mathbf{x}) &= \sum_{\mathbf{x}_j \in S} q_j \frac{\partial}{\partial \nu_{\mathbf{x}_j}} K_0\left(\frac{|\mathbf{x}_j - \mathbf{x}|}{\alpha}\right) \\
&= \sum_{\mathbf{x}_j \in S} q_j \frac{\partial}{\partial \nu_{\mathbf{x}_j}} K_0\left(\frac{|(\mathbf{x}_j - \mathbf{s}) - (\mathbf{x} - \mathbf{s})|}{\alpha}\right) \\
&= \sum_{\mathbf{x}_j \in S} q_j \frac{\partial}{\partial \nu_{\mathbf{x}_j}} \sum_{p=-\infty}^{\infty} K_p\left(\frac{|\mathbf{x} - \mathbf{s}|}{\alpha}\right) I_p\left(\frac{|\mathbf{x}_j - \mathbf{s}|}{\alpha}\right) e^{ip\,(\theta_{\mathbf{x}}^{\mathbf{s}} - \theta_{\mathbf{x}_j}^{\mathbf{s}})} \\
&= \sum_{p=-\infty}^{\infty} K_p\left(\frac{|\mathbf{x} - \mathbf{s}|}{\alpha}\right) e^{ip\,\theta_{\mathbf{x}}^{\mathbf{s}}} \sum_{\mathbf{x}_j \in S} q_j \frac{\partial}{\partial \nu_{\mathbf{x}_j}} \left(I_p\left(\frac{|\mathbf{x}_j - \mathbf{s}|}{\alpha}\right) e^{-ip\,\theta_{\mathbf{x}_j}^{\mathbf{s}}}\right) \\
&= \sum_{p=-\infty}^{\infty} M_p K_p\left(\frac{|\mathbf{x} - \mathbf{s}|}{\alpha}\right) e^{ip\,\theta_{\mathbf{x}}^{\mathbf{s}}},
\end{aligned}$$

where

$$M_p = \sum_{\mathbf{x}_j \in S} q_j \frac{\partial}{\partial \nu_{\mathbf{x}_j}} \left(I_p\left(\frac{|\mathbf{x}_j - \mathbf{s}|}{\alpha}\right) e^{-ip\,\theta_{\mathbf{x}_j}^{\mathbf{s}}}\right).$$

Figure 5.1: The left plot is a set S (light gray), its center $\mathbf{s}$, and a collection of points $\mathbf{x}_j \in S$ (open circles). A multipole expansion of ϕ_S converges when $|\mathbf{x} - \mathbf{s}| > |\mathbf{x}_j - \mathbf{s}|$ for all $\mathbf{x}_j \in S$. In the right plot, the multipole expansion is shifted from $\mathbf{s}$ to $\tilde{\mathbf{s}}$. The new multipole expansion converges when $|\mathbf{x} - \tilde{\mathbf{s}}| > |\mathbf{s} - \tilde{\mathbf{s}}|$ (outside of the dark gray circle).

The FMM requires a method to shift the center of a multipole expansion (right plot of Figure 5.1). If this is not done, the complexity of forming all multipole coefficients would be $\mathcal{O}(N \log N)$. This shift is done with Theorem 5.4.

Theorem 5.4 *Suppose* $|\mathbf{x}-\mathbf{s}| > |\mathbf{x}_j-\mathbf{s}|$ *for all* $\mathbf{x}_j \in S$ *and*

$$\phi_S(\mathbf{x}) = \sum_{p=-\infty}^{\infty} M_p K_p\left(\frac{|\mathbf{x}-\mathbf{s}|}{\alpha}\right) e^{ip\,\theta_{\mathbf{x}}^{\mathbf{s}}}$$

is the multipole expansion of ϕ_S *centered at* $\mathbf{s}$*. Then, the center of the multipole expansion can be shifted to* $\tilde{\mathbf{s}}$

$$\phi_S(\mathbf{x}) = \sum_{p=-\infty}^{\infty} \widetilde{M}_p K_p\left(\frac{|\mathbf{x}-\tilde{\mathbf{s}}|}{\alpha}\right) e^{ip\,\theta_{\mathbf{x}}^{\tilde{\mathbf{s}}}},$$

and this new multipole expansion converges when $|\mathbf{x}-\tilde{\mathbf{s}}| > |\mathbf{s}-\tilde{\mathbf{s}}|$*.*

Proof By Graf's Addition Theorem,

$$\begin{aligned}
\phi_S(\mathbf{x}) &= \sum_{p=-\infty}^{\infty} M_p K_p\left(\frac{|\mathbf{x}-\mathbf{s}|}{\alpha}\right) e^{ip\,\theta_{\mathbf{x}}^{\mathbf{s}}} \\
&= \sum_{p=-\infty}^{\infty} M_p K_p\left(\frac{|(\mathbf{x}-\tilde{\mathbf{s}})-(\mathbf{s}-\tilde{\mathbf{s}})|}{\alpha}\right) e^{ip\,\theta_{\mathbf{x}}^{\mathbf{s}}} \\
&= \sum_{p=-\infty}^{\infty} M_p e^{ip\,\theta_{\mathbf{x}}^{\mathbf{s}}} \left(\sum_{n=-\infty}^{\infty} K_{p+n}\left(\frac{|\mathbf{x}-\tilde{\mathbf{s}}|}{\alpha}\right) I_n\left(\frac{|\mathbf{s}-\tilde{\mathbf{s}}|}{\alpha}\right) e^{in\,(\theta_{\mathbf{x}}^{\tilde{\mathbf{s}}}-\theta_{\mathbf{s}}^{\tilde{\mathbf{s}}})}\right) e^{-ip\,(\theta_{\mathbf{x}}^{\mathbf{s}}-\theta_{\mathbf{x}}^{\tilde{\mathbf{s}}}+\pi)} \\
&= \sum_{p=-\infty}^{\infty} M_p \sum_{n=-\infty}^{\infty} K_n\left(\frac{|\mathbf{x}-\tilde{\mathbf{s}}|}{\alpha}\right) I_{n-p}\left(\frac{|\mathbf{s}-\tilde{\mathbf{s}}|}{\alpha}\right) e^{i(n-p)\,(\theta_{\mathbf{x}}^{\tilde{\mathbf{s}}}-\theta_{\mathbf{s}}^{\tilde{\mathbf{s}}})} e^{ip\,(\theta_{\mathbf{x}}^{\tilde{\mathbf{s}}}-\pi)} \\
&= \sum_{p=-\infty}^{\infty} K_p\left(\frac{|\mathbf{x}-\tilde{\mathbf{s}}|}{\alpha}\right) e^{ip\,\theta_{\mathbf{x}}^{\tilde{\mathbf{s}}}} \sum_{n=-\infty}^{\infty} M_n I_{p-n}\left(\frac{|\mathbf{s}-\tilde{\mathbf{s}}|}{\alpha}\right) e^{-i(p-n)\,\theta_{\mathbf{s}}^{\tilde{\mathbf{s}}}} e^{-in\pi} \\
&= \sum_{p=-\infty}^{\infty} \widetilde{M}_p K_p\left(\frac{|\mathbf{x}-\tilde{\mathbf{s}}|}{\alpha}\right) e^{ip\,\theta_{\mathbf{x}}^{\tilde{\mathbf{s}}}},
\end{aligned}$$

where

$$\widetilde{M}_p = \sum_{n=-\infty}^{\infty} M_n I_{p-n}\left(\frac{|\mathbf{s}-\tilde{\mathbf{s}}|}{\alpha}\right) e^{-i(p-n)\,\theta_{\mathbf{s}}^{\tilde{\mathbf{s}}}} e^{-in\pi}. \tag{5.7}$$

□

Since the multipole expansion of ϕ_S^{DL} is in the form (5.5), we can use Theorem 5.4 to shift its center. Shifting the center of ϕ_S^{SL} is accomplished by interchanging the summation and normal derivative.

5.1.2 Local Expansions

Multipole expansions of $\phi_S(\mathbf{x})$ could be evaluated at a large number of points, but instead, we convert the multipole expansion to a local expansion and then evaluate locally. This reduces the complexity of evaluating ϕ_S at all target points from $\mathcal{O}(N \log N)$ to $\mathcal{O}(N)$. Suppose $\widetilde{S}$ has center $\tilde{\mathbf{s}}$ with $|\mathbf{x} - \tilde{\mathbf{s}}| < |\mathbf{s} - \tilde{\mathbf{s}}|$ for all $\mathbf{x} \in \widetilde{S}$. Then, the multipole expansion of ϕ_S can be converted to a local expansion centered at $\tilde{\mathbf{s}}$ (Figure 5.2) with the following theorem.

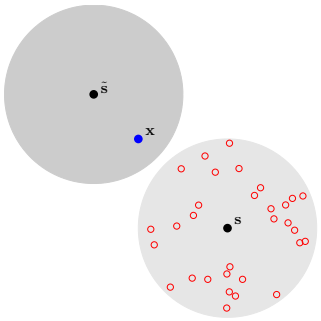

Figure 5.2: A set S (light gray), its center $\mathbf{s}$, and a collection of $\mathbf{x}_j \in S$ (open circles). The multipole expansion of ϕ_S is converted to a local expansion centered at $\tilde{\mathbf{s}}$ and converges in $\widetilde{S}$ (dark gray).

Theorem 5.5 *Suppose* $|\mathbf{x} - \mathbf{s}| > |\mathbf{x}_j - \mathbf{s}|$ *for all* $\mathbf{x}_j \in S$ *and*

$$\phi_S(\mathbf{x}) = \sum_{p=-\infty}^{\infty} M_p K_p \left(\frac{|\mathbf{x} - \mathbf{s}|}{\alpha} \right) e^{ip\,\theta_{\mathbf{x}}^{\mathbf{s}}}$$

is a multipole expansion of ϕ_S *centered at* $\mathbf{s}$*. Then, if* $|\mathbf{x} - \tilde{\mathbf{s}}| < |\mathbf{s} - \tilde{\mathbf{s}}|$*, there exist coefficients* $\{L_p\}_{p \in \mathbb{Z}} \subset \mathbb{C}$*, independent of* $\mathbf{x}$*, such that*

$$\phi_S(\mathbf{x}) = \sum_{p=-\infty}^{\infty} L_p I_p \left(\frac{|\mathbf{x} - \tilde{\mathbf{s}}|}{\alpha} \right) e^{-ip\,\theta_{\mathbf{x}}^{\tilde{\mathbf{s}}}}. \tag{5.8}$$

The coefficients $\{L_p\}$ *are called the local coefficients of* ϕ_S*. The series is called the local expansion of* ϕ_S*.*

Proof By Graf's Addition Theorem,

$$\begin{aligned}
\phi_S(\mathbf{x}) &= \sum_{p=-\infty}^{\infty} M_p K_p \left(\frac{|\mathbf{x}-\mathbf{s}|}{\alpha}\right) e^{ip\,\theta_{\mathbf{x}}^{\mathbf{s}}} \\
&= \sum_{p=-\infty}^{\infty} M_p K_p \left(\frac{|(\mathbf{x}-\tilde{\mathbf{s}})-(\mathbf{s}-\tilde{\mathbf{s}})|}{\alpha}\right) e^{ip\,\theta_{\mathbf{x}}^{\mathbf{s}}} \\
&= \sum_{p=-\infty}^{\infty} M_p e^{ip\,\theta_{\mathbf{x}}^{\mathbf{s}}} \sum_{n=-\infty}^{\infty} K_{p+n}\left(\frac{|\mathbf{s}-\tilde{\mathbf{s}}|}{\alpha}\right) I_n\left(\frac{|\mathbf{x}-\tilde{\mathbf{s}}|}{\alpha}\right) e^{in\,(\theta_{\mathbf{s}}^{\tilde{\mathbf{s}}}-\theta_{\mathbf{x}}^{\tilde{\mathbf{s}}})} e^{-ip\,(\theta_{\mathbf{x}}^{\mathbf{s}}-\theta_{\mathbf{s}}^{\tilde{\mathbf{s}}}+\pi)} \\
&= \sum_{p=-\infty}^{\infty} I_p\left(\frac{|\mathbf{x}-\tilde{\mathbf{s}}|}{\alpha}\right) e^{-ip\,\theta_{\mathbf{x}}^{\tilde{\mathbf{s}}}} \sum_{n=-\infty}^{\infty} M_n K_{n+p}\left(\frac{|\mathbf{s}-\tilde{\mathbf{s}}|}{\alpha}\right) e^{i(p+n)\,\theta_{\mathbf{s}}^{\tilde{\mathbf{s}}}} e^{-in\pi} \\
&= \sum_{p=-\infty}^{\infty} L_p I_p\left(\frac{|\mathbf{x}-\tilde{\mathbf{s}}|}{\alpha}\right) e^{-ip\,\theta_{\mathbf{x}}^{\tilde{\mathbf{s}}}},
\end{aligned}$$

where

$$L_p = \sum_{n=-\infty}^{\infty} M_n K_{n+p}\left(\frac{|\mathbf{s}-\tilde{\mathbf{s}}|}{\alpha}\right) e^{i(p+n)\,\theta_{\mathbf{s}}^{\tilde{\mathbf{s}}}} e^{-in\pi}. \tag{5.9}$$

□

The multipole expansions ϕ_S^{SL} and ϕ_S^{DL} are converted to local expansions in a similar fashion to how we shift their multipole expansions. This conversion only requires taking the normal derivative of the correct terms.

To construct the third translation operator, we require another addition theorem similar to Graf's Addition Theorem [48, §11.3 Eqn 7].

Theorem 5.6 *Let* $\mathbf{x}$ *and* $\mathbf{y}$ *have polar coordinates* $(|\mathbf{x}|, \theta_{\mathbf{x}})$ *and* $(|\mathbf{y}|, \theta_{\mathbf{y}})$ *respectively. Then, with no restrictions on* $\mathbf{x}$ *and* $\mathbf{y}$*,*

$$I_p\left(\frac{|\mathbf{y}-\mathbf{x}|}{\alpha}\right) e^{-ip(\theta_{\mathbf{y}}^{\mathbf{x}}-\theta_{\mathbf{y}})} = \sum_{n=-\infty}^{\infty} I_n\left(\frac{|\mathbf{x}|}{\alpha}\right) I_{p+n}\left(\frac{|\mathbf{y}|}{\alpha}\right) e^{in(\theta_{\mathbf{x}}-\theta_{\mathbf{y}}+\pi)}.$$

Using Theorem 5.6, we can shift the center of a local expansion.

Theorem 5.7 *The center of a local expansion can be shifted from* $\mathbf{s}$ *to* $\tilde{\mathbf{s}}$

$$\sum_{p=-\infty}^{\infty} L_p I_p\left(\frac{|\mathbf{x}-\mathbf{s}|}{\alpha}\right) e^{-ip\,\theta_{\mathbf{x}}^{\mathbf{s}}} = \sum_{p=-\infty}^{\infty} \widetilde{L}_p I_p\left(\frac{|\mathbf{x}-\tilde{\mathbf{s}}|}{\alpha}\right) e^{-ip\,\theta_{\mathbf{x}}^{\tilde{\mathbf{s}}}}.$$

Proof

$$
\begin{aligned}
&\sum_{p=-\infty}^{\infty} L_p I_p\left(\frac{|\mathbf{x}-\mathbf{s}|}{\alpha}\right) e^{-ip\,\theta_{\mathbf{x}}^{\mathbf{s}}} \\
&= \sum_{p=-\infty}^{\infty} L_p I_p\left(\frac{|(\mathbf{x}-\tilde{\mathbf{s}})-(\mathbf{s}-\tilde{\mathbf{s}})|}{\alpha}\right) e^{-ip\,\theta_{\mathbf{x}}^{\mathbf{s}}} \\
&= \sum_{p=-\infty}^{\infty} L_p e^{-ip\,\theta_{\mathbf{x}}^{\mathbf{s}}}\left(\sum_{n=-\infty}^{\infty} I_n\left(\frac{|\mathbf{s}-\tilde{\mathbf{s}}|}{\alpha}\right) I_{p+n}\left(\frac{|\mathbf{x}-\tilde{\mathbf{s}}|}{\alpha}\right) e^{in\,(\theta_{\mathbf{s}}^{\tilde{\mathbf{s}}}-\theta_{\mathbf{x}}^{\tilde{\mathbf{s}}}+\pi)}\right) e^{ip\,(\theta_{\mathbf{x}}^{\mathbf{s}}-\theta_{\mathbf{x}}^{\tilde{\mathbf{s}}})} \\
&= \sum_{p=-\infty}^{\infty} L_p \sum_{n=-\infty}^{\infty} I_{n-p}\left(\frac{|\mathbf{s}-\tilde{\mathbf{s}}|}{\alpha}\right) I_n\left(\frac{|\mathbf{x}-\tilde{\mathbf{s}}|}{\alpha}\right) e^{i(n-p)(\theta_{\mathbf{s}}^{\tilde{\mathbf{s}}}-\theta_{\mathbf{x}}^{\tilde{\mathbf{s}}}+\pi)} e^{-ip\,\theta_{\mathbf{x}}^{\tilde{\mathbf{s}}}} \\
&= \sum_{p=-\infty}^{\infty} I_p\left(\frac{|\mathbf{x}-\tilde{\mathbf{s}}|}{\alpha}\right) e^{-ip\,\theta_{\mathbf{x}}^{\tilde{\mathbf{s}}}} \sum_{n=-\infty}^{\infty} L_n I_{p-n}\left(\frac{|\mathbf{s}-\tilde{\mathbf{s}}|}{\alpha}\right) e^{i(p-n)(\theta_{\mathbf{s}}^{\tilde{\mathbf{s}}}+\pi)} \\
&= \sum_{p=-\infty}^{\infty} \widetilde{L}_p I_p\left(\frac{|\mathbf{x}-\tilde{\mathbf{s}}|}{\alpha}\right) e^{-ip\,\theta_{\mathbf{x}}^{\tilde{\mathbf{s}}}},
\end{aligned}
$$

where

$$
\widetilde{L}_p = \sum_{n=-\infty}^{\infty} L_n I_{p-n}\left(\frac{|\mathbf{s}-\tilde{\mathbf{s}}|}{\alpha}\right) e^{i(p-n)(\theta_{\mathbf{s}}^{\tilde{\mathbf{s}}}+\pi)}. \tag{5.10}
$$

□

5.1.3 Plane Wave Expansions

Plane wave expansions are used to further accelerate the FMM. We briefly show how to convert a multipole expansion to a plane wave expansion. A detailed account can be found in Appendix A of [17] and references therein. Let $x > 0$ and $(x, y) \in \mathbb{R}^2$ have polar coordinates (r, θ). Then,

$$
\begin{aligned}
K_n\left(\frac{r}{\alpha}\right) e^{in\theta} = \frac{1}{2}\int_0^{\infty} \frac{e^{-x\sqrt{\lambda^2+1/\alpha^2}}}{\sqrt{\lambda^2+1/\alpha^2}} \Big[& e^{i\lambda y}\alpha^n\left(\sqrt{\lambda^2+1/\alpha^2}+\lambda\right)^n \\
& + e^{-i\lambda y}\alpha^n\left(\sqrt{\lambda^2+1/\alpha^2}-\lambda\right)^n\Big]\, d\lambda.
\end{aligned} \tag{5.11}
$$

There exists similar integral representations for $x < 0$, $y > 0$, and $y < 0$. Using quadrature rules for these representations, we can convert a multipole expansion (5.5) to a plane wave (exponential) expansion. Using the property $e^{x+y} = e^x e^y$, the center of the plane wave

expansion can be shifted to a new center. Then, the plane wave expansion is converted to a local expansion using the formula [1, Eqn 9.6.19]

$$e^{z\cos(\theta)} = I_0(z) + 2\sum_{k=1}^{\infty} I_k(z)cos(k\theta). \tag{5.12}$$

Quadrature rules for infinite integrals such as (5.11) are discussed in [17].

5.2 Yukawa FMM

We do not introduce typical definitions of the FMM such as the interaction list and the near neighbors as these definitions are well presented in [12]. Rather, we outline the key points that pertain to the Yukawa potential.

The FMM requires computing several infinite summations. In particular, evaluating multipole and local expansions as well as the translation operators (5.7) and (5.9). These summations are truncated at some level P. For instance,

$$\phi_S(\mathbf{x}) = \sum_{p=-\infty}^{\infty} M_p K_p\left(\frac{|\mathbf{x}-\mathbf{s}|}{\alpha}\right) e^{ip\,\theta_{\mathbf{x}}^{\mathbf{s}}} \approx \sum_{p=-P}^{P} M_p K_p\left(\frac{|\mathbf{x}-\mathbf{s}|}{\alpha}\right) e^{ip\,\theta_{\mathbf{x}}^{\mathbf{s}}}.$$

Sharp bounds on this error have not been established, but myself and the authors of [17] have observed numerically that 16 digits accuracy are achieved with $P = 42$ and 8 digits accuracy are achieved with $P = 21$. Similar results are also found in [3] for the FMM applied to Helmholtz equation $\Delta u + k^2 u = 0$. Truncating the summations at P results in the following complexities:

- Forming the multipole expansion (5.6) due to a single point requires $\mathcal{O}(P)$ operations.
- Translating a multipole expansion (5.7) requires $\mathcal{O}(P^2)$ operations.
- Converting a multipole expansion to a local expansion (5.9) requires $\mathcal{O}(P^2)$ operations.
- Translating a local expansion (5.10) requires $\mathcal{O}(P^2)$ operations.
- Evaluating a multipole expansion (5.5) or local expansion (5.8) at a single point requires $\mathcal{O}(P)$ operations.

These complexities assume that symmetries such as $M_{-p} = \overline{M_p}$ and $L_{-p} = \overline{L_p}$ are exploited.

5.2.1 Quadtree Construction

The FMM starts with a quadtree structure similar to that generated in Chapter 4. We outline the key characteristics of the quadtrees required for the Yukawa potential. A more thorough construction of quadtrees is found in [12]. The notions of grid level, children, and childless boxes remain unchanged. When constructing the quadtree, a box is subdivided if it contains more than some preset maximum number of points n_{max}. Unlike the quadtree constructed in Chapter 4, there are no restrictions on neighboring boxes. Figure 5.4 illustrates a typical quadtree with 32,768 particles inside $[-1/2, 1/2]^2$. Each childless box has less than 30 particles. Figure 5.5 is a typical quadtree for an integral equation. The quadtree is far from uniform because the particles lie on one-dimensional curves.

5.2.2 Forming Expansions

The goal of the FMM is to form local expansions that converge to the potential due to all points that are sufficiently far from the center of the expansion. This is done in a hierarchical manner by forming multipole expansions (5.6), shifting multipole expansions (5.7), converting them to local expansions (5.9), and shifting local expansions (5.10).

Suppose we have constructed a quadtree with M total boxes for N source points. We construct multipole expansions, local expansions, and plane wave expansions for $\phi_S(\mathbf{x})$ (or $\phi_S^{SL}(\mathbf{x})$ or $\phi_S^{DL}(\mathbf{x})$) for all boxes S in the quadtree. The multipole coefficients are formed first. Beginning at the finest level of the quadtree, if a box S is childless, its multipole coefficients are formed with (5.6); for boxes with children, its multipole expansion is formed by summing the multipole expansions of its children. This requires shifting each child's center to the center of the parent using (5.7). Since every particle is contained in exactly one childless box, $\mathcal{O}(NP)$ operations are required to form the multipole coefficients of the childless boxes. $\mathcal{O}(MP^2)$ operations are required to shift each multipole expansion to its parent.

Once multipole coefficients are formed for all boxes, we construct local expansions from the coarsest to finest level. For each box s, we convert the multipole expansions of its interaction list to a local expansion centered at s using (5.9). Then, the local expansion is translated to the four children of s using (5.10). A box has at most 27 boxes in its interaction list, thus $\mathcal{O}(27MP^2)$ operations are required to convert multipole expansions to local expansions. Shifting the local expansions from the parent boxes to their four children

requires $\mathcal{O}(MP^2)$ operations.

The most expensive part of the FMM is translating multipole expansions to local expansions. Alternatively, we can use plane wave expansions. Converting a multipole expansion to a plane wave expansion (5.11) and a plane wave expansion to a local expansion (5.12) each require $\mathcal{O}(P^2)$ operations. However, translating a plane wave expansion to 27 new centers requires $\mathcal{O}(27P)$ instead of $\mathcal{O}(27P^2)$ operations.

Defining the interaction list and near neighbors is sufficient for a uniform quadtree. However, for an adaptive quadtree, some additional care must be taken. In Figure 5.3, the potential due to S (the shaded region) needs to evaluated at points inside $\widetilde{S}$. Direct calculations can not be used since S may contain more than n_{max} particles. The multipole expansion of S can not be translated to a local expansion of $\widetilde{S}$ since it will not converge in all of $\widetilde{S}$. However, the multipole expansion of S converges at every point in $\widetilde{S}$. Therefore, for each point $\mathbf{x} \in \widetilde{S}$, we evaluate the multipole expansion of ϕ_S. These added complications to adaptive quadtrees are addressed in [12], and are called *List 1*, *List 2*, *List 3*, *List 4*, and *List 5*. In Figure 5.3, the shaded box is in *List 3* of $\widetilde{S}$.

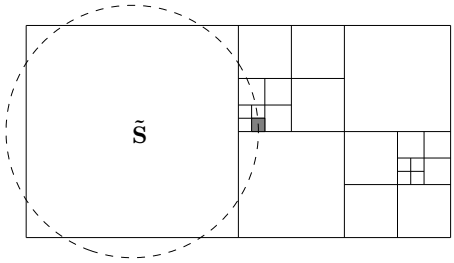

Figure 5.3: A box $\widetilde{S}$ and a box S (shaded region) that has too many particles to evaluate ϕ_S directly and is too close to $\widetilde{S}$ to translate the multipole coefficients to local coefficients (the local expansion would only converges inside the circle). Alternatively, the multipole expansion of ϕ_S is evaluated at all points in $\widetilde{S}$.

Once all the local expansions are formed, the result is an expansion for each childless box s that converges to the potential due to all particles that are well-separated from s. The

potential due to the remainder of the particles is handled either with one of the five lists, or is handled directly. The FMM is constructed so that the total number of points that is handled directly is $\mathcal{O}(1)$. So, to evaluate the potential at a single point, we require $\mathcal{O}(P)$ operations to evaluate the local expansion, $\mathcal{O}(1)$ operations to evaluate the particles that are done directly, and $\mathcal{O}(MP^3)$ operations (see [12]) to handle the nonadaptive quadtree complexities. The result is a method whose operation count scales asymptotically with N.

5.3 Numerical Examples

We compare timings and errors for the FMM. We start with a simple configuration for an increasing number of points N. Then, we look at timings for solving the modified Helmholtz equation with Dirichlet boundary conditions (2.21) and Neumann boundary conditions (2.22).

5.3.1 Timings for N Random Points

We evaluate the Yukawa potential $\phi(\mathbf{x})$ at N points with half of them randomly distributed in $[-1/2, 1/2]^2$ and the other half distributed on two elliptical boundaries (Figure 5.4). The results in Table 5.1 verify the quadratic scaling in the direct calculation, the near-linear scaling in the FMM, and the speedup that results from introducing plane wave expansions. The errors of the FMM without the plane wave expansion agree with the truncation level, $P = 41$, of the expansions. The error of the FMM with plane wave expansions is slightly larger since the quadrature rules for the plane wave expansions only guarantee 13 digits accuracy.

5.3.2 Timings for a Dirichlet Problem

We present timings in Table 5.2 for solving the integral equation for the interior Dirichlet example in Chapter 3. We solve the integral equation with the trapezoidal rule, and with Alpert's quadrature rule with error $\mathcal{O}(h^8 \log h)$. The total number of GMRES iterations is 45. We also list the size of the quadtree and the time required for its generation. The top two plots of Figure 5.5 illustrate the quadtree when $N = 2816$.

We can conclude that the FMM is achieving linear scaling for the trapezoidal rule, and near-linear scaling for Alpert's quadrature rules. The reduction in speed results from the

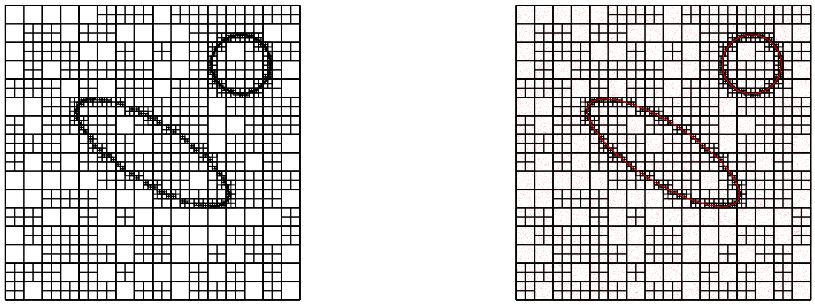

Figure 5.4: In the left plot is the quadtree without particles. The particles are included in the right plot. Here, $N = 32,768$ and no more than 30 points are in each childless box.

N	Direct	Original FMM	Max Error	Plane Wave FMM	Max Error
64	0.01	0.06	2.22×10^{-15}	0.06	2.22×10^{-15}
128	0.03	0.08	1.85×10^{-14}	0.08	1.85×10^{-14}
256	0.08	0.22	8.88×10^{-15}	0.12	2.93×10^{-14}
512	0.30	0.47	8.88×10^{-15}	0.21	2.77×10^{-13}
1,024	1.15	1.03	1.11×10^{-14}	0.36	3.44×10^{-13}
2,048	4.59	2.02	1.60×10^{-14}	0.60	3.52×10^{-13}
4,096	18.26	3.86	2.09×10^{-14}	1.36	3.65×10^{-13}
8,192	73.42	9.46	2.88×10^{-14}	2.02	3.22×10^{-13}
16,384	292.52	14.80	3.69×10^{-14}	4.60	5.26×10^{-13}
32,768	1168.22	38.44	6.00×10^{-14}	7.04	3.44×10^{-13}
65,536	4689.96	56.55	8.08×10^{-14}	17.42	3.61×10^{-13}

Table 5.1: A comparison of the CPU time (in seconds) required to compute the potential due to a set a points directly, via the original FMM , and via the FMM with plane wave expansions. Half of the points are randomly placed in the unit square and the other half are concentrated on two elliptical boundaries.

N	Quadtree Size	Quadtree Time	Trapezoidal Time	Quadrature Time
704	42 (4)	0.02	11.97	13.05
1,408	111 (5)	0.02	20.11	2.38
2,816	183 (7)	0.02	40.09	44.38
5,632	331 (8)	0.03	80.19	89.36

Table 5.2: A comparison of the CPU time (in seconds) to compute the quadtree, solve the integral equation with the trapezoidal rule, and solve the integral equation with Alpert's quadrature rules. Also listed is the size of the quadtree with its finest level in parentheses.

Fourier transforms computed from using the Fourier interpolant discussed in Section 3.2. We also see that the time required to generate the quadtree is negligible.

5.3.3 Timings for a Neumann Problem

We present timings in Table 5.3 for solving the integral equation for the exterior Neumann example in Chapter 3. We solve the integral equation with the trapezoidal rule and with Alpert's quadrature rule with error $\mathcal{O}(h^8 \log h)$. Here, $\alpha = 1$, which requires 23 GMRES iterations to solve the integral equation. The bottom two plots of Figure 5.5 illustrate the quadtree when $N = 2560$.

N	Quadtree Size	Quadtree Time	Trapezoidal Time	Quadrature Time
640	34 (4)	0.01	3.96	4.50
1,280	93 (5)	0.01	5.87	6.91
2,560	163 (7)	0.01	12.01	13.69
5,120	308 (8)	0.03	23.81	27.82

Table 5.3: A comparison of the CPU time (in seconds) to compute the quadtree, solve the integral equation with the trapezoidal rule, and solve the integral equation with Alpert's quadrature rules. Also listed is the size of the quadtree with its finest level in parentheses.

We can draw the same conclusions as with the previous example. The trapezoidal rule is computed in linear time and Alpert's quadrature rules in near-linear time. The drastic reduction in computational time when comparing Tables 5.2 and 5.3 is attributed to the required number of GMRES steps. The Neumann problem only required 23 while the Dirichlet problem required 45.

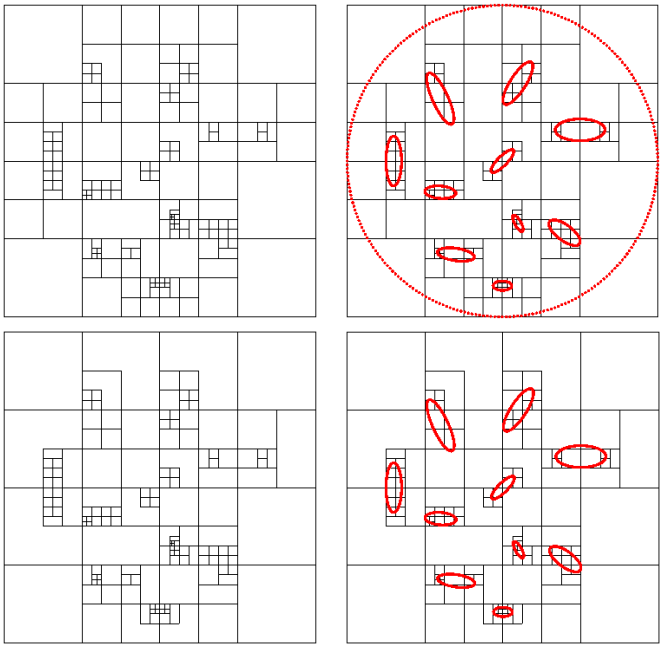

Figure 5.5: The quadtrees for the interior problem (top two figures) and for the exterior problem (bottom two figures). The interior problem has 2816 particles and the exterior problem has 2560 particles.

5.4 Other Fast Methods

There are other fast methods that have been developed for evaluating (5.1). Tree-code methods, first introduced in [6], closely resemble the FMM. As in the FMM, tree-code methods form multipole expansions of a quadtree; however, they do not form local expansions. Also, the multipole expansion of every box in the quadtree are formed directly as in (5.6). Since every particle is in exactly one box at each level of the quadtree, forming the multipole expansions requires $\mathcal{O}(PN \log N)$ operations. Then, for each particle, a sequence of expansions of well-separated boxes needs to be evaluated. The overall complexity of a tree-code method is $\mathcal{O}(N \log N)$.

A new and promising method for solving integral equations is direct methods [40]. Unlike iterative solvers, these methods construct a compressed factorization of the inverse of the matrix corresponding to the discretization of the integral equation. The cost of initially computing the inverse may cost more than the FMM. For instance, in [40], Laplace's equation with Dirichlet boundary conditions is solved in an exterior domain with $N = 102,400$ points. The direct method required 13 seconds to solve the integral equation whereas the FMM matrix-vector multiply required 0.96 seconds. Thus, if the GMRES count is less than 13, the FMM outperforms the direct method. However, once the inverse is computed, it only requires 0.12 seconds to apply it to a right-hand side. This is of particular interest to work in this thesis since at each time step, the same integral equation must always be solved, only with a different right-had side.

Chapter 6

Conclusions and Future Direction

6.1 Future Direction

A general framework has been laid out for solving the nonlinear heat equation in multiply-connected two-dimensional domains. However, to be able to apply this machinery in a more general setting, issues that need to be resolved are:

- The extension of g throughout the computational domain D remains an open problem. For the fourth-order solver developed in [17], a C^2 extension may be sufficient, but more smoothness would be required if a higher-order volume integral was developed.
- In order to resolve solution features that may appear or disappear, such as in the Allen-Cahn equation, it may be necessary to dynamically generate the quadtree throughout the simulation. However, generating the quadtree for the forced problem is expensive and information would have to be transferred from one quadtree to another.
- The near-singular integration strategy was implemented and tested on the forced modified Helmholtz equation. However, it has not been applied in a general time-stepping scheme.

Other applications require the solution of fourth-order PDEs. We discuss two such problems.

6.1.1 The Navier-Stokes Equations in Two Dimensions

The two-dimensional incompressible Navier-Stokes equations

$$\begin{aligned}
\frac{\partial \mathbf{u}}{\partial t} + (\mathbf{u}\cdot\nabla)\mathbf{u} &= \frac{1}{Re}(-\nabla p + \Delta \mathbf{u}), && \mathbf{x}\in\Omega, t>0,\\
\nabla\cdot\mathbf{u} &= 0, && \mathbf{x}\in\Omega, t>0,\\
\mathbf{u} &= \mathbf{h}, && \mathbf{x}\in\Gamma, t>0,\\
\mathbf{u} &= \mathbf{u}_0, && \mathbf{x}\in\Omega, t=0,
\end{aligned}$$

can be recast by introducing a stream function ψ satisfying

$$\mathbf{u} = (\psi_y, -\psi_x).$$

ψ satisfies

$$\frac{\partial}{\partial t}\Delta\psi - \frac{1}{Re}\Delta^2\psi = J[\psi,\Delta\psi], \quad \mathbf{x}\in\Omega, t>0, \tag{6.1a}$$

$$\nabla\psi = \mathbf{h}^{\perp}, \quad \mathbf{x}\in\Gamma, t>0, \tag{6.1b}$$

$$\nabla\psi = \mathbf{u}_0^{\perp}, \quad \mathbf{x}\in\Omega, t=0, \tag{6.1c}$$

where $(x,y)^{\perp} = (-y,x)$ and J is the Jacobian operator $J[u,v] = u_x v_y - u_y v_x$. The stream function formulation guarantees $\mathbf{u}$ will satisfy the incompressibility constraint and eliminates the pressure term. However, the order of the PDE is increased from two to four.

We discretize (6.1) in time and treat the stiff term, in this case the biharmonic term, implicitly. The simplest example is

$$\begin{aligned}
\frac{\Delta\psi^{N+1}-\Delta\psi^{N}}{dt} - \frac{1}{Re}\Delta^2\psi^{N+1} &= J[\psi^N,\Delta\psi^N], && \mathbf{x}\in\Omega,\\
\nabla\psi^{N+1} &= \mathbf{h}^{\perp}, && \mathbf{x}\in\Gamma,\\
\psi^0 &= \mathbf{u}_0^{\perp}, && \mathbf{x}\in\Omega.
\end{aligned} \tag{6.2}$$

Rearranging (6.2),

$$(\Delta - \alpha^2\Delta^2)\psi^{N+1} = \Delta\psi^N + dtJ[\psi^N,\Delta\psi^N],$$

where $\alpha^2 = dt/Re$. As we saw in Chapter 2, regardless of the IMEX method, the PDE to be solved at each time step is

$$(\Delta - \alpha^2\Delta^2)\psi^{N+1} = b,$$

where $b = b[\psi^N, \Delta\psi^N, \psi^{N-1}, \Delta\psi^{N-1}, \ldots, \psi^{N-p+1}, \Delta\psi^{N-p+1}]$. Thus, we develop integral equation methods for

$$\begin{aligned}(\Delta - \alpha^2\Delta^2)\psi &= g, \quad \mathbf{x} \in \Omega,\\ \frac{\partial\psi}{\partial\nu} &= f_1, \quad \mathbf{x} \in \Gamma,\\ \frac{\partial\psi}{\partial\tau} &= f_2, \quad \mathbf{x} \in \Gamma,\end{aligned}$$

where $\tau = \nu^\perp$, $f_1 = \mathbf{h}^\perp \cdot \nu$, and $f_2 = \mathbf{h}^\perp \cdot \tau$. We adopt the same strategy of writing $\psi = \psi^P + \psi^H$ where

$$(\Delta - \alpha^2\Delta^2)\psi^P = g,$$

and

$$\begin{aligned}(\Delta - \alpha^2\Delta^2)\psi^H &= 0,\\ \frac{\partial\psi^H}{\partial\nu} &= f_1 - \frac{\partial\psi^P}{\partial\nu},\\ \frac{\partial\psi^H}{\partial\tau} &= f_2 - \frac{\partial\psi^P}{\partial\tau}.\end{aligned}$$

This methodology for solving the two-dimensional Navier-Stokes equations was adopted in [38]. Rather than using integral equations, the PDEs were solved with a Fourier expansion in the azimuthal direction and a Chebyshev expansion in the radial direction. However, this method requires the domain to be circular. We wish to extend the work to more general domains.

Progress towards solving the homogeneous problem is now discussed. To simplify notation, we let $\lambda = 1/\alpha$, redefine f_1 and f_2, and multiply the homogeneous PDE by -1,

$$(\Delta^2 - \lambda^2\Delta)\psi^H = 0, \quad \mathbf{x} \in \Omega, \tag{6.3a}$$

$$\frac{\partial\psi^H}{\partial\nu} = f_1, \quad \mathbf{x} \in \Gamma, \tag{6.3b}$$

$$\frac{\partial\psi^H}{\partial\tau} = f_2, \quad \mathbf{x} \in \Gamma. \tag{6.3c}$$

We also assume that the domain Ω is a simply-connected bounded domain. Exterior and multiply-connected domains will lead to a rank deficiency in the upcoming integral equations, and an approach such as that taken in [24] will have to be implemented.

We begin with finding the fundamental solution G of $(\Delta^2 - \lambda^2\Delta)$. The fundamental solution $(\Delta - \lambda^2)$ is

$$-\frac{1}{2\pi}K_0(\lambda|\mathbf{x}|),$$

so, G satisfies the PDE

$$\Delta G = -\frac{1}{2\pi}K_0(\lambda|\mathbf{x}|).$$

Moving to polar coordinates

$$\frac{1}{r}\frac{\partial}{\partial r}\left(r\frac{\partial G}{\partial r}\right) = -\frac{1}{2\pi}K_0(\lambda r).$$

Multiplying by r and integrating,

$$r\frac{\partial G}{\partial r} = -\frac{-\lambda r K_1(\lambda r) + 1}{2\pi\lambda^2}.$$

Dividing by r and integrating,

$$G(r) = -\frac{1}{2\pi\lambda^2}(\log r + K_0(\lambda r)).$$

Thus, the fundamental solution of $(\Delta^2 - \lambda^2\Delta)$ is

$$G(\mathbf{x}) = -\frac{1}{2\pi\lambda^2}(\log|\mathbf{x}| + K_0(\lambda|\mathbf{x}|))$$

Since there are two boundary conditions, two layer potentials are required. We seek a solution in the form

$$\psi^H(\mathbf{x}) = \int_\Gamma G_1(\mathbf{y}-\mathbf{x})\sigma_1(\mathbf{y})ds_\mathbf{y} + \int_\Gamma G_2(\mathbf{y}-\mathbf{x})\sigma_2(\mathbf{y})ds_\mathbf{y},$$

where G_1 and G_2 are linear combinations of derivatives of G. Then, ψ^H automatically satisfies (6.3a). The boundary conditions (6.3b) and (6.3c) are found by solving a system of integral equations. The system of integral equation is constructed by taking the limit of the normal and tangential derivatives of ψ^H and matching them with f_1 and f_2 respectively. We pick G_1 and G_2 so that the system is well-conditioned and the diagonal terms are computationally manageable. Using (2.19), the asymptotic expansion of G at the origin is

$$\frac{1}{8\pi}\log|\mathbf{x}|\left(|\mathbf{x}|^2 + \frac{1}{16}\lambda^2|\mathbf{x}|^4 + \mathcal{O}(|\mathbf{x}|^6)\right) + p(\lambda|\mathbf{x}|),$$

where p is an even polynomial. Thus, the singularity of G is

$$\frac{1}{8\pi}|\mathbf{x}|^2 \log|\mathbf{x}|,$$

which is the fundamental solution of the biharmonic operator Δ^2. The biharmonic equation was solved using a system of integral equations, with Neumann and tangential boundary conditions in [22]. As the fundamental solutions of this PDE has the same behavior at their singularity, we can use the same choices for G_1 and G_2. A slight modification of the choices in [22], which are altered so that some of the bounded terms vanish, is

$$\begin{aligned} G_1 &= -2G_{\nu\nu} + \left(\Delta - \lambda^2\right) G, \\ G_2 &= -2G_{\nu\nu\nu} + 3\left(\Delta - \lambda^2\right) G_\nu. \end{aligned}$$

We define

$$\begin{aligned} G_{11}(\mathbf{x}) &= \frac{\partial}{\partial \nu_{\mathbf{x}}} G_1, \quad G_{21}(\mathbf{x}) = \frac{\partial}{\partial \tau_{\mathbf{x}}} G_1, \\ G_{12}(\mathbf{x}) &= \frac{\partial}{\partial \nu_{\mathbf{x}}} G_2, \quad G_{22}(\mathbf{x}) = \frac{\partial}{\partial \tau_{\mathbf{x}}} G_2. \end{aligned}$$

Again, using results from [22], the resulting system of integral equations is

$$\begin{aligned} f_1(\mathbf{x}_0) &= \frac{1}{2}\sigma_1(\mathbf{x}_0) - \kappa(\mathbf{x}_0)\sigma_2(\mathbf{x}_0) \\ &\quad + \int_\Gamma G_{11}(\mathbf{y} - \mathbf{x}_0)\sigma_1(\mathbf{y}) ds_{\mathbf{y}} + \int_\Gamma G_{12}(\mathbf{y} - \mathbf{x}_0)\sigma_2(\mathbf{y}) ds_{\mathbf{y}}, \qquad (6.4a) \\ f_2(\mathbf{x}_0) &= \frac{1}{2}\frac{d}{ds}\sigma_2(\mathbf{x}_0) \\ &\quad + \int_\Gamma G_{21}(\mathbf{y} - \mathbf{x}_0)\sigma_1(\mathbf{y}) ds_{\mathbf{y}} + \int_\Gamma G_{22}(\mathbf{y} - \mathbf{x}_0)\sigma_2(\mathbf{y}) ds_{\mathbf{y}}, \qquad (6.4b) \end{aligned}$$

or in matrix form

$$\mathbf{f}(\mathbf{x}_0) = D[\sigma](\mathbf{x}_0) + \int_\Gamma A(\mathbf{y} - \mathbf{x}_0)\sigma(\mathbf{y}) ds_{\mathbf{y}},$$

where

$$\mathbf{f}(\mathbf{x}_0) = \begin{pmatrix} f_1(\mathbf{x}_0) \\ f_2(\mathbf{x}_0) \end{pmatrix}, \quad \sigma(\mathbf{x}_0) = \begin{pmatrix} \sigma_1(\mathbf{x}_0) \\ \sigma_2(\mathbf{x}_0) \end{pmatrix},$$

$$D = \begin{pmatrix} \frac{1}{2} & -\kappa \\ 0 & \frac{1}{2}\frac{d}{ds} \end{pmatrix},$$

$$A(\mathbf{y}-\mathbf{x}_0) = \begin{pmatrix} G_{11}(\mathbf{y}-\mathbf{x}_0) & G_{12}(\mathbf{y}-\mathbf{x}_0) \\ G_{21}(\mathbf{y}-\mathbf{x}_0) & G_{22}(\mathbf{y}-\mathbf{x}_0) \end{pmatrix}.$$

$\kappa(\mathbf{x}_0)$ is the curvature of Γ at $\mathbf{x}_0$ and d/ds is the arclength derivative.

This is not yet a Fredholm integral equation of the second kind. We need the matrix D to be constant. The problematic terms in D are the term involving the curvature and the term involving the arclength derivative. We eliminate them with a preconditioner outlined in [22]. We first construct an indefinite integral operator P satisfying

$$\frac{d}{ds}P(\sigma(\mathbf{x}_0)) = \sigma(\mathbf{x}_0)$$

for all σ. It is problem dependent, but is readily available. If $\mathbf{r}(\theta)$ with $\theta \in [0, 2\pi)$ is a parameterization of Γ, we choose

$$P[\sigma](\mathbf{x}) = \int_0^\theta \sigma(\mathbf{r}(\omega))|\mathbf{r}'(\omega)|d\omega,$$

where $\mathbf{x} = \mathbf{r}(\theta)$. Then

$$\begin{aligned} \frac{d}{ds}P[\sigma](\mathbf{x}) &= \frac{d}{ds}\int_0^\theta \sigma(\mathbf{r}(\omega))|\mathbf{r}'(\omega)|d\omega \\ &= \frac{1}{|\mathbf{r}'(\theta)|}\frac{d}{d\theta}\int_0^\theta \sigma(\mathbf{r}(\omega))|\mathbf{r}'(\omega)|d\omega \\ &= \frac{1}{|\mathbf{r}'(\theta)|}\sigma(\mathbf{r}(\theta))|\mathbf{r}'(\theta)| \\ &= \sigma(\mathbf{x}). \end{aligned}$$

So,

$$\frac{d}{ds}P[\sigma] = \sigma$$

as desired. We note that P can be calculated with spectral accuracy if we first compute the Fourier series of the integrand

$$\sigma(\mathbf{r}(\omega))|\mathbf{r}'(\omega)| = \sum_{n\in\mathbb{Z}} c_n e^{in\omega}.$$

Then,

$$P[\sigma](\mathbf{x}) = c_0\theta - \sum_{n\neq 0}\frac{c_n}{in} + \sum_{n\neq 0}\frac{c_n}{in}e^{in\theta},$$

which is the sum of a linear function in θ and a Fourier series.

We construct the preconditioner

$$E = \begin{pmatrix} 2I & 4\kappa P \\ 0 & 2P \end{pmatrix},$$

which satisfies $DE = I$. Then, a solution of (6.4) is $\sigma = E\zeta$ where ζ solves

$$(I + AE)\zeta = f. \tag{6.5}$$

Equation (6.5) has no derivatives or curvature in the jump terms. Thus, it is a Fredholm integral equation of the second kind. Moreover, the following asymptotic expansions hold [1]

$$\lim_{\substack{\mathbf{y}\to\mathbf{x}_0 \\ \mathbf{y}\in\Gamma}} G_{11}(\mathbf{y}-\mathbf{x}_0) = \frac{\kappa(\mathbf{x}_0)}{2\pi},$$

$$\lim_{\substack{\mathbf{y}\to\mathbf{x}_0 \\ \mathbf{y}\in\Gamma}} G_{21}(\mathbf{y}-\mathbf{x}_0) = 0,$$

$$\lim_{\substack{\mathbf{y}\to\mathbf{x}_0 \\ \mathbf{y}\in\Gamma}} G_{12}(\mathbf{y}-\mathbf{x}_0) = \frac{3}{32\pi}(-8\kappa(\mathbf{x}_0)^2 + 4\lambda^2\log(\lambda/2) - 3\lambda^2 + 4\lambda^2\gamma + 4\lambda^2\log|\mathbf{y}-\mathbf{x}_0|),$$

$$\lim_{\substack{\mathbf{y}\to\mathbf{x}_0 \\ \mathbf{y}\in\Gamma}} G_{22}(\mathbf{y}-\mathbf{x}_0) = 0.$$

Three of the four kernels are bounded and continuous which guarantees that the integral operators are compact. The integral operator with kernel G_{12} is also compact since the singularity is only logarithmic [5, 18]. The preconditioner E is also compact. Thus, the Fredholm Alternative can be applied to discuss the existence and uniqueness of solutions of (6.5).

We demonstrate this method with two numerical examples. Because of the nature of the singularities, the trapezoidal rule with N points is used for G_{11}, G_{21}, and G_{22}, while Alpert's quadrature rules are used for G_{12}. Since we are solving for two density functions, the total number of unknowns is $2N$.

In the first example, $\lambda = 2$ and Ω is the ellipse whose boundary is $\mathbf{r}(\theta) = (\cos(\theta), 2\sin(\theta))$. We use the normal and tangential derivatives of the exact solution $\psi^H(\mathbf{x}) = I_0(2|\mathbf{x}|)$. The errors, timings, and total number of GMRES steps are summarized in Table 6.1. We see third-order convergence which results from the modified Bessel functions in the kernels. Higher-order quadrature rules for all the kernels would improve the accuracy. We also see quadratic scaling in the timings to perform a single GMRES step. Using a FMM would

N	GMRES Iterations	Time per Iteration	Total Time	Error
64	11	4.18×10^{-2}	0.46	3.07×10^{-3}
128	10	1.69×10^{-1}	1.69	3.86×10^{-4}
256	11	5.83×10^{-1}	6.41	4.82×10^{-5}
512	13	1.93×10^{0}	25.15	6.03×10^{-6}
1024	13	8.34×10^{0}	108.45	7.54×10^{-7}

Table 6.1: The maximum error is computed at points that are well away from Γ. The number of points, N, is the total number of discretization points. Since we are solving for two density functions, the total number of unknowns is in fact $2N$. Timings are given in seconds.

reduce the required time to $\mathcal{O}(N)$ or $\mathcal{O}(N \log N)$. Finally, we see that the total number of GMRES steps does not grow with N.

In the second example, we take $\lambda = 1$ and let the geometry be a starfish shape. We take the boundary conditions

$$\frac{\partial \psi^H}{\partial \nu} = -1, \quad \frac{\partial \psi^H}{\partial \tau} = 0.$$

Contour and surface plots are illustrated in Figure 6.1

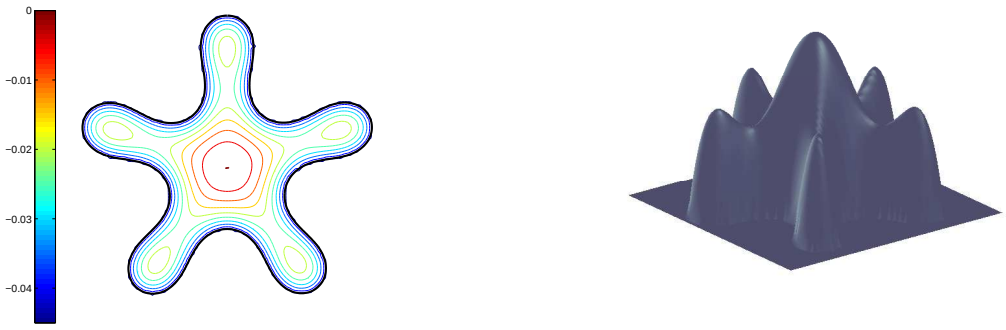

Figure 6.1: The domain Ω resembles a starfish. A total number of 2000 points is used to establish high-order accuracy near Γ. 36 GMRES iterations are required to achieve an accuracy of 10^{-10}.

6.1.2 Cahn-Hilliard

The Cahn-Hilliard equation is

$$\frac{\partial c}{\partial t} = D\Delta(c^3 - c - \gamma\Delta c), \tag{6.6}$$

where $\gamma > 0$ and $D > 0$. One possible temporal discretization of (6.6) is

$$\frac{c^{N+1} - c^N}{dt} = D\Delta(c^N)^3 - D\Delta c^N - D\gamma\Delta^2 c^{N+1}.$$

Rearranging,

$$(1 + dtD\gamma\Delta^2)c^{N+1} = c^N + dtD\Delta(c^N)^3 - dtD\Delta c^N.$$

This motivates developing integral equation methods for the operator $(1 + \alpha^2\Delta^2)$. There are also many other problems that involve the operator

$$\frac{\partial u}{\partial t} + \beta^2\Delta^2$$

in areas such as elasticity. Temporal discretizations of this PDE would again result in the operator $(1 + \alpha^2\Delta^2)$.

6.2 Conclusions

Integral equations offer an exciting alternative for solving PDEs arising in physics and engineering. By coupling them with fast algorithms, large-scale problems with complex geometries can be solved with high accuracy. In this thesis, we developed fast integral equation methods for the modified Helmholtz equation for the purpose of solving the forced heat equation. We based the approach on Rothe's method where first a temporal discretization is done, then the resulting sequence of elliptic boundary value problems are solved.

Chapter 2 discussed temporal discretizations of the nonlinear heat equation and developed potential theory for the resulting modified Helmholtz equation. The homogeneous modified Helmholtz equation was recast as a boundary integral equation and existence and uniqueness of the homogeneous PDE and the boundary integral equation were established. Chapter 3 developed numerical methods for the boundary integral equations from Chapter 2. The trapezoidal rule failed to achieve the desired spectral accuracy because of a loss of smoothness of the integral operators' kernels. Instead, we adopted high-order quadrature

rules designed for functions with logarithmic singularities. By coupling these quadrature rules with Fourier interpolation, high-order accuracy was achieved. A near-singular integration was applied to guarantee a uniform bound for the error of the solution of the PDE. These methods were applied to both interior and exterior, multiply-connected domains, with either Dirichlet or Neumann boundary conditions. In Chapter 4, a volume integral developed in [17] was coupled with methods from Chapter 3 to build a solver for the forced modified Helmholtz equation. This required extending the forcing function from the domain Ω to a box D containing Ω. Three options for constructing this extension were described and compared. It became apparent that a smooth, compactly supported extension is important. Numerical examples demonstrated the capabilities and limitations of the method. Chapter 5 developed a particle-based fast multipole method for solving the linear systems in Chapter 3. Timings and errors were demonstrated.

Future directions of this thesis include solving a larger variety of PDEs that can be interpreted as a forced heat equation. This includes reaction-diffusion, variational, and fluid dynamics problems. This requires a more careful implementation of near-singular integration and smoother extensions of arbitrary functions. Another future direction is the development of integral equation methods for PDEs whose order is greater than two. This includes the two-dimensional Navier-Stokes equations and the Cahn-Hilliard equation.

Bibliography

[1] M. Abramowitz and I. Stegun. *Handbook of Mathematical Functions with Formulas, Graphs and Mathematical Tables*. Dover, New York, 1964.

[2] B. K. Alpert. Hybrid Gauss-Trapezoidal Quadrature Rules. *SIAM Journal on Scientific Computing*, 20:1551–1584, 1999.

[3] S. Amini and A. Profit. Analysis of the truncation errors in the fast multipole method for scattering problems. *Journal of Computational and Applied Mathematics*, 115:23–33, 2000.

[4] U.M. Ascher, S.J. Ruuth, and B.T.R. Wetton. Implicit-explicit methods for time-dependent partial differential equations. *SIAM Journal on Numerical Analysis*, 32:797–823, 1995.

[5] K.E. Atkinson. *The Numerical Solution of Boundary Integral Equations*. Cambridge University Press, Cambridge, MA, 1997.

[6] J. Barnes and P. Hut. A hierarchical *0(NlogN)* force-calculation algorithm. *Nature Publishing Group*, 324:446–449, 1986.

[7] J.T. Beale and M.-C. Lai. A Method for Computing Nearly Singular Integrals. *SIAM Journal on Numerical Analysis*, 38(6):1902–1925, 2001.

[8] R. Beatson and L. Greengard. A short course on fast multipole methods. In *Wavelets, Multilevel Methods and Elliptic PDEs*, pages 1–37. Oxford University Press, 1997.

[9] G. Biros and S.K. Veerapaneni. The Chebyshev fast Gauss and nonuniform fast Fourier transforms and their application to the evaluation of distributed heat potentials. *Journal of Computational Physics*, 227:7768–7790, 2007.

[10] G. Biros, L. Ying, and D. Zorin. An Embedded Boundary Integral Solver for the Unsteady Incompressible Navier-Stokes Equations. *preprint*, 2002.

[11] G. Biros, L. Ying, and D. Zorin. An Embedded Boundary Integral Solver for the Stokes Equations. *Journal of Computational Physics*, 193:317–348, 2004.

[12] J. Carrier, L. Greengard, and V. Rokhlin. A Fast Adaptive Multipole Algorithm for Particle Simulations. *SIAM Journal on Scientific and Statistical Computing*, 9(4):669–686, 1988.

[13] R. Chapko. On the Combination of Rothe's Method and Boundary Integral Equations for the Nonstationary Stokes Equation. *Journal of Integral Equations and Applications*, 13(2):99–116, 2001.

[14] R. Chapko and R. Kress. Rothe's Method for the Heat Equation and Boundary Integral Equations. *Journal of Integral Equations and Applications*, 9:47–69, 1997.

[15] H. Cheng and L. Greengard. A Method of Images for the Evaluation of Electrostatic Fields in Systems of Closely Spaced Conducting Cylinders. *SIAM Journal on Applied Mathematics*, 58(1):122–141, 1998.

[16] H. Cheng, L. Greengard, and V. Rokhlin. A Fast Adaptive Multipole Algorithm in Three Dimensions. *Journal of Computational Physics*, 155:468–498, 1999.

[17] H. Cheng, J. Huang, and T.J. Leiterman. An adaptive fast solver for the modified Helmholtz equation in two dimensions. *Journal of Computational Physics*, 211:616–637, 2005.

[18] D. Colton. *Partial Differential Equations*. Random House, New York, NY, 1988.

[19] A. Dutt, L. Greengard, and V. Rokhlin. Spectral Deferred Correction Methods for Ordinary Differential Equations. *BIT Numerical Mathematics*, 40:241–266, 2000.

[20] F. Ethridge and L. Greengard. A New Fast-Multipole Accelerated Poisson Solver in Two Dimensions. *SIAM Journal on Scientific Computing*, 23:741–760, 2001.

[21] L. Evans. *Partial Differential Equations*. American Mathematical Society, Providence, Rhode Island, 1998.

[22] P. Farkas. *Mathematical Foundations for Fast Algorithms for the Biharmonic Equation*. PhD thesis, University of Chicago, 1989.

[23] B. Folland. *Introduction to Partial Differential Equations*. Princeton University Press, Princeton, New Jersey, 1995.

[24] A. Greenbaum, L. Greengard, and G.B. McFadden. Laplace's Equation and the Dirichlet-Neumann Map in Multiply Connected Domains. *Journal of Computational Physics*, 105:267–278, 1993.

[25] L. Greengard and J. Huang. A New Version of the Fast Multipole Method for Screened Coulomb Interactions in Three Dimensions. *Journal of Computational Physics*, 180:642–658, 2002.

[26] L. Greengard, M.C. Kropinski, and A. Mayo. Integral Equation Methods for Stokes Flow and Isotropic Elasticity in the Plane. *Journal of Computational Physics*, 125:403–414, 1996.

[27] L. Greengard and J.-Y. Lee. A Direct Adaptive Poisson Solver of Arbitrary Accuracy. *Journal of Computational Physics*, 125:415–424, 1995.

[28] L. Greengard and J.-R. Li. On the numerical solution of the heat equation I: Fast solvers in free space. *Journal of Computational Physics*, 226:1891–1901, 2007.

[29] L. Greengard and J.-R. Li. High order accurate methods for the evaluation of layer heat potentials. *SIAM Journal on Scientific Computing*, 31(5):3847–3860, 2009.

[30] L. Greengard and V. Rokhlin. A Fast Algorithm for Particle Simulations. *Journal of Computational Physics*, 73:325–348, 1987.

[31] L. Greengard and V. Rokhlin. A new version of the Fast Multipole Method for the Laplace equation in three dimensions. *Acta Numerica*, 6:229–269, 1997.

[32] J. Helsing and R. Ojala. On the evaluation of layer potentials close to their sources. *Journal of Computational Physics*, 227:2899–2921, 2008.

[33] J. Huang, J. Jia, and M. Minion. Accelerating the convergence of spectral deferred correction methods. *Journal of Computational Physics*, 214:633–656, 2006.

[34] J. Jia and J. Huang. Krylov deferred correction accelerated method of lines transpose for parabolic equations. *Journal of Computational Physics*, 227:1739–1753, 2008.

[35] O.D. Kellogg. *Foundations of Potential Theory.* Dover Publications, New York, 1953.

[36] M.C. Kropinski and B.D. Quaife. Fast integral equation methods for Rothe's method applied to the isotropic heat equation. *Computers and Mathematics with Applications*, preprint, 2010.

[37] M.C. Kropinski and B.D. Quaife. Fast integral equation methods for the modified Helmholtz equation. *Journal of Computational Physics*, 230:425–434, 2011.

[38] L. Greengard and M.C. Kropinski. An Integral Equation Approach to the Incompressible Navier-Stokes Equations in Two Dimensions. *SIAM Journal on Scientific Computing*, 20:318–336, 1998.

[39] J. Ma, V. Rokhlin, and S. Wandzura. Generalized Gaussian Quadrature Rules for Systems of Arbitrary Functions. *SIAM Journal on Numerical Analysis*, 33(3):971–996, 1996.

[40] P.G. Martinsson and V. Rokhlin. A fast direct solver for boundary integral equations in two dimensions. *Journal of Computational Physics*, 205:1–23, 2005.

[41] A. Mayo. The Fast Solution of Poisson's and the Biharmonic Equations on Irregular Regions. *SIAM Journal on Numerical Analysis*, 21(2):285–289, 1984.

[42] A. Mayo. Rapid, Fourth Order Accurate Solution of the Steady Navier-Stokes Equations on General Regions. *Dynamics of Continuous, Discrete and Impulsive Systems*, 12(1):59–72, 2005.

[43] A. Mayo and A. Greenbaum. Fourth order accurate evaluation of integrals in potential theory on exterior 3D regions. *Journal of Computational Physics*, 220:900–914, 2006.

[44] V. Rokhlin. Rapid Solution of Integral Equations of Scattering Theory in Two Dimensions. *Journal of Computational Physics*, 86:414–439, 1990.

[45] Y. Saad and M.H. Schultz. GMRES: A Generalized Minimal Residual Algorithm for Solving Nonsymmetric Linear Systems. *SIAM Journal on Scientific and Statistical Computing*, 7:856–869, 1986.

[46] L.N. Trefethen. *Spectral Methods in MatLab*. Society for Industrial and Applied Mathematics, Philadelphia, PA, USA, 2000.

[47] S.K. Veeranpaneni and G. Biros. A High-Order Solver for the Heat Equation in 1D domains with Moving Boundaries. *SIAM Journal on Scientific Computing*, 29, 2006.

[48] G.N. Watson. *A Treatise on the Theory of Bessel Functions*. Cambridge University Press, Cambridge, second edition, 1944.

[49] L. Ying, G. Biros, and D. Zorin. A kernel-independent adaptive fast multipole algorithm in two and three dimensions. *Journal of Computational Physics*, 194:591–626, 2004.

[50] L. Ying, G. Biros, and D. Zorin. A High-order 3D Boundary Integral Equation Solver for Elliptic PDEs in Smooth Domains. *Journal of Computational Physics*, 219:247–275, 2006.